2018-05-10

Brittleness and Fracability Evaluation of Unconventional Reservoirs

Hu, Yuan

UNIVERSITY OF CALGARY

Brittleness and Fracability Evaluation of Unconventional Reservoirs

by

Yuan Hu

A THESIS

SUBMITTED TO THE FACULTY OF GRADUATE STUDIES

IN PARTIAL FULFILMENT OF THE REQUIREMENTS FOR THE

DEGREE OF DOCTOR OF PHILOSOPHY

GRADUATE PROGRAM IN CHEMICAL AND PETROLEUM ENGINEERING

CALGARY, ALBERTA

MAY, 2018

Abstract

Brittleness and fracability evaluation plays an important role in recovery of unconventional oil and gas; it directly influences the effect of hydraulic fracturing. The definition of brittleness is controversial and the existing analytical/semi-analytical models have no unified theory to support them. Brittleness and fracability evaluation is currently unreliable. Unconventional reservoirs have different confining pressure, pore pressure and temperature. Models that do not consider these influences lack accuracy in the brittleness index (BI) calculation, resulting in failure during hydraulic fracturing.

This research is focused on establishing new methods for brittleness and fracability evaluation. First, analytical/semi-analytical models are proposed considering the influence of confining pressure, pore pressure and temperature, respectively. The influence of calcite on rock mechanics parameters and brittleness is compared to quartz and clay. The weight of each parameter in models based on elastic modulus and mineralogy is analyzed. Finally, a numerical method to evaluate rock brittleness in terms of energy is developed. This novel method is applied to evaluate rock brittleness and fracability in more complicated conditions by considering hydro-mechanical (HM) interaction.

By defining brittleness in terms of energy, rock brittleness from different sources can be compared. The influence factors ignored by other models of brittleness evaluation: pressure, temperature and rock texture can be addressed at the same time. By combining the analytical method and the numerical method for brittleness and fracability the resulting evaluations are more applicable because they reflect a more realistic unconventional oil and gas reservoirs environment.

Keywords: brittleness, fracability, unconventional reservoirs, energy

Acknowledgements

I would like to take this opportunity to give my greatest gratitude to my supervisor, Dr. Zhangxing (John) Chen, for his selfless support during my doctoral study at the University of Calgary. The plentiful resources, opportunities and trust he gave to me are deeply appreciated. I am also grateful to my supervisory committee members Dr. Haiping Huang, Dr. Hossein Hejazi, Dr. Xin Wang and Dr. Alireza Nouri for their time and efforts.

Special thanks go to Dr. Keliu Wu for enlightening me with the research and Jamie Mclnnis and Wei Liu for reviewing the thesis. My gratitude also goes to my colleagues in the Reservoir Simulation Group and my friends who supported me in my research, sparking incentives to strive towards my goal.

Last but not the least, I would like to thank my family for their unconditional support and love throughout my life.

Table of Contents

List of Tables

List of Figures and Illustrations

List of Symbols, Abbreviations and Nomenclature

Symbol	Definition
a_I	Nodal enriched degree of freedom vector
b_I^{α}	Nodal enriched degree of freedom vector
BI_R	Brittleness index calculated by Rickman's equation
BI_{new}	Brittleness index calculated by new equations
BI_Q	Brittleness index calculated by mineralogical method
DT	Interval transit time, *us/ft*
E	Young's modulus, GPa
E_T	Young's modulus at temperature T, GPa
E_0	Young's modulus at room temperature, GPa
E_i	the elastic modulus after unloading in direction I, GPa
$\dot{E}_W$	the rate of work done to the body by external forces
$\dot{E}_{QB}$	the rate of energy dissipated by the damping effect of solid medium infinite elements
$\dot{E}_F$	the rate of energy dissipated by contact friction forces between the contact surfaces
E_D	the damage energy, J
E_I	the internal energy, J
E_S	the applied elastic strain energy, J
E_P	the energy dissipated by plasticity, J
E_C	the energy dissipated by time-dependent deformation (creep, swelling, and viscoelasticity), J

E_W	work done by the externally applied loads, J
E_{HF}	external heat energy through external fluxes, J
E_{IE}	internal energy, J
E_{KE}	kinetic energy, J
E_{FD}	frictional energy dissipated, J
E_V	viscous energy dissipated, J
E_{IHE}	internal heat energy, J
E_E	recoverable elastic strain energy, J
E_P	energy dissipated through inelastic processes such as plasticity, J
E_{CD}	energy dissipated through viscoelasticity or creep, J
E_A	artificial strain energy, J
E_{DMD}	energy dissipated through damage, J
E_{DC}	energy dissipated through distortion control, J
E_{FC}	fluid cavity energy, J
e_s	internal energy per unit of mass of solid
e_i	internal energy per unit of mass of liquid
f	the body force vector
f'	empirical factor
F_a	asymptotic crack-tip functions
G	shear modulus, psi
$H(x)$	jump function
H	the height of the sample

K_g	bulk modulus, psi
K_C	critical stress intensity factor, MPa·m$^{0.5}$
K_{IC}	mode I fracture toughness, MPa·m$^{0.5}$
K_{IC}^0	mode I fracture toughness of rocks when Pc=0, MPa·m$^{0.5}$
I_m^h	average coefficient of heat conduction
I_l^h	coefficient of heat conduction of liquid
M	axial modulus, psi
N	the equivalent number of rock fragments
$N_I(x)$	shape function
N	the normal direction vector on boundary S
P_c	confining pressure, MPa
P_g	total pressure of gas
P_p	pore pressure, psi
q_{rl}	density vector of liquid
R	the radius of the sample
r	the equivalent radius of the rock fragments
r_{ef}	energy efficiency in fracturing
S	total vertical stress, psi
S_l	liquid saturation
T	temperature, °F
t	time, s
t_v	the surface traction vector
U	the internal energy per unit mass, J/kg

U^d	the dissipation energy, J
U_i	the input energy in direction I, J
U_i^d	the dissipation energy in direction I, J
U_i^e	the releasable strain energy in direction I, J
u	displacement vector
u_I	nodal displacement vectors
V_0	the molar volume
V_{cl}	clay content, %
V_p	P-wave velocity, km/s
V_s	S-wave velocity, km/s
v	the velocity field vector
v	Poisson's ratio, %
ε_p	peak strain, %
ε_r	residual strain, %
ε_v	volumetric strain of solid
$\dot{\varepsilon}$	strain rate tensor
σ_c	compressive strength, MPa
σ^c	the stress derived from the user-specified constitutive equation, MPa
σ^{el}	the elastic stress, MPa
σ_v	the viscous stress, MPa
σ_t	tensile strength, MPa
σ'	effective pressure, MPa

σ_g	effective stress acting on individual grains, MPa
σ	macroscopic stress tensor
β_{lpo}	is constant, subscript o means reference state
β_{Tg}	thermal expansion coefficient of solid phase
β_g	grain compressibility, 1/psi
β_f	fluid compressibility, 1/psi
φ	porosity
α_g	grain cubic thermal expansivity, 1/°F
α_f	fluid cubic thermal expansivity, 1/°F
γ	surface free energy
ρ	the current mass density, g/cm^3
ρ_s	solid density, kg/m^3
ρ_l	liquid density, kg/m^3
ρ_l^w	bulk density of liquid phase
ρ_s	mass density of solid phase
ALLDMD	damage dissipation energy for whole model
ALLIE	internal energy for whole model
ALLPE	plastic dissipation energy for whole model
ALLSE	strain energy for whole model
BI	brittleness indice
Cal	calcite content, %
Dol	dolomite content, %
ETOTAL	total energy for whole model

FE	finite element
FEM	finite element method
MAXPS	maximum principal stress
MAXPSC	maximum principal strain criterion
MAXSERC	maximum strain energy release rate criterion
MSSC	maximum shear stress criterion
Qtz	quartz content, %
SEM	scanning electron microscope
SPH	smoothed particle hydrodynamics
SPSS	Statistic Package for Social Science
TOC	total organic carbon
XFEM	extended finite element method
2D	two dimensional
3D	three dimensional

1. Introduction

1.1 Research Background

In the development of unconventional oil and gas reservoirs, hydraulic fracturing is one of the keys for their successful exploitation (Vermylen, 2011; Wu, 2015). It is a well stimulation technique in which the reservoirs are fractured by high pressure fluid. The process of hydraulic fracturing involves the injection of high-pressure fracturing fluid through a wellbore into the reservoirs so as to create fractures. The oil, natural gas and/or water inside the reservoirs could then flow out through those fractures (Gandossi, 2015). The ability to effectively fracture organic-rich reservoirs like shale gas and tight oil reservoirs by fluid injection is really important to production. Therefore, it is crucial to establish an effective way to evaluate the ability of unconventional reservoirs to create fractures.

The term brittleness is widely used in shale and tight reservoirs to evaluate the potential effectiveness of hydraulic fracture initiation and propagation (Wang, 2009). A material is brittle if it breaks without plastic deformation under the stress. Brittleness index has been used to describe the ability of material brittleness. It is a parameter influenced by many factors, including rock mineralogy, rock mechanics characteristics, in-situ stress and pressure.

1.2 Literature Review

There are a variety of brittleness descriptions and characterizations, making the definition of brittleness ambiguous and inconsistent (Tarasov, 2013; Jin, 2015).

Honda and Sanada (1956) first proposed a brittleness model based on hardness and bulk modulus. Hucka and Das (1974) summarized a number of characteristics of brittle rocks (Table

1.1): fracture failure, a higher angle of internal friction, and a higher ratio of compressive to tensile strength. These characteristics are thought to represent general behaviours of brittle rocks.

Table 1.1 Brittleness Indices in the literature

	Brittleness Indices	Reference
$BI_1 = \frac{(H_m - H)}{K}$	H: macro-hardness H_m: micro-hardness K: bulk modulus	Honda and Sanada (1956)
$BI_2 = \frac{\tau_{max} - \tau_{res}}{\tau_{max}}$	τ_{max}: peak strength τ_{res}: residual strength	Bishop (1967)
$BI_3 = \frac{\varepsilon_{el}}{\varepsilon_{tot}}$	ε_{el}: elastic strain	Hucka and Das (1974)
$BI_4 = \frac{W_{el}}{W_{tot}}$	W_{el}: elastic energy W_{tot}: total energy	Hucka and Das (1974)
$BI_5 = \sin\varphi$	φ: friction angle	Hucka and Das (1974)
$BI_6 = \frac{C_0 - T_0}{C_0 + T_0}$	C_0: compressive strength T_0: tensile strength	Hucka and Das (1974)
$BI_7 = \frac{H}{K_{IC}}$	H : hardness K_{IC} : fracture toughness	Lawn and Marshall (1979)
$BI_8 = \varepsilon_{ux} \times 100\%$	E_{ux}: unrecoverable axial strain	Andreev (1995)
$BI_9 = \frac{c}{d}$	c: crack length d: indent size for Vickers indents at a specified load; empirically related to H/K_{IC}	Sehgal et al. (1995)
$BI_{10} = \frac{H \cdot E}{K_{IC}^2}$	H: hardness E: Young's modulus K_{IC} : fracture toughness	Quinn and Quinn (1997)
$BI_{11} = (\frac{\sigma_{v,max}}{\sigma_v})^b$	$\sigma_{v,max}$: max previous experienced effective vertical stress σ_v: current effective vertical stress b: empirical value	Ingram and Urai (1999)
$BI_{12} = \left\lvert \frac{\varepsilon_f^p - \varepsilon_c^p}{\varepsilon_c^p} \right\rvert$	ε_f^p: plastic strain at failure ε_f^p: specific strain beyond failure	Hajiabdolmajid and Kaiser (2003)
$BI_{13} = \frac{\sigma_c \sigma_t}{2}$	σ_c: compressive strength σ_t : tensile strength	Altindag (2003)
$BI_{14} = \frac{P_{inc}}{P_{dec}}$	P_{inc} : average increment P_{dec} : decrement of forces	Copur et al. (2003)
$BI_{15} = \frac{W_{qtz}}{Wtot}$	W_{qtz}: quartz weight W_{tot}: total mineral weight	Jarvie et al. (2007)
$BI_{16} = \frac{1}{2}(\frac{E_{max} - E}{E_{max} - E_{min}} + \frac{v_{max} - v}{v_{max} - v_{min}})$	E: Young's modulus v : Poisson's ratio	Modified from Rickman et al. (2008)
$BI_{17} = \frac{F_{max}}{P}$	F_{max}: the maximum applied force on the Specimen P: the corresponding penetration	Yagiz (2009)
$BI_{18} = \frac{W_{qtz} + W_{dol}}{Wtot}$	W_{qtz}: quartz weight W_{dol}: dolomite weight W_{tot}: total mineral weight	Wang and Gale (2009)

The models from Bishop (1967), Andreev (1995) and Hajiabdolmajid and Kaiser (2003) are based on stress/strain test. The models of Sehgal (1995), Copur(2003) and Yagiz (2009) are based on indentation test. Altindag's model (2003) refers to compressive and tensile strength, which can be obtained from uniaxial compressive strength and Brazilian tests. The models from Quinn (1997) and Lawn and Marshall (1979) use hardness and fracture toughness as the main parameters. Rickman's model (2008) is related to Young's modulus and Poisson's ratio. The models proposed by Jarvie (2007) and Wang and Gale (2009) are based on mineral component.

Most of the existing models rely on rock mechanics tests. The last three models (BI_{16} – BI_{18}), which can be obtained from well loggings or related tests, are more practical than the others. Table 1.1 combines the existing brittleness indices mentioned above. The numerous proposed brittleness indices (BI) reflect the diversity of definitions and descriptions (Table 1.1). They share limitations that will be considered in this thesis.

1.3 Statement of Limitations

Currently, brittleness evaluation models are based on semi-analytic or empirical equations. Most of the existing models ignore the effect of confining pressure, pore pressure and temperature. Shale and tight reservoirs underground are usually full of water, oil or gas with different confining pressure, temperature and pore pressure (Figure 1.1). These factors can promote or prevent reservoir failure.

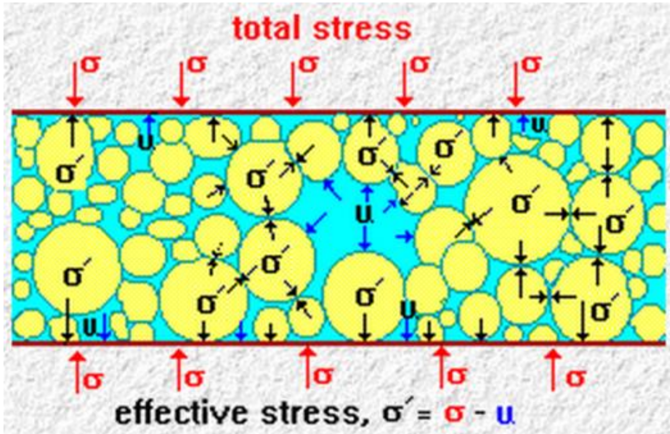

Figure 1.1 Reservoirs underground with confining pressure and pore pressure

Figures 1.2 a and b are rock samples with equal elastic modulus or equal peak and residual strength levels. The differences of brittleness may be influenced by pressure and temperature. Temperature changes rock texture and influences rock brittleness through pore pressure. Abnormal pore pressure may be formed by high overburden pressure and high temperature because shale and tight reservoirs have very low permeability. Models that do not consider the influence of these factors are inaccurate in their BI calculation and the result is the failure of hydraulic fracturing. Some research has been conducted to analyze a relationship between brittleness and confining pressure (Hucka, 1974; Jarvie, 2007; Rickman, 2008; Holt, 2011). They provided a relationship in charts without further explanation. They did not explore how to include the influence of confining pressure in brittleness evaluation. Some of them simply concluded that BI increases with confining pressure because Young's modulus increases with confining pressure. Therefore, research that explores the evaluation of brittleness and considers pressure, temperature and pore fluid is needed.

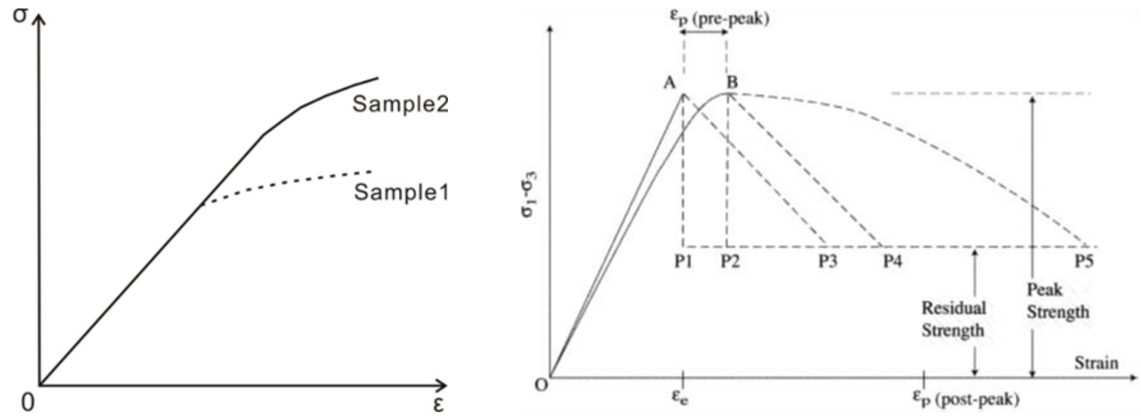

a.Two samples with equal elastic modulus   b.Two samples with equal peak and residual strength

Figure 1.2 Schematic representations of various stress–strain curves (Ingram, 1999)

Another limitation of the current models is the lack of consideration given to the weight of each parameter and the use of an ambiguous definition of brittle minerals. The petroleum industry commonly uses models of brittleness evaluation that are based on elastic modulus (elastic modulus models) or mineralogy (mineralogical models) because they are easily obtained from well logs (Jarvie, 2007; Rickman, 2008). The weights of Young's modulus and Poisson's ratio in BI prediction are undefined (Eq.1-1). Poisson's ratio does not play the same role as Young's modulus in an elastic modulus model. Rocks with more quartz tend to be more brittle than rocks with more feldspar. Similarly, quartz, dolomite, calcite and clay are different minerals with different properties of hardness, density and molecular structure. They do not play the same role in brittleness evaluation. When treated equally in the brittleness evaluation, the BI calculated is inaccurate.

$$BI_R = \frac{1}{2}\left(\frac{E_{MAX} - E}{E_{MAX} - E_{MIN}} + \frac{v_{MAX} - v}{v_{MAX} - v_{MIN}}\right) \tag{1-1}$$

$$BI_J = \frac{W_{qz}}{W_{tot}} \tag{1-2}$$

$$BI_W = \frac{W_{qz} + W_{dol}}{W_{tot}} \tag{1-3}$$

Calculating BI by considering quartz (or dolomite) as the only brittle mineral when using the mineralogical method lacks the necessary precision (Jarvie, 2007; Wang, 2009). Quartz is not the only brittle mineral in shale. Feldspar, dolomite and calcite may also be considered brittle minerals. The controversy is whether all these minerals should be considered as brittle minerals in BI prediction. Some previous studies compared the effect of calcite content to Young's modulus and Poisson's ratio. These studies found that an increase in calcite content increases Poisson's ratio but decreases Young's modulus (Diao, 2013; Yang, 2014). They concluded that calcite should not be considered a brittle mineral in BI prediction. Most shale gas reservoirs found in early exploration are siliceous and quartz is the primary brittle mineral in those reservoirs. It plays an important role in determining BI. It is reasonable to calculate BI by using Eq. 1-2. However, the development of unconventional oil and gas shale reservoirs like Eagle Ford are rich in carbonate minerals including calcite and dolomite. If the carbonate minerals are ignored in these reservoirs, the value of BI will be greatly underestimated. Wang et al. (2009) suggested to add dolomite as a brittle mineral in BI calculation (Eq. 1-3). But their model was still insufficient because they did not consider the weights of quartz and dolomite or calcite. Questions like whether carbonate minerals should be considered as a brittle mineral and how to obtain the weights of each brittle mineral and rock mechanics parameter in BI prediction are imperative to establish BI predictions that are more accurate.

Besides, the application of semi-analytic/empirical models in brittleness evaluation is limited. Semi-analytic/empirical models can be proposed that consider the influence of confining pressure, pore pressure or temperature, respectively, in this research. However, those factors (confining pressure, pore pressure and temperature) cannot be considered at the same time. Fracability, as a parameter to evaluate the ability of reservoirs to create fracture networks (Wang, 2015), cannot be described by the existing semi-analytic/empirical models. In other words, the existing semi-analytic/empirical models cannot reflect the degree of rock fragmentation. Also, empirical coefficients change in different areas, which makes the empirical models inaccurate.

A new method that considers interactions among factors of confining pressure, pore pressure, temperature, fluid and fracability is needed if brittleness and fracability evaluation is to be reliable.

1.4 Research Objectives

The purpose of this research is to establish effective and accurate methods in brittleness and fracability evaluation of unconventional reservoirs. The specific objectives are as follows:

1. Propose new analytic/semi-analytic models that consider the influence of confining pressure, pore pressure and temperature that have been ignored in the existing models.
2. Modify the existing models from Rickman and Jarve by considering weight of each factor. The definition of brittle minerals will also be involved.
3. Look for a new method from an experimental viewpoint to quantificationally describe rock/reservoir brittleness and fracability.
4. Look for a numerical method based on energy analysis so as to quantificationally describe rock/reservoir brittleness and fracability.

1.5 Structure of the Thesis

This thesis contains eight chapters.

Chapter 1 presents the background, literature review and the motivation of this research. It also describes the research problems and objectives.

Chapter 2 summarizes the methodologies used in this research. The detail of each method is also explained in each chapter below.

Chapters 3 and 4 analyze the influence of confining pressure, pore pressure and temperature. Analytic/semi-analytic models that consider the influence of confining pressure, pore pressure and temperature are proposed respectively in the end of each chapter.

Chapter 5 analyzes the influence of calcite and dolomite on rock brittleness and the weight of each parameter in the models based on elastic modulus and minerals. New models of BI are proposed to characterize the weight of each parameter in the end of the chapter.

Chapter 6 focuses on the energy analysis of rock failure based on axial compression tests. A new method of brittleness and fracability evaluation based on cyclic loading-unloading tests is proposed for brittle rocks.

Chapter 7 focuses on the energy analysis of rock failure and hydrofracture on numerical methods. A new method of brittleness and fracability evaluation based on finite element method (FEM) is proposed. This numerical method is applied to more complicated conditions by considering the influence of confining pressure and pore fluid in coupled hydro-mechanical (HM) models.

Chapter 8 summarizes the conclusions and future work of this research.

2. Methodologies

Based on the limitations described above, this thesis is focused on establishing new approaches to brittleness and fracability evaluation.

Analytic/semi-analytic models that consider the influence of confining pressure, pore pressure and temperature are proposed. Effective stress is introduced to provide the relationship among confining pressure, pore pressure and fracture toughness. Confining pressure and pore pressure are introduced into the new models by replacing fracture toughness. Data from experiments and oil fields is used to validate the models. Temperature influence on brittleness evaluation of unconventional reservoirs is analyzed based on rock texture and pore pressure. According to the analysis of uniaxial compression tests, scanning electron microscope (SEM) and X-ray diffraction, mechanical properties, texture and crack characteristics of rocks are obtained. Stress-strain curves of shale and sandstone samples at temperatures from 25℃ to 800℃ are used to analyze the temperature dependency of the elastic modulus, peak stress and strain.

Next, the influence of calcite on rock mechanics parameters and BI is analyzed and compared to quartz and clay. The weight of each parameter in the models is based on elastic modulus and mineralogy. Based on the least squares method, optimal values of weight coefficients are obtained by iteration.

A novel numerical method is developed that evaluates rock brittleness in terms of energy so as to consider the influence of confining pressure, pore pressure and temperature at the same time. This new method is used to evaluate rock brittleness in more complicated conditions by considering hydro-mechanical (HM) and thermo-hydro-mechanical (THM) interactions. Finite element (FE) modelling is introduced in this research to generate realistic simulations that consider the influence of plastic deformation and damage dissipation energy on brittleness and fracability evaluation. Data from cyclic loading-unloading and compression rock mechanics tests is used to refine and calibrate the models. An extended finite element method is used in crack growth for realistic failure predictions. The models are compared with the analytical models described above to validate the influence of confining pressure, pore pressure, temperature and rock texture on brittleness evaluation. By defining brittleness in terms of energy, rock brittleness from different areas can be compared. The influence factors ignored by other models of brittleness evaluation (confining pressure, pore pressure, temperature and rock texture) are addressed at the same time. Details of those methods are found at the end of each chapter.

3. Brittleness Evaluation: Confining Pressure and Pore Pressure

This chapter is focused on the first limitation effect of confining pressure and pore pressure on brittleness evaluation. The outcome is to establish new analytic/semi-analytic models based on previous research. The existing problems that need to be fixed and the details of the methods used to establish models are explored. Then, new models are established based on experimental data derived from these new methods. Case analysis and validation are completed using experimental data and oilfield production data. Part of this research has been published in SPE Asia Pacific Unconventional Resources Conference 2015 with me as the first author.

3.1 Existing Problems and Methodology

3.1.1 Existing Problems

Based on previous research, the relationships between pressure and rock mechanics parameters (including Young's modulus and Poisson's ratio) are described using data from different regions (Appendix A).

3.1.1.1 Compressive strength vs confining pressure

Data of Haynesville shale and Longmaxi shale (data1, Appendix A) shows that compressive strength increases with confining pressure (Figures 3.1 and 3.2). At low confining pressure, compressive strength increases rapidly with an increase in confining pressure. When confining pressure is high (more than 60MPa), the increase in compressive strength is slow.

3.1.1.2 Compressive strength vs Young's modulus

Figure 3.3 shows that compressive strength and Young's modulus satisfy a linear relationship. The correlation coefficient is > 0.87. Compressive strength is roughly derived from Young's modulus. The data from Sichuan Basin (data 2, Appendix A,) indicates that this relationship is not affected by the mineral composition (Table 3.1).

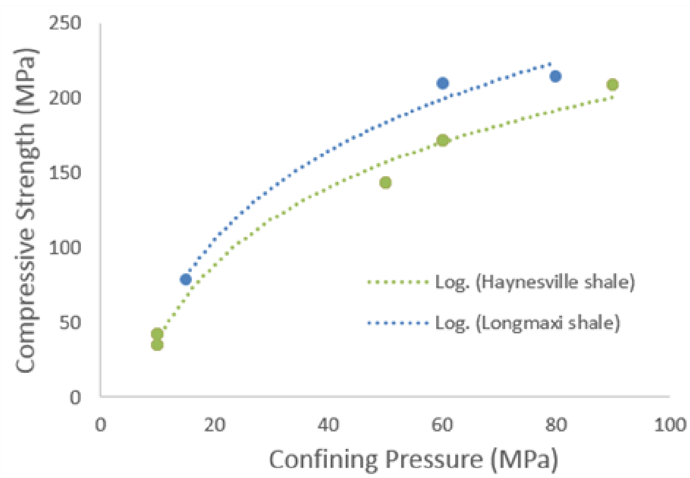

Figure 3.1 Compressive strength versus confining pressure

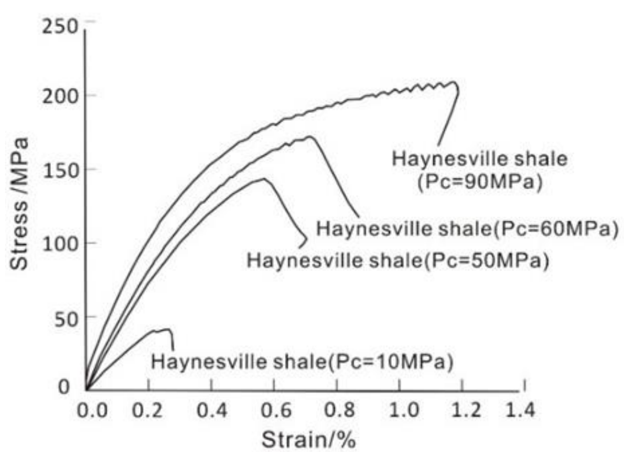

Figure 3.2 Influence of confining pressure on shale strength (Li, 2012)

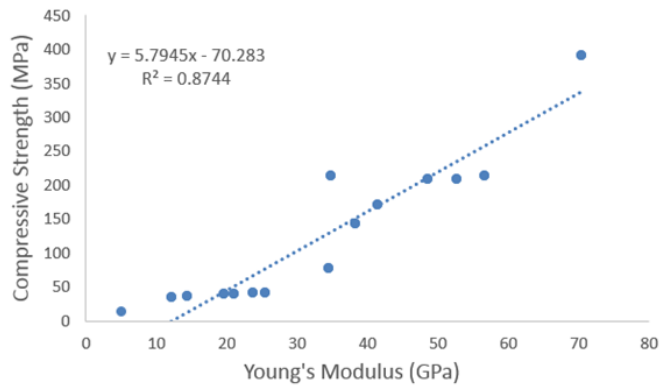

Figure 3.3 Compressive strength versus Young's modulus (Hu, 2015)

Table 3.1. Test and calculation result of data 1

Brittle Mineral (%)	Clay (%)	Confining Pressure (MPa)	Compressive Strength (MPa)	Tensile Strength (MPa)	Young's Modulus (GPa)	K_{IC_3-23} ($MPa{\cdot}m^{1/2}$)	K_{IC_3-24} ($MPa{\cdot}m^{1/2}$)	K_{IC_3-25} ($MPa{\cdot}m^{1/2}$)	BI_J	BI_R	BI_{3-23}	BI_{3-24}	BI_{3-25}
78.2	16.17	15	261.77	6.14	31.6	1.3444	1.0090	1.2338	0.782	0.789	0.868	0.898	0.890
78.2	16.17	30	337.87	6.14	31.5	1.9894	1.3710	1.7866	0.782	0.791	0.546	0.592	0.532
62.6	35.35	15	105.95	2.04	6.6	1.0116	0.9948	1.2079	0.626	0.403	0.459	0.336	0.334
62.6	35.35	30	140.71	2.04	7.5	1.6566	1.3567	1.7608	0.626	0.409	0.284	0.181	0.150
50.55	43.41	15	109.535	4.50	21.8	1.2813	0.9888	1.1976	0.506	0.517	0.558	0.512	0.512
50.55	43.41	30	160.815	4.50	23.8	1.9263	1.3507	1.7505	0.506	0.572	0.376	0.363	0.321
52.75	39.86	15	81.73	4.29	4.9	1.2720	0.9876	1.1970	0.528	0.286	0.252	0.164	0.162
52.75	39.86	30	160.215	4.29	12.5	1.9170	1.3495	1.7499	0.528	0.385	0.212	0.157	0.127
37.1	42.8	15	76.86	3.07	12.78	1.2478	0.9893	1.1971	0.371	0.422	0.223	0.368	0.368
36.8	46.9	30	162.33	4.70	16.73	1.8657	1.3511	1.7498	0.368	0.456	0.110	0.235	0.201

3.1.1.3 Young's modulus vs confining pressure

Data of Haynesville shale and Longmaxi shale indicates Young's modulus increases with an increase in confining pressure (Figures 3.4 and 3.5). Figure 3.2 provides the same result; the slope of the elastic portion increases with an increase in confining pressure. Young's modulus compressive strength and confining pressure increase with each other. Young's modulus is influenced by the load capacity of the rock. An increase in confining pressure improves the load capacity of the rock and its resistance to deformation and failure, increasing Young's modulus. Figure 3.4 shows that Young's modulus and confining pressure satisfies a linear relationship instead of nonlinear relationship. This may be because of data deficient.

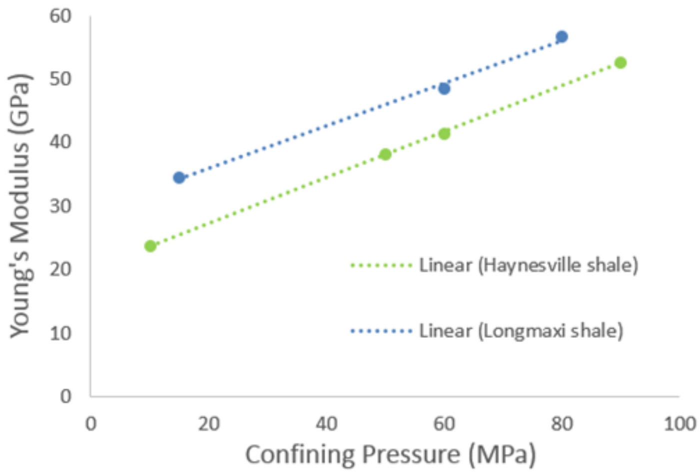

Figure 3.4 Young's modulus versus confining pressure (Hu, 2015)

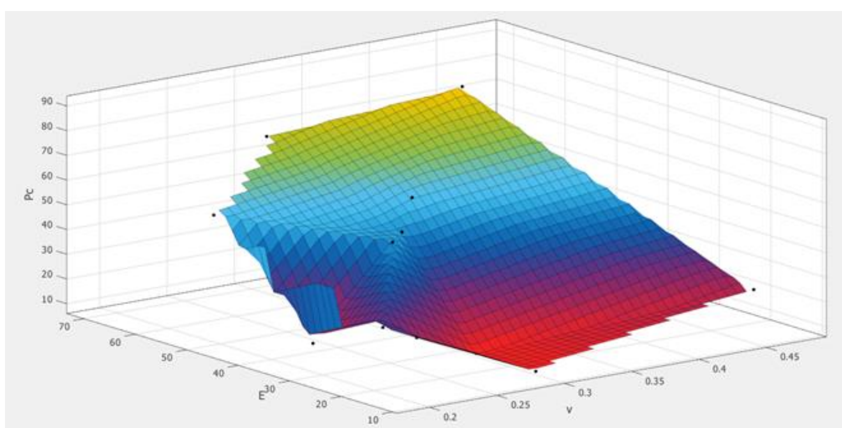

Figure 3.5 Confining pressure versus Young's modulus and Poisson's ratio from data

3.1.1.4 Poisson's ratio vs confining pressure

The Poisson ratio increases a small amount with confining pressure, but it is not obvious, especially for Longmaxi shale samples (Figure 3.6). Figure 3.5 from Appendix A data 1 also shows no obvious relationship between these two.

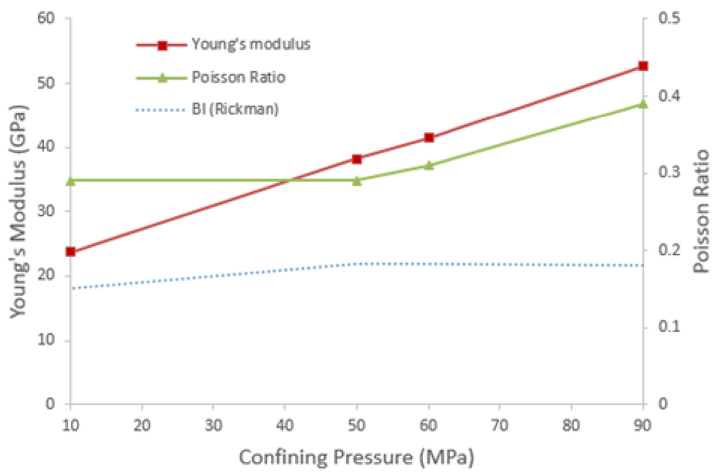

a. Haynesville shale samples

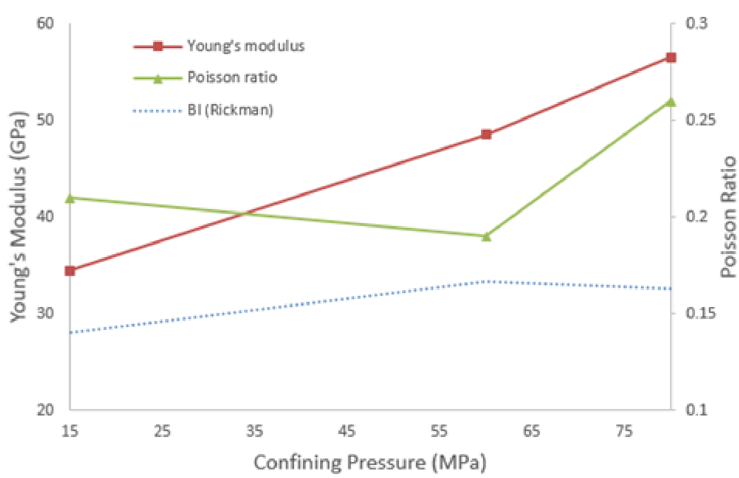

b. Longmaxi shale samples

Figure 3.6 Mechanical parameters at different confining pressure (Hu, 2015)

3.1.1.5 Number of microcracks vs confining pressure

Tests from Li et al. (2012) found that the microcrack number of samples decreases with an increase in confining pressure (Li, 2012). There are three different failure modes for shale samples at different confining pressures (Figure 3.7): splitting failure mode (E9, E10, E11, H4, H5, H6, and L15), splitting-shear failure mode (L14) and shear failure mode (B12, E8). The splitting failure mode is the main failure mode for shale samples at low confining pressure. The shear failure mode dominates at high pressure. A probable cause is that the confining pressure restrains the longitudinal spread of a crack.

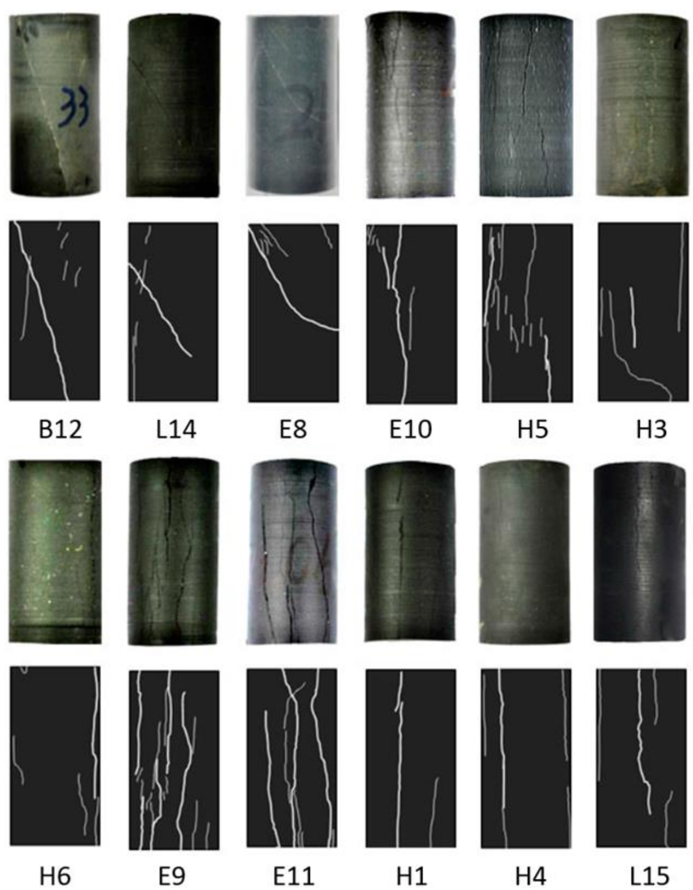

Figure 3.7 Typical failure modes of shale specimens under different pressure constraints (Pc) (Li, 2012)

3.1.1.6 Stress and strain vs pore pressure

The stress-strain curves in Figure 3.8 reflect an influence of pore pressure on ultimate strength and the shapes of the curves. This is related to the deformation mechanisms involved (Handin, 1963). It seems that the ultimate strength, yield strength and ductility tend to decrease as λ increases from 0 to 0.5 (Figure 3.9) (Rutter, 1972). λ signifies the ratio of pore-water pressure to total confining pressure.

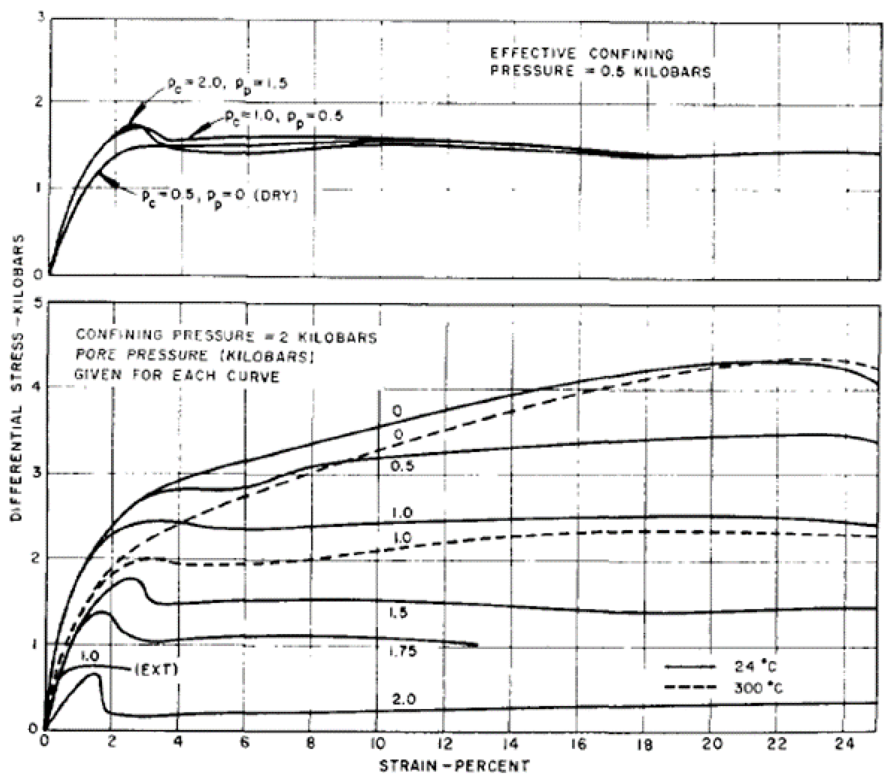

Figure 3.8 Stress-strain curves for Berea sandstone at different pore pressures (kilobars). *Below: all at 2 kilobars confining pressure and 24°C or 300°C; all in compression except curve marked Ext (for extension). Above: at confining pressures (Pc) of 0.5, 1, and 2 kilobars at 24°C; at pore pressures (Pp) of 0, 0.5, and 1.5 kilobars; all at same effective pressure of 0.5 kilobar. (Handin, 1963).*

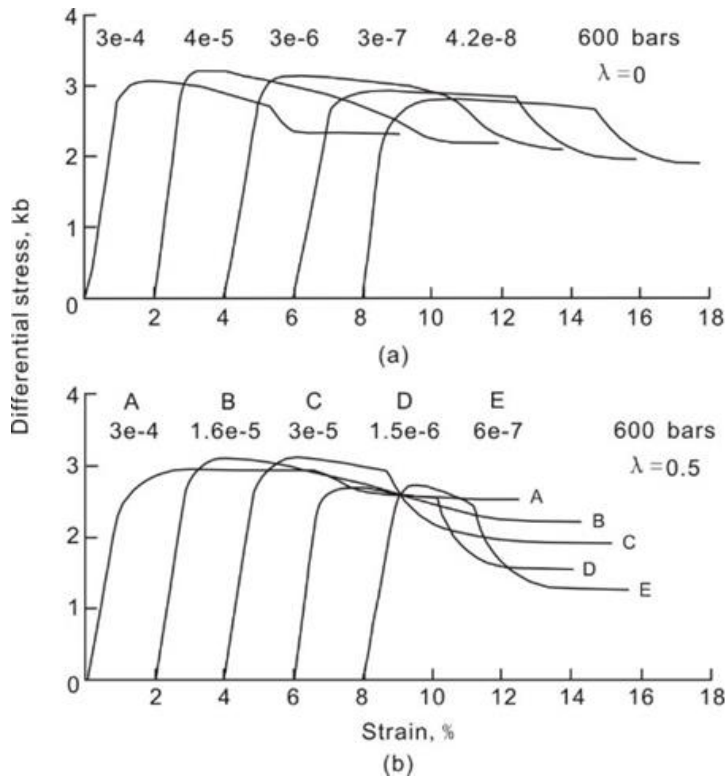

Figure 3.9 Axial stress vs strain curves for wet Solenhofen limestone deformed at 20°C

(a) 300 bars confining pressure, λ = 0, (b) 600 bars confining pressure, λ = 0 Strain rates (sec-1) are indicated with each curve (Rutter, 1972).

Young's modulus increases with an increase in confining pressure and there is no evidence of a relationship between Poisson's ratio and confining pressure. Using the model proposed by Rickman (2008), BI increases with confining pressure (Tables 3.1 and 3.2). Figure 3.6 indicates a change in mechanical parameters at different confining pressures. A blue dash line represents the trend of BI calculated from Rickman's equation (B_S). With an increase in confining pressure, B_R increases.

The mineralogical method (B_Q) (Jarvie, 2007) and the compressive and tensile strength method were also used to calculate BI (Hucka, 1974). The results are the same: BI increases with confining pressure (Table 3.2).

Rock is usually more brittle at low confining pressure and has a tendency toward ductility when confining pressure increases (Becker, 1893; Jaeger, 1976; Paterson, 2005; Holt, 2011). Microcracks decrease with an increase in confining pressure (Figure 3.7). This conflicts with the results from the BI models used above. Pore pressure influences rock mechanics parameters but it is ignored in the previous models. A new model that considers the influence of confining pressure and pore pressure in BI calculation is necessary.

Table 3.2 Test and calculation results of data 2

Sample Number	Depth (m)	Confining Pressure (MPa)	Young's Modulus (GPa)	Poisson Ratio	Compressive Strength (MPa)	Peak Strain (%)	Residual Strain (%)	BI_R	BI_{new}
H1	3359	90	52.61	0.39	209.19	1.16	1.26	0.624	0.285
H2	3393.7	60	41.4	0.31	171.92	0.72	0.85	0.618	0.382
H3	3393.7	50	38.15	0.29	143.73	0.53	0.67	0.613	0.416
H4	3233	10	23.73	0.29	42.3	0.3	0.35	0.512	0.524
H5	3362.2	10	12.13	0.29	35	0.3	0.33	0.430	0.707
H6	3359	10	25.43	0.35	42.49	0.21	0.27	0.469	0.433
H7	3219.5	10	4.92	0.62	14.78	0.42	0.43	0.079	0.040
E8	4163.1	50	34.74	0.27	214.09	1.01	1.28	0.607	0.455
E9	4164	30	20.91	0.21	40.57	0.34	0.36	0.565	0.668
E10	4164	20	19.56	0.48	40.56	0.19	0.21	0.310	0.297
E11	4164	30	14.33	0.21	37.75	0.51	0.65	0.518	0.801
B12	2171.6	60	70.4	0.41	391.25	1	1.31	0.731	0.245
L13	2071.1	80	56.58	0.26	215.13	0.38	0.46	0.770	0.364
L14	2123.4	60	48.54	0.19	210.17	0.43	0.51	0.777	0.445
L15	2229.7	15	34.48	0.21	78.5	0.21	0.3	0.660	0.516

H-Haynesville shale, E-Eagle ford shale, B-Barnett shale, L-Longmaxi shale in Sample Number H-horizontal core, V-vertical core, number behind means the angle between core direction and magnetic north in orientation

3.1.2 Methodology

In this chapter confining pressure is compared to rock mechanics parameters and the microcrack quantity of cores and the relationships are evaluated. Effective stress is introduced to provide a relationship among the confining pressure, pore pressure and fracture toughness. The confining pressure and pore pressure are introduced into the new models by replacing fracture toughness. A new model for brittleness evaluation is developed to correct the influence of confining pressure. Finally, data from experiments and oil fields is used to validate the models.

3.2 Models Considering Confining Pressure and Pore Pressure Effect

3.2.1 Fracture Toughness and Effect Stress

3.2.1.1 Fracture Toughness

Brittleness is a parameter influenced by many factors: rock mineral content, rock mechanics characteristics, in situ stress, confining pressure and a strain rate. Using Young's modulus and Poisson's ratio does not thoroughly characterize brittleness. Young's modulus increases with confining pressure and BI decreases with confining pressure. It could be speculated that there is a parameter changing with confining pressure that influences rock brittleness. Fracture toughness is explored as a possible explanation.

Fracture toughness is an important parameter that characterizes the ability of a rock with cracks to resist fracturing. It is a quantitative method that expresses the rock's resistance to a brittle fracture. It is more likely to have a ductile fracture, if the fracture toughness of a rock is high. On the contrary, a rock with low fracture toughness is more likely to have a brittle fracture (Hertzberg, 1995). Fracture toughness can be obtained by the stress intensity factor (K), where a crack in the rock begins to spread. Cracks begin to spread when K is equal or greater than the critical stress intensity factor (Kc). Kc is then named the fracture toughness which is an intrinsic property of a rock (Ko, 2007).

There are three fracture toughness numbers K_{IC}, K_{IIC}, and K_{IIIC} and they correspond to three cracking modes. IC, IIC and IIIC represent modes of cracks (Figure 3.10). IC means mode I, which forms in a tensile stress. The other two develop in shear and tear stress, respectively. Nagel (2011) used numerical simulation to demonstrate that tensile failure mainly happens during hydraulic fracturing and shear failure mainly occurs in natural fractures. K_{IC} is introduced to characterize the rock's ability to resist fracturing under the tensile stress.

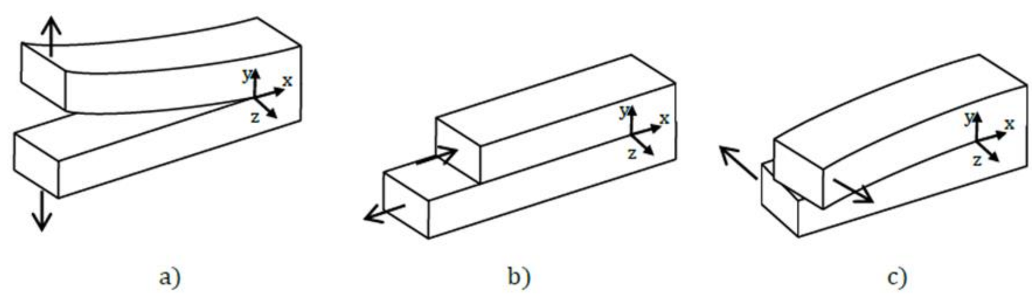

Figure 3.10 Three loading modes. a) Mode I, b) Mode II, c) Mode III (Qu, 2011)

3.2.1.2 Effective Stress

The concept of effective stress is based on the pioneering work in soil mechanics by Terzaghi (1923) who noted that the behaviour of a soil (or a saturated rock) is controlled by the effective stresses: the differences between externally applied stresses and internal pore pressure (Zoback, 2007). According to Terzaghi's study, the stress tensor of all normal components tends to decrease because of the influence of pore pressure and Mohr's circle tends to move toward the left side. The rock material stays closer to the failure envelope (Qu, 2011). The so-called "simple" or Terzaghi definition of effective stress is

$$\sigma = S - \delta P_p \tag{3-1}$$

where S is the normal components of the stress tensor, σ is the corresponding effective stress and Pp is the pore pressure. The pore pressure influences the normal components of the stress tensor, σ_{11}, σ_{22}, σ_{33} and not the shear components σ_{12}, σ_{23}, σ_{13} (Seto, 2001).

In Figure 3.11 the stresses acting on individual grains result from the difference between the externally applied normal stresses and the internal fluid pressure.

When the forces acting on a single grain contact, all of the forces are transmitted to the grain. Thus, the force balance is

$$F_T = F_{\mathrm{g}} \tag{3-2}$$

In terms of stress and area, it can be expressed as

$$S_{\mathrm{ii}} A_T = A_c \sigma_c + (A_T - A_c) P_p \tag{3-3}$$

where A_C is the contact area of the grain and σ_c is the effective normal stress acting on the grain contact. Introducing parameter a = A_C/A_T

$$S_{ii} = a\sigma_c + (1-a)P_p \tag{3-4}$$

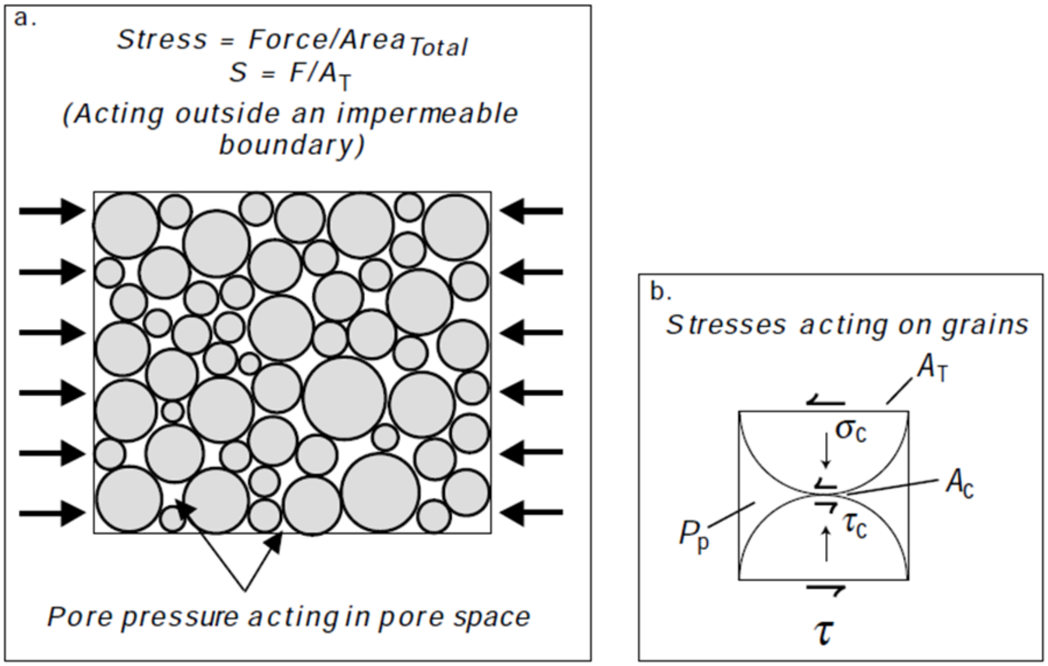

Figure 3.11 Sketch map of force analysis for grains with pore pressure (Zoback, 2007)

(a) Schematic illustration of a porous solid with external stress applied outside an impermeable boundary and pore pressure acting within the pores. (b) Considered at the grain scale, the force acting at the grain contact is a function of the difference between the applied force and the pore pressure. As A_C/A_T goes to zero, the stress acting on the grain contacts is given by the Terzaghi effective stress law.

The intergranular stress is obtained by taking the limit where *a* becomes vanishingly small:

$$\lim_{a \to 0} a\sigma_c = \sigma_g \tag{3-5}$$

such that the "effective" stress acting on individual grains, σ_g, is given by

$$\sigma_g = S_{ii} - (1-a)P_p = S_{ii} - P_p \tag{3-6}$$

for very small contact areas. In Figure 3.11b pore fluid pressure does not affect shear stress components, S_{ij}.

Figure 3.12 shows conventional triaxial strength tests on Berea sandstone and Mariana limestone by Handin (1963). In Figures 3.12a and c, the strength tests are shown without pore pressure in the manner of Figure 3.12b where the strength at failure, S_1, is shown as a function of confining pressure, S_3.

$$S_1 = c_0 + nS_3 \tag{3-7}$$

Assuming that it is valid to replace S_1 with ($S_1 - P_p$) and S_3 with ($S_3 - P_p$) in Eq. 3-7

$$S_1 - S_3 = c_0 + (1-n)P_p - (1-n)S_3 \tag{3-8}$$

Figures 3.12b and d show that the straight lines predicted by Eq. 3-8 match data exactly for the various combinations of confining pressures and pore pressures when the tests were conducted. The effect of pore pressure on rock strength is described very well by the simple (or Terzaghi) form of the effective stress law in these rocks.

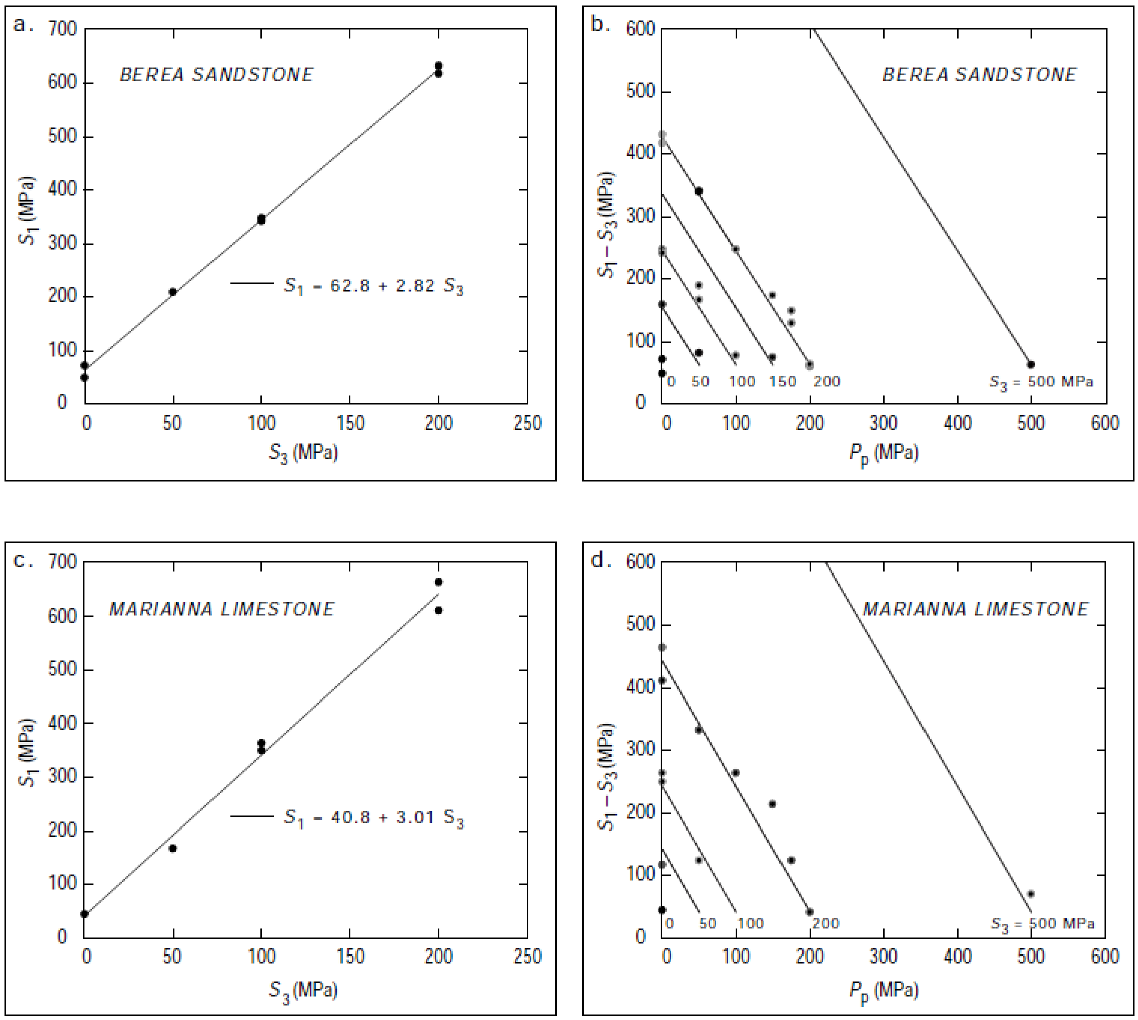

Figure 3.12 Dependence of rock strength with and without considering pore pressure

(a*) Dependence of rock strength on confining pressure in the absence of pore pressure for Berea sandstone. (b) Dependence of rock strength on confining pressure and pore pressure assuming the simple Terzaghi effective stress law (equation 3.8) is valid (straight diagonal lines). And (c) and (d) show similar data for Marianna limestone. Data derived from Handin, Hager et al. (1963).*

3.2.1.3 Relationship between Fracture Toughness and Effective Stress

An increase in confining pressure may close preexisting cracks and restrict the crack propagation. Even though both compressive and tensile strength increases with confining pressure, tensile strength plays a more important role in tensile failure which mainly happens in hydraulic fracturing. Therefore, mode I fracture toughness increases with confining pressure. This aligns with findings in previous studies (Seto, 2001; Ko, 2007).

Fracture toughness and confining pressure are shown to have a linear relationship (Figure 3.13) using fracture toughness tests (Biret, 1989; Chen, 1997; Jin, 2001). F.Biret (1989) found a linear relationship between fracture toughness and confining pressure based on samples from Indiana in the United States :

$$K_{Ic} = 0.052P_c + 0.536(R = 0.99) \tag{3-9}$$

Jin Yan (2001) got a similar linear relationship between fracture toughness and confining pressure by using artificial cores. Al-Shayea (2000) showed that fracture toughness and effective confining pressure have a linear relationship based on outcropping in the Central Province of Saudi Arabia .

$$K_{Ic} = 0.043\sigma_3' + K_{IC}{}^0(R = 0.99) \tag{3-10}$$

Using the data of shale and sandstone samples from Chen (1997), the relationship of fracture toughness and tensile strength is built:

$$K_{Ic}{}^0 = 0.0059\sigma_t{}^3 - 0.0922\sigma_t{}^2 + 0.5145\sigma_t - 0.3494 \tag{3-11}$$

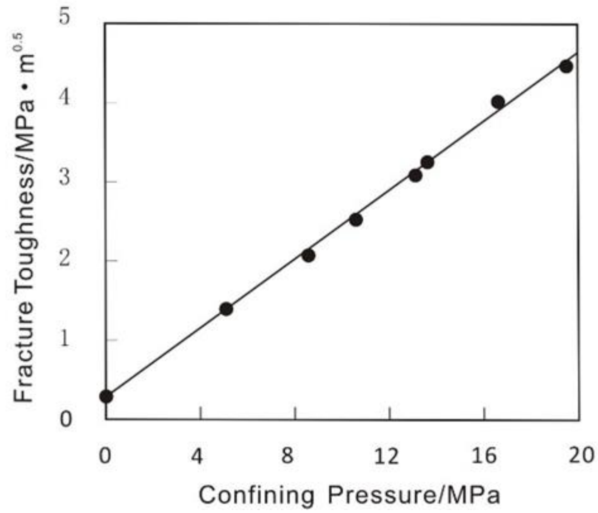

Figure 3.13 Fracture toughness vs confining pressure

Figures 3.14 and 3.15 show the results of regression analysis between tensile strength and fracture toughness. Fracture toughness is expressed in confining pressure and tensile strength.

$$K_{Ic} = 0.043P_c + 0.0059\sigma_t^{\ 3} - 0.0922\sigma_t^{\ 2} + 0.5145\sigma_t - 0.3494 (R = 0.95) \qquad (3\text{-}12)$$

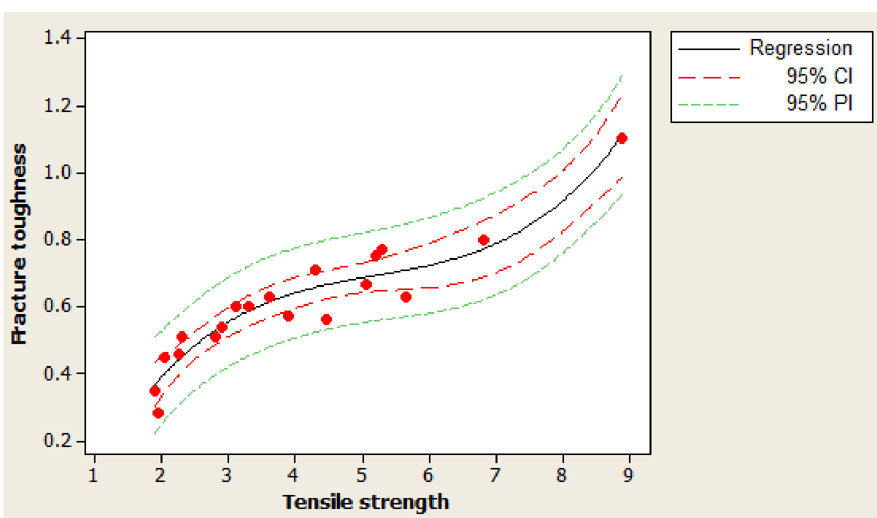

Figure 3.14 Regression analysis of tensile strength and fracture toughness

Chen (1997) determined the relationship between fracture toughness and Young's modulus/P-wave velocity/S-wave velocity in shale formation.

$$K_{Ic} = 0.054V_p + 0.3876(R^2 = 0.75) \tag{3-13}$$

$$K_{Ic} = 0.102V_s + 0.3876(R^2 = 0.80) \tag{3-14}$$

$$K_{Ic} = 3.672 \times 10^{-3} E + 0.45034(R^2 = 0.84) \tag{3-15}$$

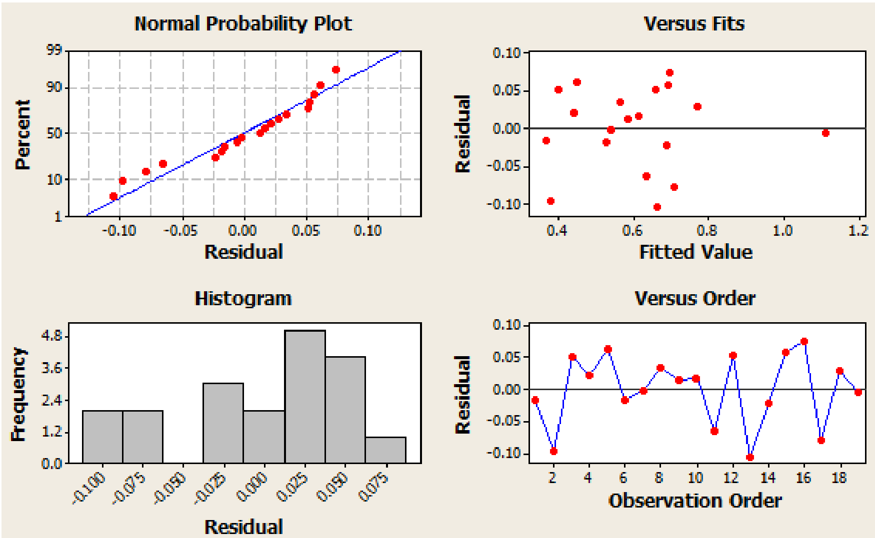

Figure 3.15 Residual plots of regression analysis

Eberhart (1989) built an empirical relationship between effective pressure and P-wave velocity/S-wave velocity.

$$V_{\mathrm{p}} = 5.77 - 6.94\phi - 1.73\sqrt{V_{\mathrm{sh}}} + 0.446(\sigma_3{}' - e^{-16.7\sigma_3{}'}) \qquad (3\text{-}16)$$

$$V_{\mathrm{s}} = 3.70 - 4.94\phi - 1.57\sqrt{V_{\mathrm{sh}}} + 0.361(\sigma_3{}' - e^{-16.7\sigma_3{}'}) \qquad (3\text{-}17)$$

$$\sigma_3{}' = P_c - P_p \qquad (3\text{-}18)$$

Bringing Eq. 3-16 and Eq. 3-17 into Eq. 3-13 and Eq. 3-14

$$K_{Ic} = 0.054[5.77 - 6.94\phi - 1.73\sqrt{V_{\mathrm{sh}}} + 0.446(\sigma_3{}' - e^{-16.7\sigma_3{}'})] + 0.3876 \qquad (3\text{-}19)$$

$$K_{Ic} = 0.102[3.70 - 4.94\phi - 1.57\sqrt{V_{\mathrm{sh}}} + 0.361(\sigma_3{}' - e^{-16.7\sigma_3{}'})] + 0.3876 \qquad (3\text{-}20)$$

Eq. 3-19 and Eq. 3-20 have a similar form with Eq. 3-10 showing that K_{IC} increases with effective pressure. Using Eq. 3-19 and Eq. 3-20, K_{IC} at different confining pressures can be calculated from well log data.

It has to be noted that most of the equations in this section are empirical equations based on data from different areas. Eq. 3-9 from F.Biret is based on samples from Indiana of the United States and Eq. 3-10 from Al-Shayea is based on outcropping in the Central Province of Saudi Arabia. They both reflect a linear relationship between fracture toughness and confining pressure, but with different empirical coefficients.

3.2.2 New Model Establishment in BI Evaluation

The components of Young’s modulus (E) and Poisson’s ratio (v) are combined to reflect the rocks ability to fail under stress and maintain a fracture once the rock fractures (Rickman, 2008).

This is valid only when confining pressure stays constant. When confining pressure increases, the ultimate tensile strength and intermolecular force of rock increase with it. The rock has more fracture energy and resistance to be fractured, the fracture toughness.

Based on the relationship between fracture toughness and confining pressure, a new model is proposed in my published research (Hu, 2015).

$$BI_{new} = \frac{\frac{BI_R}{K_{IC}} - (\frac{BI_R}{K_{IC}})_{\min}}{(\frac{BI_R}{K_{IC}})_{\max} - (\frac{BI_R}{K_{IC}})_{\min}} \tag{3-21}$$

For a series of samples, BI_R has been calculated by using the equation of Rickman (Eq. 1-1), respectively. Then normalization is done after BI_R dividing by K_{IC}.

Bring Eq. 3-9 and Eq. 3-10 into Eq. 3-21

$$BI_{new} = \frac{\frac{BI_R}{0.052P_c + 0.536} - (\frac{BI_R}{0.052P_c + 0.536})_{\min}}{(\frac{BI_R}{0.052P_c + 0.536})_{\max} - (\frac{BI_R}{0.052P_c + 0.536})_{\min}} \tag{3-22}$$

$$BI_{2-23} = \frac{\frac{BI_R}{0.043(P_c - P_P) + K_{Ic}{}^0} - (\frac{BI_R}{0.043(P_c - P_P) + K_{Ic}{}^0})_{\min}}{(\frac{BI_R}{0.043(P_c - P_P) + K_{Ic}{}^0})_{\max} - (\frac{BI_R}{0.043(P_c - P_P) + K_{Ic}{}^0})_{\min}} \tag{3-23}$$

By using Eq. 3-19 and Eq. 3-20, BI can be calculated from well log data.

$$BI_{2-24} = \frac{\frac{BI_R}{0.0541V_{\mathrm{p}} + 0.3876} - (\frac{BI_R}{0.0541V_{\mathrm{p}} + 0.3876})_{\min}}{(\frac{BI_R}{0.0541V_{\mathrm{p}} + 0.3876})_{\max} - (\frac{BI_R}{0.0541V_{\mathrm{p}} + 0.3876})_{\min}} \tag{3-24}$$

$$BI_{2-25} = \frac{\frac{BI_R}{0.1021V_{\mathrm{s}} + 0.3876} - (\frac{BI_R}{0.1021V_{\mathrm{s}} + 0.3876})_{\min}}{(\frac{BI_R}{0.1021V_{\mathrm{s}} + 0.3876})_{\max} - (\frac{BI_R}{0.1021V_{\mathrm{s}} + 0.3876})_{\min}} \tag{3-25}$$

These models consider the influence of Young's modulus, Poisson's ratio, tensile strength, fracture toughness, and confining and pore pressure in brittleness evaluation. They can be used to compare rock brittleness relatively based on the existing empirical coefficients. It is more accurate to recalculate the empirical coefficients by using the local data.

3.3 Case analysis and validation

According to the analysis above, brittleness indices from previous and new models are calculated using data 1 and data 2 (Tables 3.1 and 3.2). Data and experiments are described in Appendix A. BI_J and BI_R in data 1 are brittleness indices from the models of Jarvie and Rickman, respectively. BI_{3-23}, BI_{3-24} and BI_{3-25} are calculated by using Eq. 3-23, Eq. 3-24 and Eq. 3-25, respectively. Tensile strength is not measured in data 2. Therefore, Eq. 3-15 is used to calculate K_{IC}. BI_{new} in data 2 is calculated by using Eq. 3-22.

The results show that brittleness indices in data 1 generally increase as the content of quartz increases. This reflects the influence of the brittle mineral. The results of BI_J and BI_R in data 1 demonstrate the brittleness index of the same sample under different confining pressure is almost the same. The results of BI_{3-23}, BI_{3-24} and BI_{3-25} in data 1 show that the brittleness index of the same sample is usually greater at low confining pressure than that at high confining pressure (Tables 3.1). BI_R, $BI_{3\text{-}23}$, $BI_{3\text{-}24}$ and $BI_{3\text{-}25}$ of sample 3 are larger than that of sample 2, displaying the influence of elastic modulus.

The models are validated by comparing the results with experimental data. Figure 3.7 has the microcrack numbers of samples. The three largest are H5, E9 and E11 and they correspond to the values of BI_{new} with 0.707, 0.668 and 0.801, respectively (Table 3.2). The microcrack numbers for samples H4 and L15 are in the second place (Figure 3.7) with BI_{new} 0.524 and 0.516, respectively (Table 3.2). The results from the new models match well with experimental results, validating the new models.

3.4 Conclusions

(1) Rock is usually more brittle at low confining pressure and has a tendency toward ductility when the confining pressure increases. This conflicts with existing models for BI calculation.

(2) The effective stresses in a reservoir decrease with elevated pore pressure. This may reduce the influence of the confining pressure and increase the brittleness of the rocks.

(3) The new model considers the influence of Young's modulus, Poisson's ratio, tensile strength, pressure and fracture toughness. The BI calculation matches well with experimental results and can be built by using conventional data like well logs.

4. Brittleness Evaluation considering Temperature

In this chapter, the focus is on the first limitation, the effect of temperature on brittleness evaluation. The outcome is to establish a model that considers the influence of temperature. We first show the existing problems that need to be fixed and details of the methods used to establish the new model are reviewed. Then, a new model is established based on experimental data and the methods. Part of this research has been published in AAPG annual convention 2016 with me as the first author (Hu, 2016).

4.1 Existing Problems and Methodology

4.1.1 Existing Problems

Temperature has a significant impact value of the rock mechanics parameters. Since ancient times, man has been interested in the possibility of strengthening or weakening rocks under the influence of temperature (Sygała, 2013).

The influence of temperature on rock brittleness is controversial. It is generally agreed that there is a visible decrease of strength and an increase in ductility at elevated temperatures. Dimitriyev (1969) noted that when rocks like clay and kaolin are exposed to high temperatures, their resistance increased several times with a simultaneous reduction of their plasticity. Ying (2012) also shows that temperature increases the degree of sandstone fragmentation by uniaxial stress tests. To establish a model of brittleness evaluation that considers temperature, the influence of increased temperatures on changes to the texture and geomechanical properties of rocks must first be analyzed.

Shale reservoirs are full of gas, oil and/or water, creating significant pore pressure, especially when the reservoirs are under high temperature. When pore pressure is considered in undrained conditions, like that of a shale gas reservoir, the status of temperature should be reevaluated. Figures 4.8 and 4.9 show the influence of pore pressure on rock mechanics properties.

Based on the discussion above, three problems have been proposed:

1. How does temperature impact pore pressure and rock mechanics properties of shale/tight sandstone?
2. What is the relationship between temperature and pore pressure?
3. How is a relationship between temperature and rock brittleness established?

4.1.2 Methodology

Rock strength is determined on the basis of mineral composition, structural and textural characteristics, porosity, fracturing, the strength of given mineral constituents and the nature of the bonding between them. The same factors determine the strength of rocks under increased temperature (Dimitriyev, 1969; Chmura, 1992; Sygała, 2013).

In this chapter, the research is focused on the influence of temperature on rock texture and pore pressure. Macrostructural and microstructural characteristics of shale samples at different temperatures are analyzed. The thermo-poroelasticity theory is introduced to determine a relationship between temperature and pore pressure. The finding is combined with the outcomes from Chapter 3, and a relationship between temperature and rock brittleness is established.

Experimental data from Zhang (2013) and Liu (2000) is analyzed in this research. In the analysis of a uniaxial compression test, scanning electron microscope (SEM) and X-ray diffraction, the mechanical properties, texture and rock mechanics properties of rocks are obtained. Stress-strain curves of shale samples at temperatures from 25℃ to 800℃ are used to analyze the temperature dependency of the elastic modulus, ultimate strength and strain. The shape of stress-strain characteristics expressed during the destruction of the rock samples due to temperature impact under uniaxial compression is discussed.

4.2 Effect of Temperature on Rock Texture

4.2.1 Macrostructural Characteristics of Shale at Different Temperatures

Figures 4.1 and 4.2 provide the stress-strain characteristics of shale samples from 25°C to 800°C. From the post-failure curve, a gradual increase in the damaging stress to 400°C (maximum) is evident. The pre-failure stress–strain curves for temperatures up to 200°C do not differ in shape and have considerable elastic deformation. The values of Young's modulus do not differ significantly. In the temperature range of 400-800°C, the values of Young’s modulus visibly decrease. In Figure 4.1 higher temperature shale exhibits higher values of axial-failure strain and total deformation. Yin (2012) and Ranjith (2012) found the same trend with sandstone. Some researchers attribute this phenomenon to the transition of rocks from a brittle model into a ductile model (Sygała, 2013).

The pictures of shale fractures after failure shown in Figure 4.3 illustrate the fracture degree of shale samples under different temperatures. There is no significant difference in fracture degree when temperature is less than 200°C. The degree of rock fragmentation at 600℃ is greater than at 25℃. This trend increases with increasing temperature reflecting the influence of temperature on rock brittleness. When temperature is > 600℃, rocks become more brittle as temperature increases.

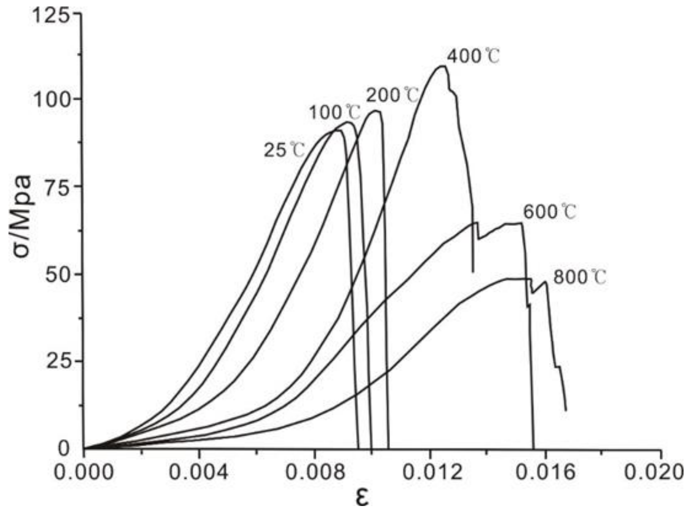

Figure 4.1 Stress-strain curves of shale at different temperatures

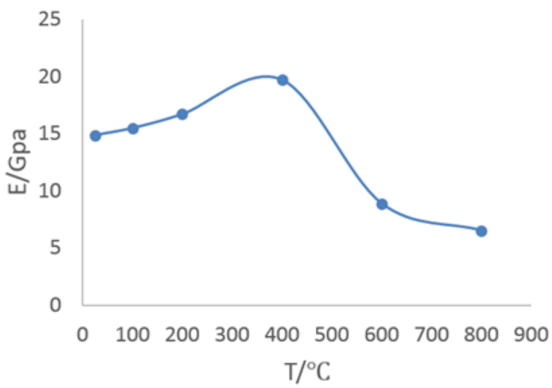

(a) E vs T

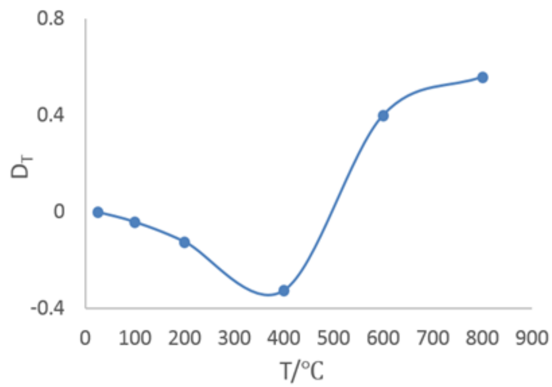

(b) DT vs T

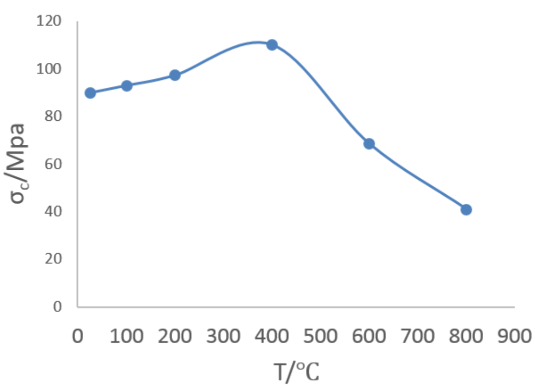

(c) σ_c vs T

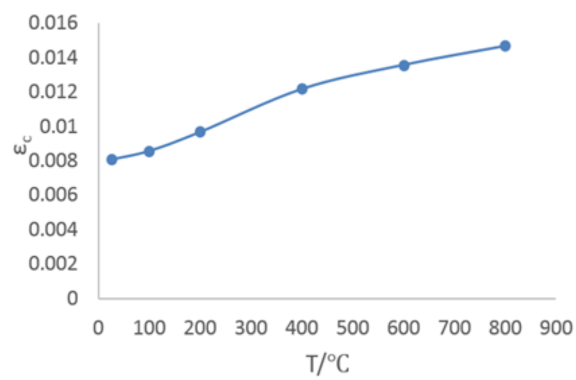

(d) ε_c vs T

Figure 4.2 Influence of temperature on rock mechanics parameters

(a) 25℃ (b) 100℃ (c) 200℃

(d) 400℃ (e) 600℃ (f) 800℃

Figure 4.3 Influence of temperature on rock failure (Liu, 2000)

The concept of thermal damage is proposed, given that the modulus of elasticity is presented in Reference (Chmura, 1992) as a parameter of thermal damage D(T). It is defined as follows:

$$D(T) = 1 - \frac{E_T}{E_0} \tag{4-1}$$

where E_T is the modulus of elasticity at T℃ and E_0 at T=25℃. In Table 4.1 thermal damage increases rapidly when temperature goes up to 600℃ (Figure 4.2b).The same trend is found in Figure 4.3.

Table 4.1 Rock mechanics parameters at different temperatures

T/°C	25	100	200	400	600	800
E/GPa	14.89	15.51	16.72	19.75	8.91	6.54
σ_c/MPa	90.06	93.12	97.42	110.42	68.78	41.15
ε_c	0.0081	0.0086	0.0097	0.0122	0.0136	0.0147
D_T	0	-0.042	-0.123	-0.326	0.402	0.561

4.2.2 Microstructural Characteristics of Shale at Different Temperatures

In this section, SEM pictures (Figure 4.4) are used to analyze the microstructural characteristics of shale at different temperatures.

4.2.2.1 Porosity

The porosity development is substantial in shale samples at 25℃ and decreases as temperature increases (Figure 4.4). There are no distinct pores from the SEM pictures at temperature > 600℃ (Figure 4.6d and e) visible. The pore size decreases as the temperature increases.

4.2.2.2 Microcrack

The development of microcracks is impacted differently by temperature. In low temperatures, there are not many microcracks and most are intercrystalline cracks (Figure 4.4a and b). The number of microcracks increases with an increase in temperature, especially when temperature is > 600℃ (Figure 4.4d and e).

From the description above, pore density (the number of pores per mm^2) decreases with an increase in temperature when temperature is < 400℃. The number of microcracks increases with an increase in temperature when temperature is > 400℃ (Figure 4.4).

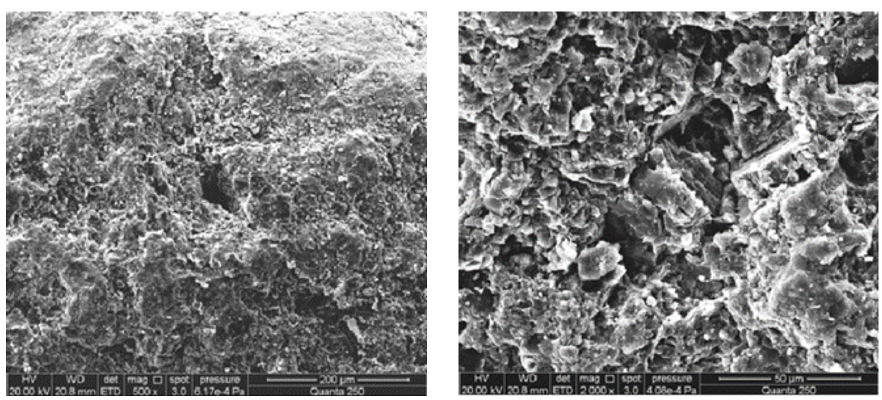

(a) 25℃

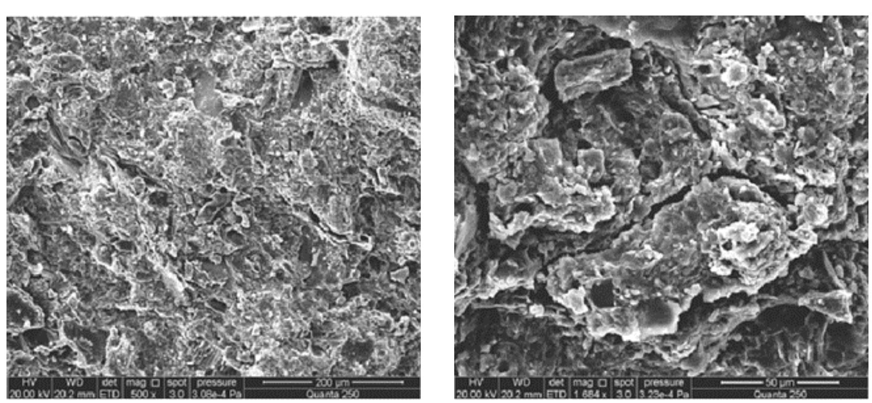

(b) 200℃

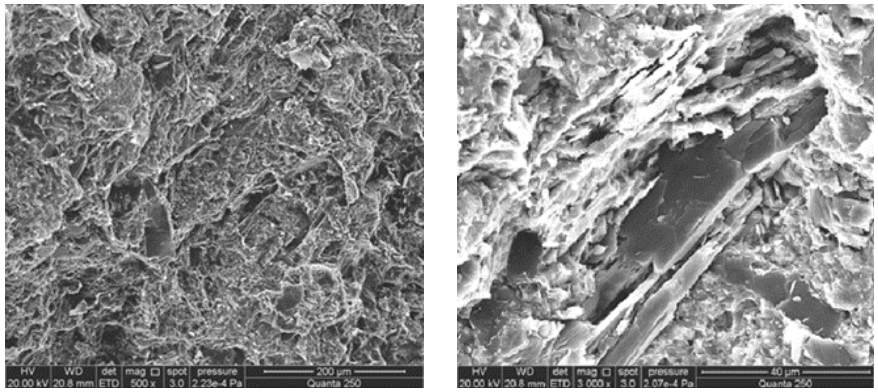

(c) 400℃

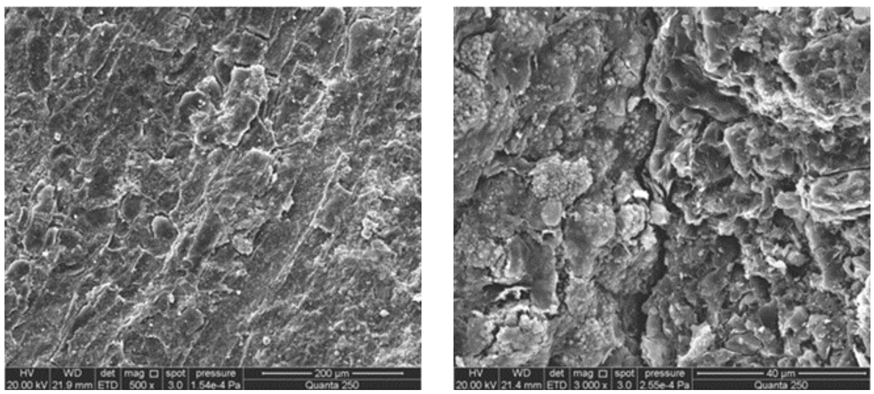

(d) 600℃

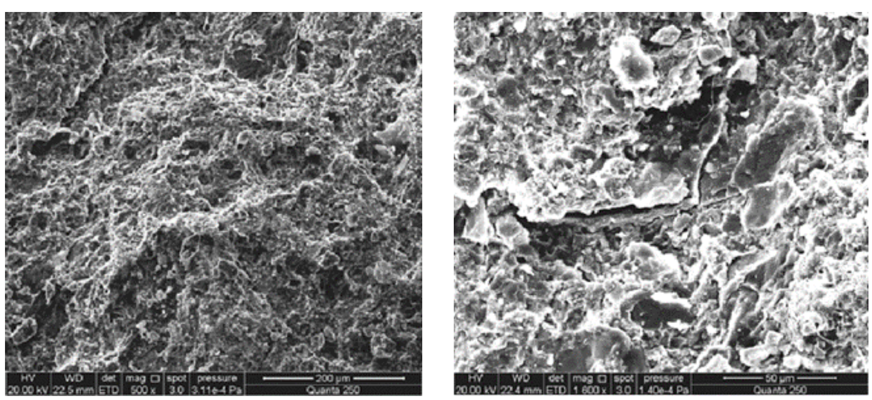

(e) 800℃

Figure 4.4 Microstructural characteristics of shale at different temperatures (Liu, 2000)

4.2.3 Discussion

Here is the contradiction identified previously. According to the change of Young’s modulus and the results of uniaxial compression tests (Figure 4.3), the brittleness of a shale sample increases with temperature, while, in terms of axial-failure strain and total deformation, plastic deformation of shale samples also increases with temperature (Figure 4.1).

In the case of temperature impact on rock, one factor influencing its strength is the thermal expansion of minerals included in the composition of the shale rock. In fine-grained sandstone or shale, an increase of compressive strength occurs earlier and is longer than in coarse-grained sandstones of greater porosity. This behaviour is attributed to a change in thermal expansion of minerals. Under the influence of temperature, depending on the coefficient of the thermal expansion of mineral components, an increase of contact surfaces between particles takes place. This leads to structural changes that have an impact on the change of the values of strength parameters and the bulk density of the rock (Dimitriyev, 1969; Chmura, 1992; Wan, 2009). Figure 4.5 demonstrates that a thermal expansion coefficient increases with temperature. Intergranular fractures and cracks develop when temperature is at a certain degree. In addition to structural deformation, there are changes to physical properties (shape change, volume, mass, and velocity of propagation of elastic waves through the rock medium) caused by the hydration or dehydration and decarbonization of rocks. It is a little bit like the change of clay with temperature. When clay is fired to a high temperature it will become a kind of pottery or ceramic with higher brittleness.

Therefore, under the influence of temperatures in the rock, thermal stress appears which gives rise to numerous micro-cracks, which then gradually expand as the temperature rises. This leads to a weakening of the rocks' strength and their gradual destruction (Sygała, 2013). We will further analyze this question in terms of energy in Chapter 6.

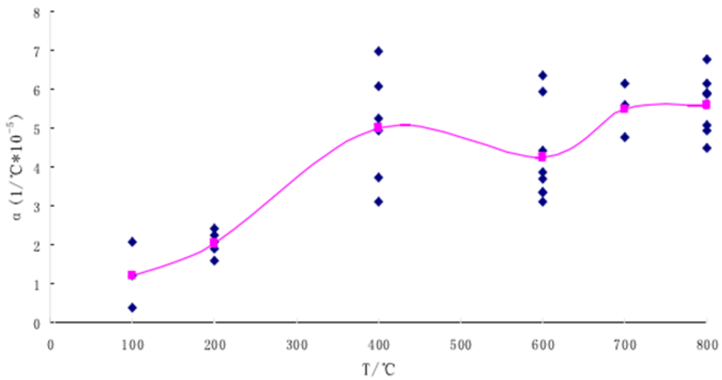

Figure 4.5 Change curves of thermal expansion coefficient with temperature (Liu, 2000)

Note that the influence of temperature on rock texture is prominent only at high temperature (over 400℃). However, the temperature of shale gas or tight oil reservoirs underground is usually less than 200℃. Therefore, the influence of temperature on rock texture above could be ignored in brittleness evaluation of unconventional reservoirs.

4.3 Effect of Temperature on Pore Pressure

4.3.1 Experimental Modelling

It is difficult to measure the change of pore pressure with temperature inside a rock. Gay-Lussac's Law (or the Pressure Law) by Joseph Louis Gay-Lussac in 1809 states that for a fixed mass of gas, at a constant volume, the pressure (P) is directly proportional to the absolute temperature (T).

$$\frac{\text{Pressure}}{\text{Temperature}} = C_{\text{constant}} \tag{4-2}$$

An experiment from GCSE Physics is introduced to prove this relationship. Figure 4.6 shows a sealed cylinder with no leaks that contains a fixed mass. The volume of the gas is kept constant by using a cylinder with a fixed roof capable of withstanding high pressures. The gas pressure is created by the collision of the moving gas particles with each other and against the walls of the cylinder.

The set up used to investigate the relationship between temperature and pressure for a gas is outlined here. Heat energy is applied to the cylinder and the temperature of the gas increases. The average velocity of the gas particles increases resulting in an increase in the rate of collisions and the average force per collision. Because the areas of the walls are kept constant, the force per unit area increases driving an increase in pressure.

Plotting the pressure (P) against the absolute temperature (T) is a straight line where extrapolated measures pass through the origin. The pressure of the gas is directly proportional to the absolute temperature of the gas. Doubling the temperature will double the pressure for a fixed mass of gas at constant volume. The gradient of the slope is the constant in Charles' Law. If the gas is cooled to absolute zero then the energy of the molecules are also at the lowest energy state and, therefore, cannot generate pressure.

For real gas, the molecule volume of a gas and Van der Waals' force are considered.

$$(P + \frac{a}{V_0^{\,2}})(V_0 - b) = \mathrm{RT} \tag{4-3}$$

where P is the pressure, T is the temperature, R is the ideal gas constant and V_0 is the molar volume.

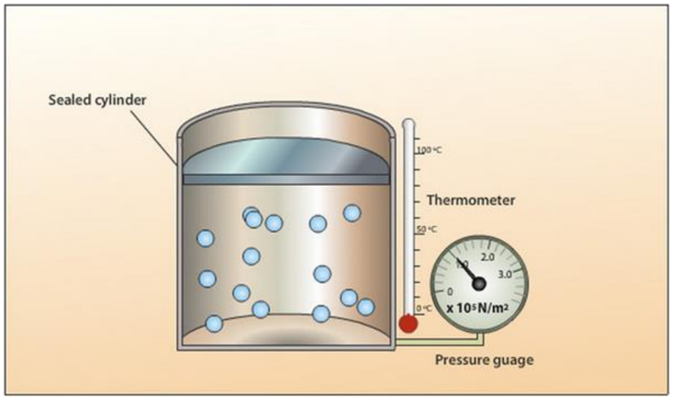

a. Before heating

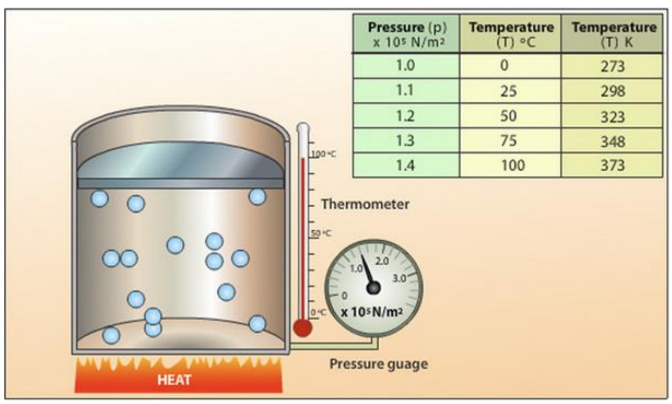

b. After heating

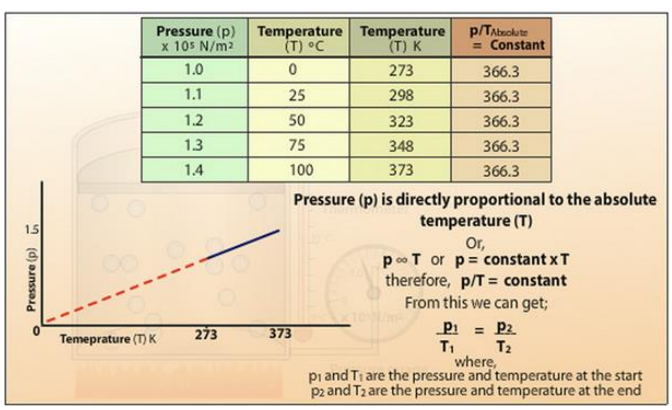

c. Data analysis

Figure 4.6 Experimental process of Gay-Lussac's Law (from GCSE Physics)

Parameters a and b are determined empirically for each gas, or are estimated using critical temperature (T_c) and critical pressure (P_c):

$$a = \frac{27R^2T_c^{\ 2}}{64P_c} \tag{4-4}$$

$$b = \frac{RT_c}{8P_c} \tag{4-5}$$

In reality, the pressure inside the cylinder increases with an increase in temperature.

4.3.2 Analytic Models

In porous media, the relationship between pressure and temperature is more complicated. Porosity, thermal expansivity, compressibility, vertical stress and elastic modulus are considered. Based on thermo-poroelasticity equations, Higgs (1991) derived expressions for changes of porosity in an open system (Bradley, 1994).

$$\mathrm{d}\phi = [\frac{1}{M} - (1-\phi) f \beta_g](dS - dP_p) + \{[\frac{K}{M} - (1-\phi)]\beta_g - \phi\beta_f\}dP_p - \{[\frac{K}{M} - (1-\phi)]\alpha_g - \phi\alpha_f\}dT \tag{4-6}$$

Here ϕ is porosity, M is axial modulus, *f* is empirical factor, S is total vertical stress, K is bulk modulus, P_p is pore pressure, β_g is grain compressibility, β_f is fluid compressibility, T is temperature, α_g is grain cubic thermal expansivity, α_f is fluid cubic thermal expansivity.

In addition, for changes of pressure in a closed system (Bradley, 1994)

$$\mathrm{dP_p} = \frac{[1-(1-\phi)Mf\beta_g]dS + [\phi M\alpha_f - K\alpha_g + (1-\phi)M\alpha_g]dT}{\phi M\beta_f + 1-(1-\phi)Mf'\beta_g - K\beta_g + (1-\phi)M\beta_g} \tag{4-7}$$

If we ignore the change in overburden stress (dS=0) and other coefficients are constant, then

$$\mathrm{P_p} = \frac{[\phi M\alpha_f - K\alpha_g + (1-\phi)M\alpha_g]T}{\phi M\beta_f + 1-(1-\phi)Mf\beta_g \text{-} K_g\beta_g + (1-\phi)M\beta_g} + \mathrm{c} \tag{4-8}$$

$$BI = \frac{\dfrac{BI_R}{0.043(\sigma_3' - P_P) + K_{Ic}{}^0} - \left(\dfrac{BI_R}{0.043(\sigma_3' - P_P) + K_{Ic}{}^0}\right)_{\min}}{\left(\dfrac{BI_R}{0.043(\sigma_3' - P_P) + K_{Ic}{}^0}\right)_{\max} - \left(\dfrac{BI_R}{0.043(\sigma_3' - P_P) + K_{Ic}{}^0}\right)_{\min}} \tag{4-9}$$

Bringing Eq. (4-8) into Eq. (4-9), the relationship between temperature and BI is apparent.

4.4 Conclusions

(1) Porosity decreases with an increase in temperature while microcracks increase with an increase in temperature, and the shale samples become more brittle.

(2) Since the thermally induced microcrack is inconspicuous under 200℃, a thermal cause of abnormally high pore pressure cannot be ignored in brittleness evaluation of unconventional reservoirs.

(3) The relationship between temperature and pore pressure can be expressed based on thermo-poroelastic equations.

5. Weights of Brittle Minerals and Rock Mechanics Parameters

In this chapter, we focus on the second limitation: the definition of brittle minerals and the weight of each parameter in the existing models of brittleness evaluation. The existing problems that need to be fixed and the details of the methods used to establish models are given. New models are established based on experiment data and the methods. Part of this research has been published in SPE Asia Pacific Unconventional Resources Conference 2015 with me as the first author (Hu, 2015).

5.1 Existing Problems, Available Data Set and Methodology

5.1.1 Existing problems

5.1.1.1 Definition of brittle mineral

It is imprecise to calculate BI by considering quartz (or dolomite) as the only brittle mineral. Quartz is not the only brittle mineral in shale. Feldspar, dolomite and calcite may also be considered brittle minerals. Whether they should be considered brittle minerals in BI prediction is controversial. Previous studies compared the calcite content with Young's modulus and Poisson's ratio and found an increase in calcite content increases Poisson's ratio and lowers Young's modulus (Jarvie, 2007; Rickman, 2008). The conclusion drawn is that calcite should not be considered a brittle mineral in BI prediction.

Most of the shale gas reservoirs found in early exploration are siliceous. Quartz is the primary brittle mineral in these reservoirs and plays a predominate role in determining BI. It is reasonable to calculate BI using Eq. 1-2 (Coates, 1966). Developed unconventional oil and gas reservoirs like Eagle Ford are rich in carbonate minerals (including calcite and dolomite). If the carbonate minerals in those reservoirs are ignored, the value of BI is significantly underestimated.

5.1.1.2 Weight coefficients of elastic modulus and brittle minerals

The weight of each parameter in models based on elastic modulus and mineralogy is not clear. Wang et al. (2009) suggested adding dolomite as a brittle mineral in BI calculation (Eq. 1-3). They did not consider the weights of quartz and dolomite and they ignored the role of calcite. Quartz, dolomite and calcite are different minerals with different properties of hardness, density and molecular structure. They do not play the same role in BI prediction. If they are treated equally (without weighting) the BI calculated is not accurate. Similarly, the weights of Young's modulus and Poisson's ratio in BI prediction are undefined (Eq. 1-1). It is imperative to discuss if carbonate minerals should be considered as a brittle mineral and how much weight should be given to each recognized brittle mineral, and the rock mechanics parameters to ensure BI prediction are more accurate.

5.1.2 Available data set

Three different types of data have been used in this study to determine an accurate model. Data 1 is the rock physics (Young's modulus and Poisson's ratio) trends for varying mineralogy from Cho (2014). They are measured under an ideal condition, where external factors are ignored (Figure 5.1).

Data 2 is a sample analysis of the Woodford shale formation from the Colorado School of Mines. An analysis based on a core of 80 m from the Reliance Triple Crown (RTC) #1 well is available. Previous studies (Harris, 2009; Hemmesch, 2009; Mnich, 2009; Aoudia, 2010) analyzed more than 150 samples from this core including lithology, mineral composition, total organic carbon (TOC) content and geochemistry. Five lithofacies are distinguished: black shale, massive carbonate, siltstone, massive grey mudstone and laminated carbonate (Hajiabdolmajid, 2003). Figure 5.2 is the mineral composition and content of the samples. A handheld acoustic velocity probe (Batzle, 1992) was used to obtain shear (Vs) and compressional (Vp) signals along the core. Figures 5.3 and 5.4 show Young's modulus (E) and Poisson's ratio (ν), respectively, from the core measurements using the dipole sonic log. Data 3 is samples from Eagle Ford (Table 5.1), used to validate the new models.

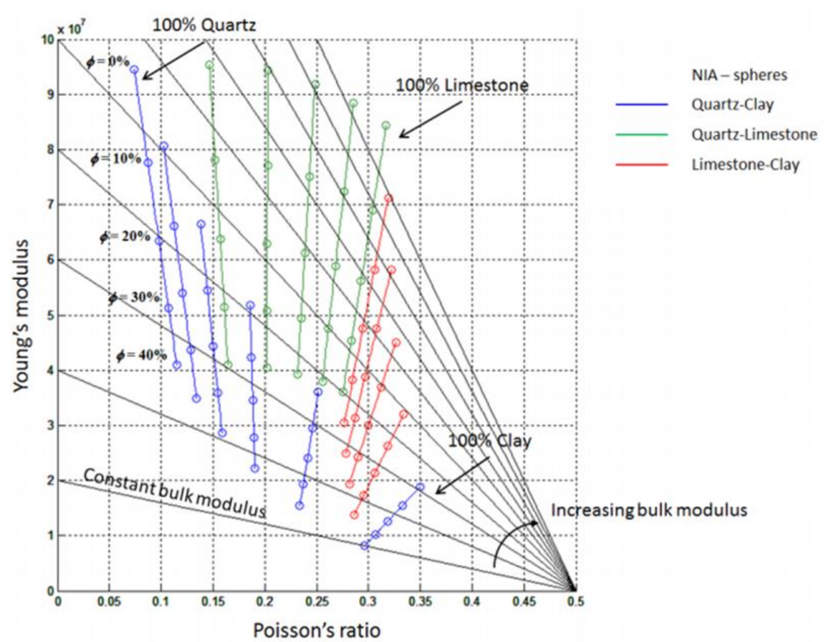

Figure 5.1 Rock physics trends for varying mineralogy and porosity (Cho, 2014)

5.1.3 Methodology

In this chapter, the influence of carbonate minerals on Young's modulus, Poisson's ratio and BI is analyzed by comparing them to quartz and clay to determine if carbonate minerals like calcite should be considered as brittle minerals in BI prediction. A new model of BI is proposed to characterize the weight of each brittle mineral. Based on the least squares method, optimal values of weight coefficients are obtained by iteration. The weight coefficients of the rock mechanics parameters are obtained by matching Young's modulus and Poisson's ratio with BI calculated using the new mineralogical model. A case analysis and validation are performed to make sure the new model is applicable.

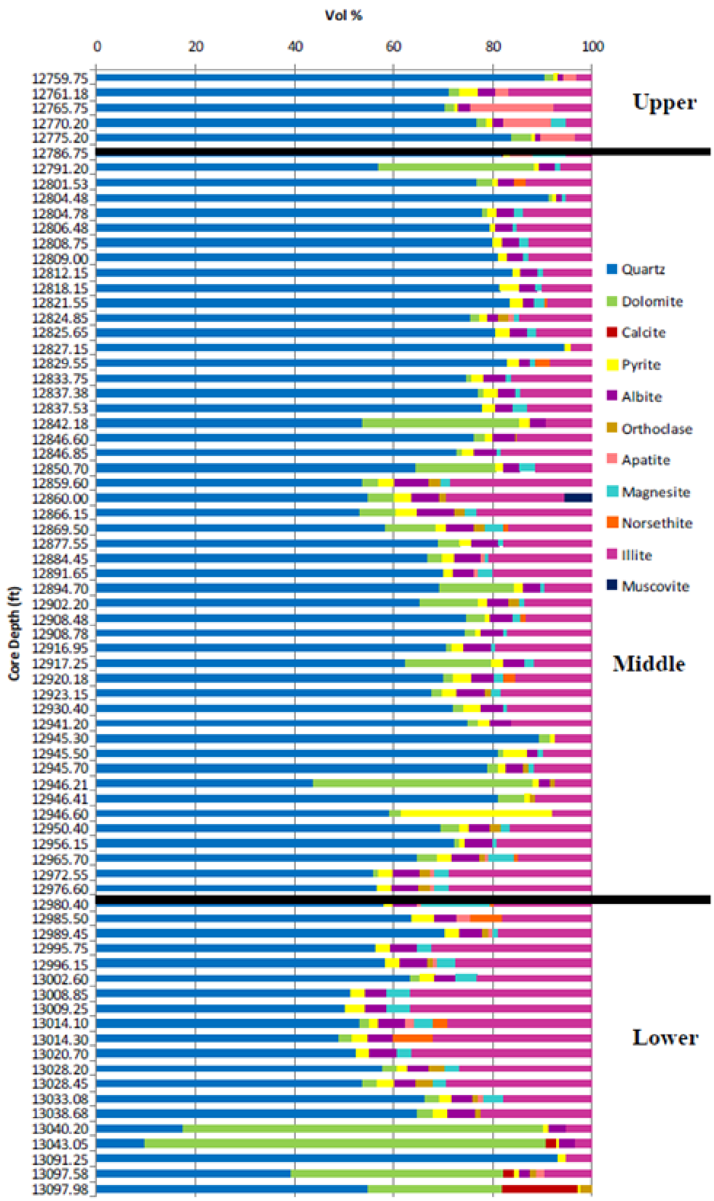

Figure 5.2 Mineralogy of the samples from the Woodford Shale (Aoudia, 2010)

Table 5.1 Data 3 from Eagle Ford

Sample Number	Quartz (%)	Calcite (%)	Clay (%)	BI_{Jarvie}	BI_{wang}	BI_{Q_new}
1	0.209	0.615	0.165	0.209	0.209	0.601
2	0.218	0.497	0.275	0.218	0.218	0.555
3	0.270	0.305	0.408	0.270	0.270	0.503
4	0.151	0.295	0.542	0.151	0.151	0.418

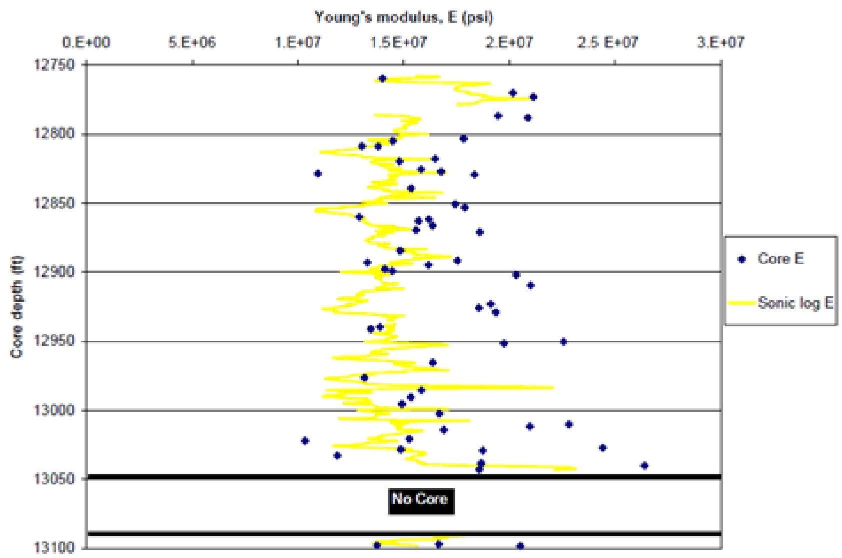

Figure 5.3 Log and core Young's modulus for the RTC well 1, Woodford shale (Aoudia, 2010)

Data 1 is used to weigh the influence of calcite on Young's modulus, Poisson's ratio and BI by comparing with quartz and clay. Based on the result, two ideal models (a new mineralogical model and a new elastic modulus model) of BI that consider the influence of calcite, the weight of each brittle mineral and rock mechanics parameters (Young's modulus and Poisson's ratio), respectively, are developed. A relationship between the two models is built.

The weight coefficients of the brittle minerals is obtained by a regression analysis. Based on the least squares method, the iteration continues until the optimal values of the weight coefficients are obtained. The weight coefficients of brittle minerals form the new mineralogical model. The BI from the new mineralogical model is used to calculate the weights of Young's modulus and Poisson's ratio. The BI from the new elastic modulus model helps to optimize the weight coefficients of the mineralogical model. After repeating iterations between the new mineralogical model and the new elastic modulus model of BI, the weight coefficients of the two models reach optimal values.

Data 2 is used to obtain the mineralogical model and elastic modulus model of BI in field conditions using the same method. Data 3 is used to validate the new models.

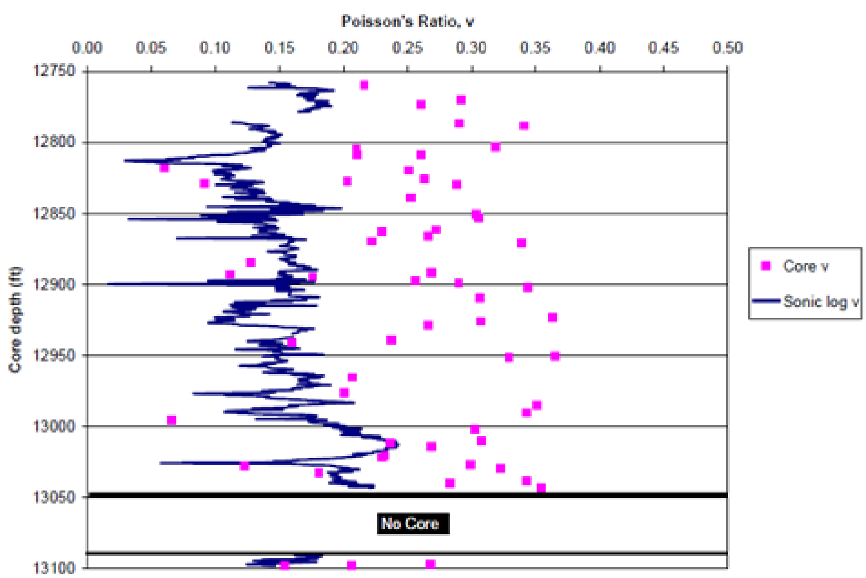

Figure 5.4 Log and core Poisson's ratio for the RTC well 1, Woodford shale (Aoudia, 2010)

5.2 Weight Analysis of Brittle Minerals and Rock Mechanics Parameters

5.2.1 Influence of calcite on brittleness evaluation

Figure 5.1 shows the rock physics trends from Poisson's ratio and Young's modulus in space with constant lines of the bulk modulus (Cho, 2014). It demonstrates that an increase in quartz content lowers Poisson's ratio and increases Young's modulus. The contrary is also true; an increase in clay content increases Poisson's ratio and lowers Young's modulus. Calcite is more complicated. Compared to clay, an increase in calcite content lowers Poisson's ratio and increases Young's modulus. This is totally opposite when compared to quartz. This means that the ability of calcite as a brittle mineral is between quartz and clay. The weight of calcite in BI calculation is assumed to be less than that of quartz.

A regression analysis is executed for the brittle minerals (quartz and calcite) and rock mechanics parameters (Young's modulus, Poisson's ratio and BI), respectively. Eq. 5-1 and Eq. 5-2 express that an increase of calcite increases both Young's modulus and Poisson's ratio. It improves the BI by increasing Young's modulus but reduces BI by increasing Poisson's ratio. The increase of Young's modulus when influenced by calcite is much greater than that of the Poisson ratio. In Eq. 5-3 BI increases with the content of calcite, even though the weight of calcite is less than that of quartz. In conclusion, calcite behaves as a brittle mineral and improves rock brittleness as a whole.

$$E = 77.5 \times Qz + 65.769 \times Cal + 19.449 \quad \text{with } R^2=0.997 \tag{5-1}$$

$$\text{v} = -0.253 \times Qz + 0.007 \times Cal + 0.323 \quad \text{with } R^2=0.957 \tag{5-2}$$

$$BI = 0.620 \times Qz + 0.316 \times Cal + 0.265 \quad \text{with } R^2=0.975 \tag{5-3}$$

where Qz and Cal are the contents of quartz and calcite, respectively. E is Young modulus and *v* is Poisson ratio.

5.2.2 Ideal models

In this section, BI models are calculated by using data in experiment conditions (Figure 5.1). These are considered ideal models.

As discussed above, calcite behaves as a brittle mineral and improves BI (Eq. 5-3). Quartz has more ability to improve BI than calcite. Calcite should be added into the model and the weight of each brittle mineral should be considered to distinguish the influence of quartz and calcite. Dolomite plays a more important role in BI prediction than calcite (Wang, 2009). If calcite is considered as a brittle mineral in BI prediction, dolomite should also be included.

The new mineralogical model of BI is

$$BI_{Q\_new} = \frac{a' \cdot Qz + b' \cdot Dol + c' \cdot Ca}{Total} \tag{5-4}$$

where *a'*, *b'*, and *c'* are the weight coefficients of quartz, dolomite and calcite, respectively. When *a'*= *b'*=1 and *c'*=0, Eq. 5-4 and Eq. 1-3 (the model from Wang, 2009) are the same. Feldspar is also a brittle mineral, but the content was very low in the samples used and so it was not considered.

The elastic modulus model of BI is rebuilt to include the weights of Young's modulus and Poisson's ratio

$$BI_{R\_new} = k \cdot E + (1-k) \cdot \nu \quad (1 \geqslant \text{k} \geqslant 0) \tag{5-5}$$

where k and 1-k are the weight coefficients of Young's modulus and Poisson's ratio. When k=0.5, Eq. 5-5 and Eq. 1-1 (the model from Rickman, 2008) are the same.

The data used is from the same formation in the same area. The stress field, structure and sedimentary environment are similar for the shale samples (Portas, 2010; Nikki, 2014). The confining pressure change for the 80m core is about 0.8 MPa with a pressure gradient of 0.01MPa/m. The diagenesis, tectonic condition, sedimentary environment and confining pressure are also assumed to be the same.

A linear relationship between BI_Q and BI_R is assumed:

$$BI_{R\_new} = m \cdot BI_{Q\_new} + n \tag{5-6}$$

Combining Eq. 5-4, Eq. 5-5 and Eq. 5-6, the relationship between E, v and each mineral composition is

$$\text{k} \cdot E + (\text{1-k}) \cdot v = \frac{a \cdot Qz + b \cdot Dol + c \cdot Ca}{Total} + n \tag{5-7}$$

Data 1 is used to determine the weight coefficients *a*, *b*, *c*, k and n. Since dolomite is not considered in data 1, b equals 0. Based on the least squares method, the iteration continues until the optimal values of the weight coefficients are obtained. Statistic Package for Social Science (SPSS) software is used to complete the iteration.

Table 5.2 provides the weight coefficients of the mineralogical model (*a*, *c*, n and k) in each iteration. The weight coefficient k increases gradually from 0.5 to 0.709 with each iteration. This can be interpreted to mean that Young's modulus plays a more important role than Poisson's ratio in BI prediction. The value of *a*/*c* decreases from 1.96 to 1.53 with each iteration indicating that the role of calcite in BI prediction increases in importance. This is because calcite has a greater influence on Young's modulus than Poisson's ratio as determined above. An increasing weight of Young's modulus requires calcite to play a more important function in BI prediction or the weight of Poisson's ratio will increase. Young's modulus plays a more significant role than Poisson's ratio in BI prediction and this is reasonable from the point of mineralogy.

Table 5.2. Iteration history of weight coefficients, data 1

Iteration Number	a		c		n		k	
	Estimate	Std.Error	Estimate	Std.Error	Estimate	Std.Error	Estimate	Std.Error
0.0	1		1		1		0.5	
1.0	0.62	0.04	0.316	0.04	0.265	0.018	0.518	0.024
2.0	0.566	0.06	0.313	0.06	0.268	0.039	0.546	0.034
3.0	0.578	0.056	0.332	0.056	0.256	0.037	0.572	0.032
4.0	0.588	0.053	0.351	0.053	0.245	0.035	0.597	0.031
5.0	0.599	0.05	0.368	0.05	0.234	0.033	0.62	0.029
6.0	0.608	0.047	0.384	0.047	0.224	0.031	0.641	0.028
7.0	0.617	0.044	0.399	0.044	0.215	0.029	0.661	0.027
8.0	0.667	0.015	0.423	0.015	0.199	0.01	0.672	0.019
9.0	0.67	0.015	0.431	0.015	0.195	0.01	0.682	0.018
10.0	0.673	0.014	0.437	0.014	0.191	0.009	0.692	0.018
11.0	0.676	0.014	0.443	0.014	0.187	0.009	0.703	0.017
12.0	0.678	0.014	0.449	0.014	0.183	0.009	0.709	0.017

Table 5.3 shows that the R squared of the BI_{Q_new} model, BI_{R_new} model and BI_{Q_new} model vs BI_{R_new} increases with each iteration. This indicates that the calculation improves the correlation and accuracy of the models.

Table 5.3. Iteration history of R squared, data 1

Iteration Number	R squared		
	BI_{Q_new} model	BI_{R_new} model	BI_{Q_new} vs BI_{R_new}
0.0			0.7468
1.0	0.975	0.975	0.9859
2.0	0.857	0.966	0.9877
3.0	0.876	0.971	0.989
4.0	0.893	0.975	0.9901
5.0	0.907	0.978	0.9911
6.0	0.919	0.981	0.9919
7.0	0.929	0.983	0.9926
8.0	0.993	0.993	0.993
9.0	0.993	0.993	0.9934
10.0	0.994	0.993	0.9936
11.0	0.994	0.994	0.9939
12.0	0.995	0.994	0.994

R squared = 1 – (Residual Sum of Squares) / (Corrected Sum of Squares)

5.2.3 Real models

The BI models are calculated using field data and are labelled as real models. In Figure 5.5, BI_R increases with an increase in BI_Q. The correlation coefficient is low (about 0.3384). It may be due to several reasons. First, BI_Q and BI_R come from different definitions of brittleness. Even though the mineral composition (including quartz, calcite, dolomite and clay) and rock mechanics parameters (including Young's modulus and Poisson's ratio) are correlated with each other, BI_Q and BI_R may be affected by other factors causing a poor correlation. Second, brittle minerals like quartz, calcite and dolomite do not play the same role in BI calculation. Usually, quartz has a greater influence on E and v than calcite as identified earlier in this study. A third reason for a low correlation coefficient may be due to an experimental error.

The models are advanced by considering the weight of each brittle mineral and the rock mechanics parameters. Data 2 is used to get the weight coefficients *a*, *b*, *c*, k and n by implementing the same method described above.

Data 2 has the same trends as data 1 from Tables 5.4 and 5.5. Brittle minerals play different roles in BI prediction. The result of data 2 shows quartz > dolomite > calcite > clay in improving BI. Young's modulus (with a weight coefficient 0.731) has a more impact than Poisson's ratio in BI prediction (Table 5.4). The R squared of the BI_{Q_new} model, BI_{R_new} model and BI_{Q_new} vs BI_{R_new} increases with each iteration. A noted difference is that an increase in calcite increases Young's modulus a lot and decreases Poisson's ratio in just a small amount from data 2 which has a faster convergence rate than data 1.

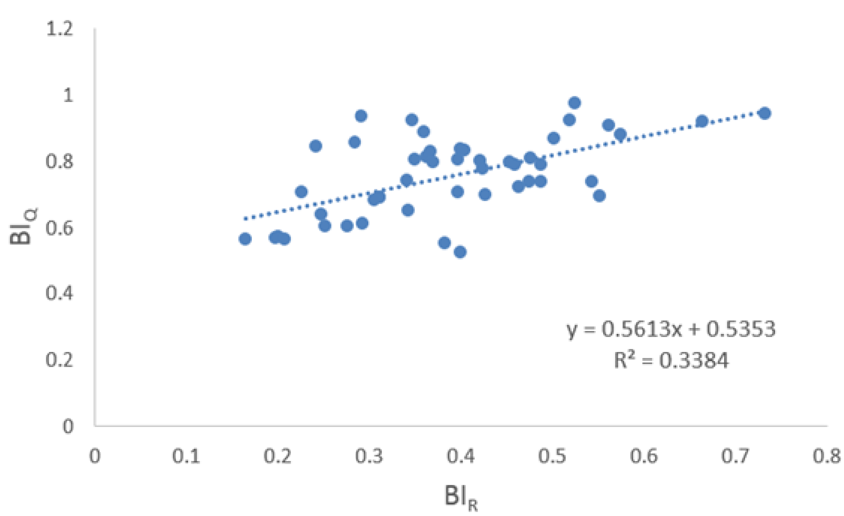

Figure 5.5 BI_Q vs BI_R

Table 5.4 Iteration history of weight coefficients, data 2

Iteration Number	a		b		c		n		k	
	Estimate	Std.Error	Estimate	Std.Error	Estimate	Std.Error	Estimate	Std.Error	Estimate	Std.Error
0.0	1		1				1		0.5	
1.0	0.667	0.133	0.527	0.132	0.253	0.626	-0.1	0.097	0.663	0.085
2.0	0.614	0.125	0.553	0.124	0.294	0.576	-0.063	0.092	0.712	0.081
3.0	0.598	0.125	0.561	0.124	0.306	0.573	-0.051	0.092	0.728	0.081
4.0	0.593	0.125	0.563	0.124	0.311	0.573	-0.048	0.092	0.731	0.081

Table 5.4 presents a reasonable standard of errors for the weight coefficients, except for coefficient c with a standard error of 0.573. This is because there are few samples that contain calcite. The calcite content in these samples is very low and not enough to calculate the weight coefficient of calcite accurately. The weight coefficient of calcite reflects the role of calcite in brittleness evaluation in Eq.5-3. Of course, reality is more complicated than this. The influence of pressure, diagenesis, temperature and rock texture is not considered. This is why the R squared of data 2 is much lower than that of data 1.

Table 5.5 Iteration history of R squared, data 2

Iteration Number	R squared		
	BI_{Q_new} model	BI_{R_new} model	BI_{Q_new} vs BI_{R_new}
0.0			0.338
1.0	0.396	0.391	0.401
2.0	0.414	0.404	0.421
3.0	0.415	0.405	0.422
4.0	0.415	0.405	0.422

R squared = 1 – (Residual Sum of Squares) / (Corrected Sum of Squares)

5.3 Case analysis and validation

In the analysis above, BI_{Q_new}, BI_{Jarvie}, and BI_{Wang} are calculated using data 3 (Table 5.1). The samples from Eagle Ford (Table 5.1) correspond to the ternary plots (from left to right) in Figure 5.6. The results are compared to the analysis of seismic mechanical facies (Figure 5.6). In Table 5.1, the models that consider quartz (or dolomite) as the only brittle mineral in Eagle Ford BI prediction are inaccurate because the BIs of the four samples are almost the same (Table 5.1). The results from seismic mechanical facies show that the samples from two wells on the arch are more brittle (Bodziak, 2014). This fact is shown by drilling cores. The BI calculated using the novel mineralogical model developed in this study matches with the results from seismic mechanical facies (Figure 5.6). The results of the weights of Young's modulus and Poisson's ratio in this thesis are based on statistics. The next chapter will consider the application of this new information in terms of impact on energy.

5.4 Conclusions

(1) Calcite improves BI by increasing Young's modulus and reduces BI by increasing Poisson's ratio at the same time. The increase of Young's modulus influenced by calcite is greater than that of the Poisson ratio. Calcite behaves as a brittle mineral and improves BI as a whole.

(2) Brittle minerals play a different role in BI prediction. Usually, quartz > dolomite > calcite > clay are the order for increasing rock brittleness.

(3) Young's modulus plays a more important role than Poisson's ratio in BI prediction, which is reasonable from the point of mineralogy.

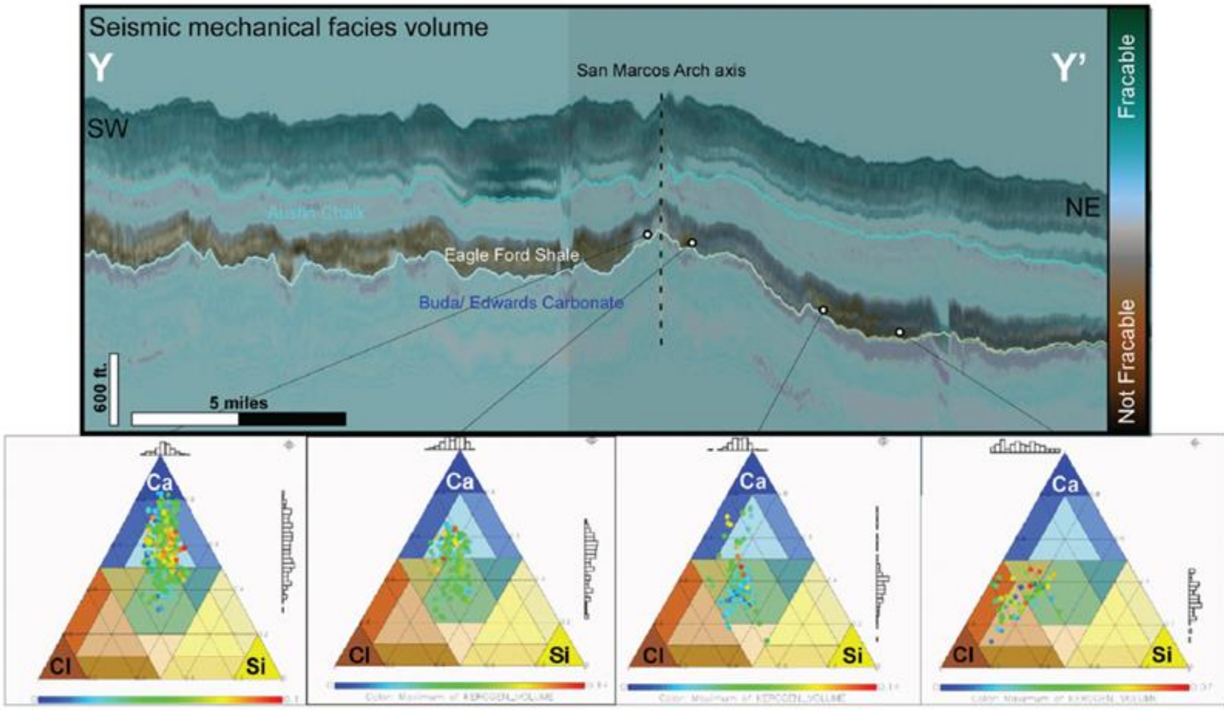

Figure 5.6 Seismic strike section across the San Marcos arch in Eagle Ford (Bodziak, 2014)
The lighter blue colors indicate the brittle facies (more carbonate-rich) and the darker brown colors indicate the more ductile (clay-rich) facies.

6. Experimental Methods Based on Energy

The next two chapters focus on the third limitation and the work is to establish a new method for brittleness evaluation based on energy analysis. The existing challenges that must be addressed are explored and details of the methods used to establish new models are provided. The new models are based on experimental data. In the next chapter, a new numerical method of brittleness evaluation based on energy is proposed. Part of this research has been published in AAPG annual convention 2016 with me as the first author (Hu, 2016).

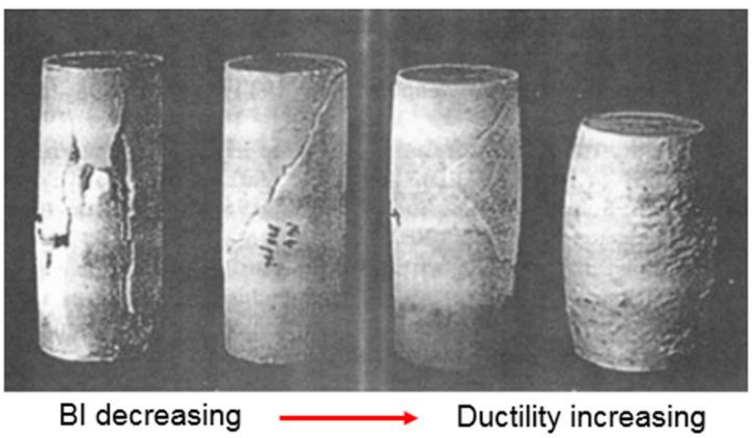

Figure 6.1 Traditional definition of rock brittleness

6.1 Existing Problems and Methodology

6.1.1 Existing problems

What is brittleness? Usually, the higher the magnitude of the BI, the more brittle the rock (Figure 6.1). Reality is more complicated than this. Consider the two cases (Figure 6.2). Case I: the rock needs more energy to achieve failure; however, there is a higher rock fragmentation degree after failure. Case II: the rock needs less energy to achieve failure; however, there is a lower rock fragmentation degree after the failure. Which rock is more brittle? Most of the time the focus on theoretical parameters like Young's modulus and Poisson's ratio in brittleness evaluation is too high. The real effect like the degree of rock fragmentation may be ignored. The relevant factor is not how large the rock mechanics parameters are. It is more important to understand to what extent rocks can be fractured during hydraulic fracturing so that more oil/gas moves through the fractures in a reservoir.

Old models of brittleness evaluation did not consider the influence of temperature, confining and pore pressure. No model considers all of the factors. The new analytical/semi-analytical models from this research consider the influence of temperature, confining and pore pressure, respectively. However, those models cannot work when temperature, confining and pore pressure change together. Also, degree of rock fragmentation cannot be measured by using the analytical/semi-analytical models. It is necessary to find a method of brittleness evaluation that can be used to reliably describe rock brittleness and characterize rock fracability.

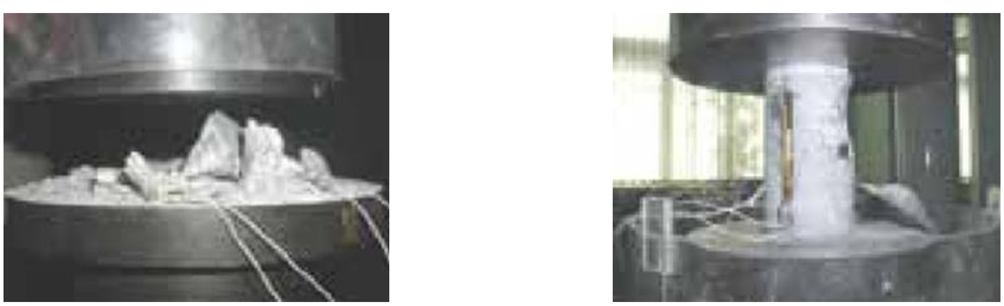

Case I Case II

Figure 6.2 Two cases of rock failure.

*Case I: broken to pieces, with energy density 0.58mJ*mm-3. Case II: cleavage, with energy density 0.18mJ*mm-3.*

Based on the above analysis, when confining pressure increases the ultimate strength and plastic deformation increase too (Figure 4.2), the energy used to create rock failure increases. When pore pressure increases, the ultimate strength will decrease and energy consumption decreases (Figures 4.8 and 4.9). An increase in temperature increases the rock plastic deformation (Figure 5.1) and decreases the ultimate strength by increasing pore pressure (Figures 4.8 and 4.9). The reaction is described by energy conversion. Table 6.1 provides the relationships between confining pressure, pore pressure, temperature and energy consumption.

Since all parameters above can be described by energy, why not use energy to directly characterize rock brittleness and fracability?

Table 6.1 Relationships between energy and other parameters

Factors	Ultimate strength	Plastic deformation	Energy consumption
P_c +	+	+	++
P_p +	-		-
T + (0,200°C)	-	+	+?

-: decrease *+: increase* *++: increase rapidly*

6.1.2 Methodology

This chapter is focused on the energy analysis of rock failure based on experimental data. Experiments on cyclic loading-unloading tests are used to analyze the relationship between rock brittleness and energy. There are many types of energy during rock failure: elastic energy, plastic energy, thermal energy, kinetic energy, and frictional energy. The energy that can be used to characterize rock brittleness and how to calculate this energy are the first step.

Rock failure is a process of energy dissipation and release. The energy dissipation leads to plastic deformation and damage of rock. The releasable strain energy results in an abrupt structural failure of the rock (Figure 6.3).

$$U_i = U_{\mathrm{i}}^{\mathrm{d}} + U_{\mathrm{i}}^{e} \tag{6-1}$$

where U_i^d is the dissipation energy and U_i^e is the release energy.

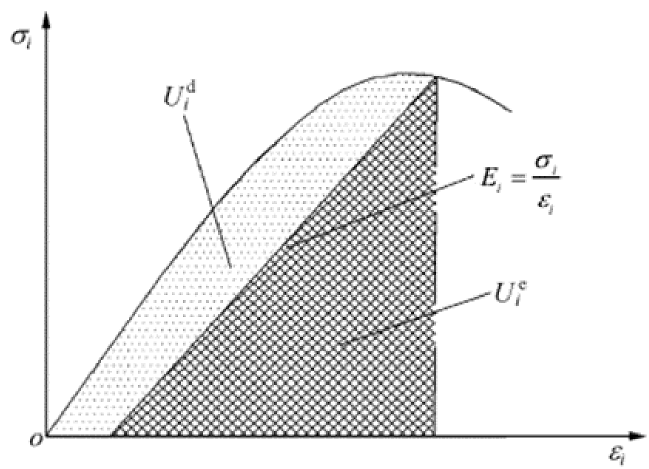

Figure 6.3 Relationship between dissipated energy and releasable strain energy of rock mass element (Xie, 2005)

Energy into the rock system will transfer into elastic energy, plastic energy and damage energy (Figure 6.4). Elastic energy (releasable strain energy) is accumulated in the rock and is released or transferred into another type of energy. Plastic energy and damage energy are dissipated for plastic deformation and damage making microcracks that are irreversible. The damage energy describes the energy used to create crack/fracture surfaces. This quantifies the disruption of intermolecular bonds that occur when a surface or fracture is created. In the deformation of solids, damage energy is treated as the "energy required to create one unit of surface area” and is a function of the difference between the total energies of the system before and after the deformation (Woodruff, 2002). By calculating the dissipation energy and elastic energy it is possible to predict how much energy is used to fracture the rock.

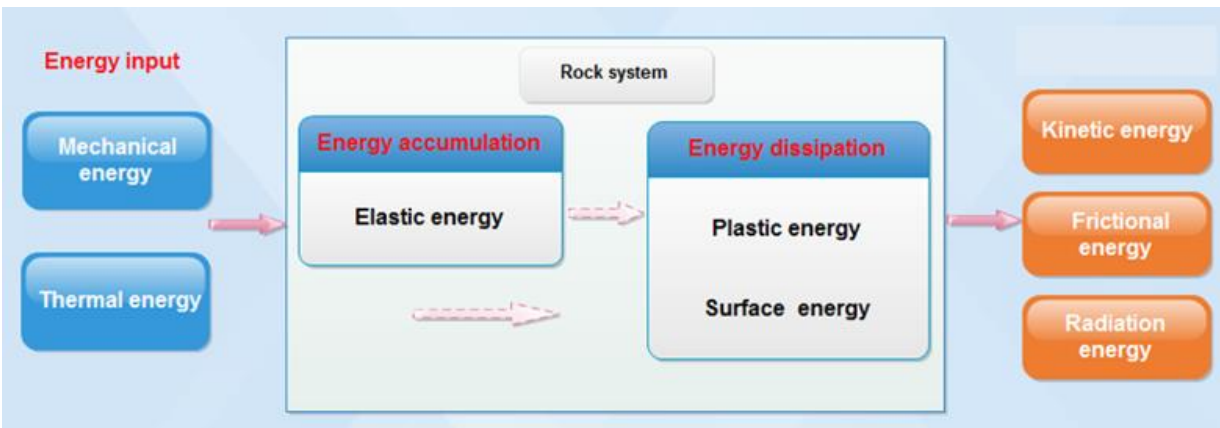

Figure 6.4 Sketch map of energy conversion during rock failure

Cyclic loading-unloading tests by using MTS815 electro hydraulic servo system (Figure 6.5) are used to investigate the effect of energy dissipation and release during rock failure. The load step is 20kPa per cycle. Load from 0 to 20kPa and unload, and then reload from 0 to 40kPa, … , until the sample failure. The rate of loading is 1kPa/s. Sandstone samples are from Nanyi quarry in Xuzhou (Zhang, 2013) and shale samples are from Longmaxi shale in Sichuan, China. The samples are made by using ISO size of rock testing with 5cm in diameter and 10cm in height.

Loading and unloading stress-strain curves are used to calculate the dissipation energy and elastic energy, since releasable strain energy is reversible. The energy released from unloading is equal to the elastic energy accumulated from the previous loading.

Figure 6.5 MTS815 electro hydraulic servo system

If unloading is at point A (Figure 6.6) in a uniaxial compression test, the strain-strain curve returns and meets at point C with the x-axis. If the thermal influence is ignored, then the area AOB represents the input energy U_i. The area ACB represents the releasable strain energy U_{ie}. The area AOC represents the dissipation energy U_{id} that is dissipated to make plastic deformation or create microcracks inside the rock. The loads are applied slowly, the crack velocity is assumed to be small, and the kinetic energy of the body is negligible. The test is completed using constant temperature and thermal energy is ignored. The dissipation energy is the difference between total energy and elastic energy.

$$U_{\mathrm{i}}^{\mathrm{d}} = \int_0^{\varepsilon'} \sigma_i d\varepsilon_i - \int_{\varepsilon''}^{\varepsilon'} \sigma_i d\varepsilon_i \tag{6-2}$$

$$U_{\mathrm{i}}^{e} = \int_{\varepsilon''}^{\varepsilon'} \sigma_i d\varepsilon_i \tag{6-3}$$

where U_i^d is the dissipation energy, U_i^e is the release energy, σ_i is the stress in i direction and ε_i is the strain in i direction.

By defining rock brittleness in terms of energy, rocks from different areas can be compared. The influencing factors ignored in other models of brittleness evaluation (confining pressure, temperature and rock texture) are addressed. The degree of rock fragmentation is described by dissipation energy.

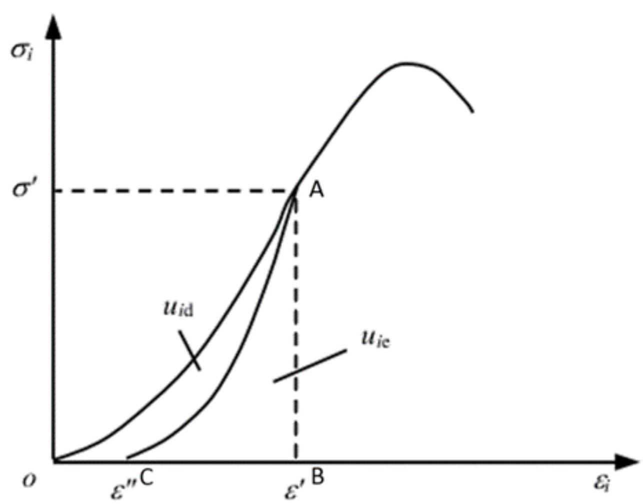

Figure 6.6 Loading-unloading stress-strain curve of rock mass element

6.2 Results and Discussion

6.2.1 Experimental results and analysis

The results indicate that dissipation energy of a sandstone sample remains low before failure and increases sharply when failure occurs (Figure 6.7). In the shale sample, there is less difference in energy dissipation before and during the failure (Figure 6.8), because more energy is converted into plastic energy instead of damage energy.

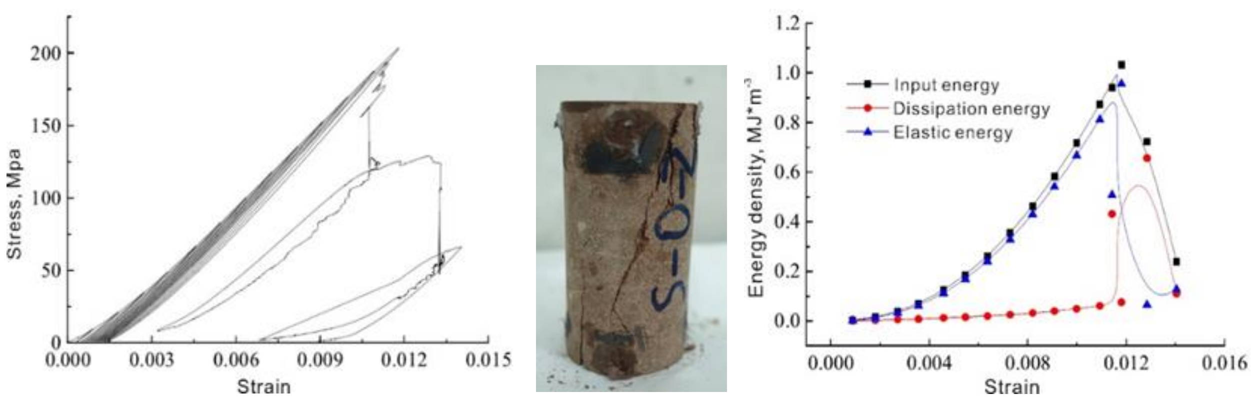

a. Loading and unloading stress-strain curves b. Energy evolution curves

Figure 6.7 Loading and unloading stress-strain curves and energy curves of sandstone (Zhang, 2013)

Compared to the shale sample, the sandstone sample has more elastic energy released during rock failure and converted into dissipated energy than the shale sample (Figures 6.9 and 6.10, Table 6.2). This means more energy is consumed as damage energy making the cracks or plastic energy to create plastic deformation. Assuming that the plastic energy is the same for both the sandstone and the shale rock, the energy used to fracture the sandstone is greater than the energy consumed to fracture the shale. This analysis aligns with the results from the sandstone sample; it has more cracks after rock failure than the shale sample (Figures 6.7 and 6.8).

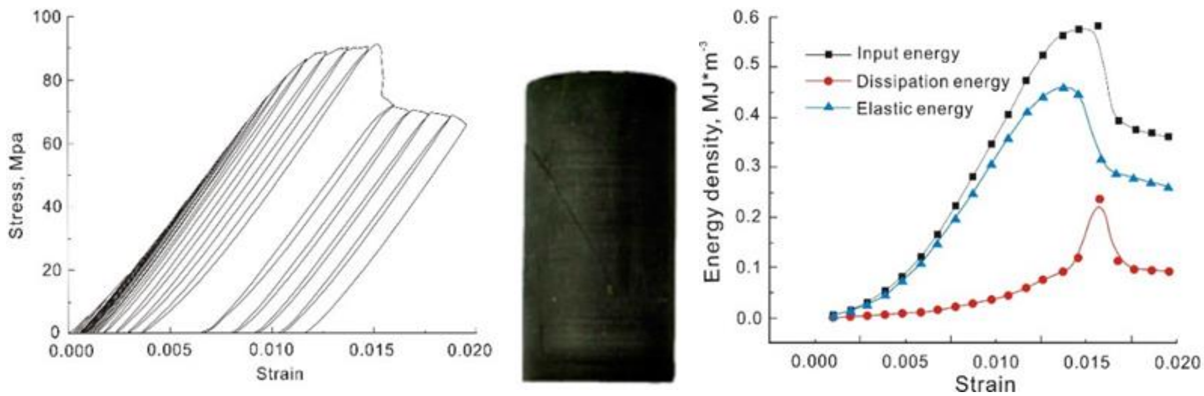

a. Loading and unloading stress-strain curves b. Energy evolution curves

Figure 6.8 Stress-strain curves and energy evolution curves of shale

Chapter 4 identified a contradiction: from the change of Young's modulus and the results of the uniaxial compression tests (Figure 6.5), the brittleness of the shale samples seemed to increase with temperature. In terms of axial-failure strain and total deformation, plasticity of shale samples increase with temperature (Figure 6.3). It may be explained in terms of energy. More energy is needed for failure of shale rock at high temperature than at low temperature because more energy is consumed in plastic deformation. This is why stress-strain curves show the total deformation of shale samples increasing with temperature. The energy input is composed of mechanical energy and thermal energy as shown in Figure 6.4. It is the thermal energy provided by the external environment that creates extra microcracks and plastic deformation. This part of energy should not be considered mechanical energy as the energy used to fracture the rocks does not change. This may explain why both rock fragmentation degree and plastic deformation of shale samples increase with an increase in temperature.

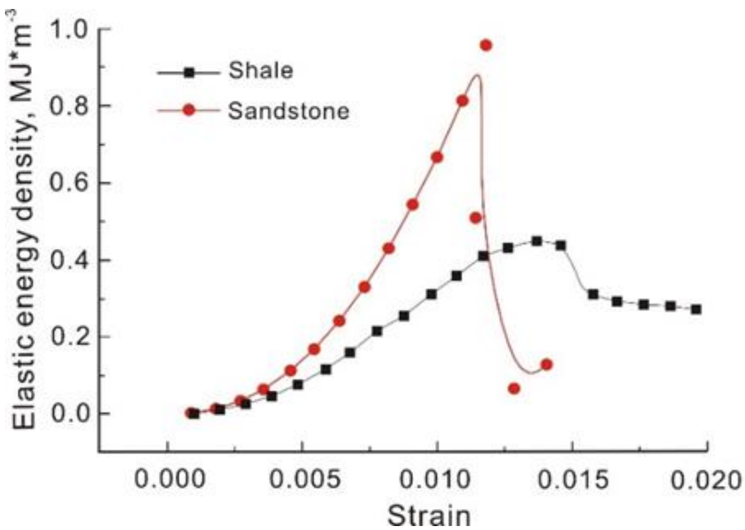

Figure 6.9 Variation of elastic energy density

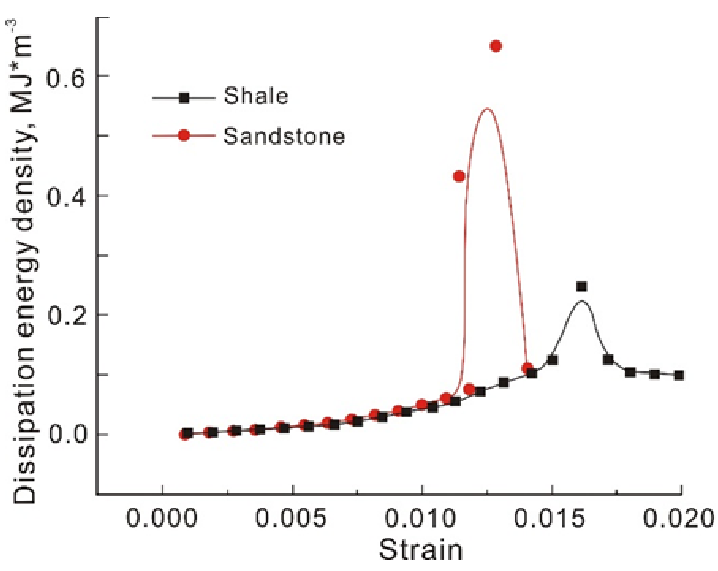

Figure 6.10 Variation of dissipation energy density

Table 6.2 Energy density during rock failure (MJ-millijoule)

Lithology	Maximum elastic energy density (MJ*mm^{-3})	Elastic energy density after failure (MJ*m^{-3})	Maximum dissipation energy density (MJ*m^{-3})
Sandstone	0.956	0.122	0.649
Shale	0.449	0.281	0.247

6.2.2 Analytical Analysis

For brittle rock samples, we ignore the energy consumption of plastic deformation. Then, we simplify the model by assuming that the rock will break into N balls of the same size.

$$u^{\mathrm{d}} = (4N\pi r^2 - 2\pi R\mathrm{h} - 2\pi R^2)\gamma \tag{6-4}$$

Here R is the radius of the sample, h is the height of the column, r is the equivalent radius of the rock fragments and γ is the surface free energy. According to volume conservation

$$\frac{4}{3}\mathrm{N}\pi r^3 = \pi R^2 h \tag{6-5}$$

the relationship between the equivalent degree of rock fragmentation and dissipation energy is

$$N = \frac{(\frac{u^d}{\gamma} + 2\pi Rh + 2\pi R^2)^3}{36\pi^3 R^4 h^2} \tag{6-6}$$

For brittle rocks, the greater the energy dissipation during the process, the smaller the fragments after rock failure. For plastic rocks, the energy consumption of plastic deformation should be considered.

6.3 Conclusions

(1) Energy dissipation determines the degree of rock fragmentation. The greater the energy dissipation during the process, the more cracks or fragments after rock failure.

(2) The energy dissipation of brittle rock remains low prior to failure and increases sharply when the failure occurs. For ductile rock, there is less difference in energy dissipation before and during the failure. This is because more energy is converted into plastic energy instead of energy to increase the degree of rock fragmentation.

(3) Energy dissipation at high temperature is greater than the dissipation at a relatively low temperature. The thermal energy from heating provides the extra energy necessary to make cracks.

(4) By comparing the value of energy dissipation and release it is possible to evaluate rock brittleness and predict the degree of rock fragmentation after rock failure.

7. Numerical Methods Based on Energy

7.1 Existing Problems and Methodology

Based on the experiment analysis described previously, a method to evaluate rock brittleness in terms of energy is explored in Chapter 6. The method is effective only when rock ductility is ignored. Also, a cyclic loading-unloading test is needed to make the method practical for industrial applications.

In the following sections a numerical method to evaluate rock brittleness in terms of energy is developed. The method is used to evaluate rock brittleness in complicated conditions by considering hydro-mechanical (HM) interactions. The model attempts to remove the main limitations of idealized elastic or kinematic methods that do not account for the complexity of rock deformation. Data from rock mechanics tests and finite element (FE) modelling are used in this research to generate realistic simulations that consider the influence of plastic deformation and damage dissipation energy on brittleness and fracability evaluation.

7.1.1 Existing problems

Three problems need to be solved to establish the numerical models: a nonlinear solution, crack initialization and propagation and limitations of existing software.

7.1.1.1 Nonlinear solution

There are three sources of nonlinearity in structural mechanic simulations: material nonlinearity, boundary nonlinearity and geometric nonlinearity. Material nonlinearity is the most familiar and is the focus in this section. Most materials have a fairly linear stress/strain relationship at low strain values. They tend to yield and become nonlinear at higher strains which are irreversible

(Figure 7.1). Material nonlinearity may be related to factors other than strain. Strain-rate-dependent material data and material failure are both forms of material nonlinearity. Material properties are also a function of temperature and other predefined fields.

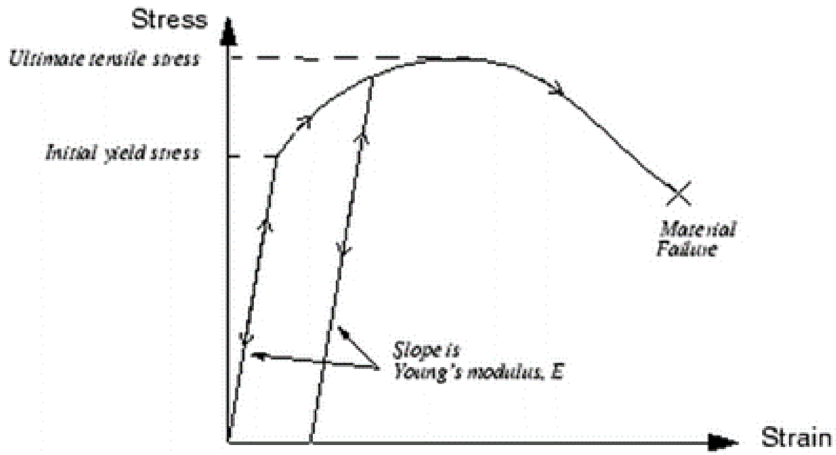

Figure 7.1 Stress-strain curve for an elastic-plastic material under uniaxial tension

The fully elastic material property has a linear stress-strain relationship regardless of the load applied. But it is not enough to describe rock failure, especially when rock plasticity is considered. The elastic-plastic material property has a linear relationship up to the yield point and becomes nonlinear beyond the yield point (Szwaja, 2012). To calculate the energy of plastic deformation, a nonlinear stress-strain relationship needs to be considered.

7.1.1.2 Crack initialization and propagation

To simulate discontinuities like a crack by using the conventional finite element method (FEM), the grids need to be changed to reflect the geometric discontinuities. A large number of grids are needed around the crack tip area to fully capture the singular asymptotic fields (Moes, 1999).

The modelling of dynamic discontinuities using the conventional FEM is difficult and cumbersome because the grids need to be continually updated to match the geometry when a crack initializes and propagates.

Several new finite element techniques have been developed to model cracks and crack growth without remeshing. These include the incorporation of a discontinuous mode on an element level (Oliver, 1995), a moving mesh technique (Rashid, 1998) and an enrichment technique for finite elements based on a partition-of-unity that involves minimal remeshing (Belytschko, 1999). In Belytschko and Black (1999), curved cracks are treated by mapping the straight crack enriched field. This is not readily applicable to long cracks or three dimensions (Moes, 1999).

7.1.1.3 Limitation of existing software

There are many software packages that use the FEM to solve partial differential equations, like Abaqus, Ansys, Nastran, and Cosmos. Each has its own advantages. For example, Abaqus is good at nonlinear analysis, modelling and post processing and Ansys is adept at linear solutions. The software chosen is dependent on user requirements. Most of the software packages provide an environment named CAE for the user with a simple and consistent interface to build and process models and evaluate results. CAE does not work in many complex situations. Elements and nodes out of sight cannot be defined and complex simulations like pore fluid diffusion or coupling are not possible. A secondary development and user subroutines are often applied providing users an opportunity to realize their particular analysis requirements.

7.1.2 Methodology

The analysis starts with an elastic-plastic damage rheology including pressure-dependent yield criteria, plastic deformation and fracturing via a continuum damage approach. The results of triaxial compression tests are used to refine and calibrate the rheology. FE damage models based on the continuum damage theory have been built. The plastic energy and damage dissipation energy are calculated from these models. An extended finite element method (XFEM) and cohesive behaviour are used in crack initialization and growth so that realistic failure of rocks is predicted. This numerical method is applied to evaluate rock brittleness in more complicated conditions by considering the influence of confining pressure and pore fluid in coupled HM models.

7.1.2.1 Finite element method

The finite element method (FEM) is the dominant discretization technique in structural mechanics. The basic concept in the physical interpretation of FEM is the subdivision of the mathematical model into disjointed components of simple geometry called finite elements or elements for short. The response of each element is expressed in terms of a finite number of degrees of freedom characterized as the value of an unknown function, or functions, at a set of nodal points. The response of the mathematical model is approximated using the discrete model obtained by connecting or assembling the collection of all the elements (Chen, 2005). This subdivision method helps to accurately represent a complex geometry and includes dissimilar material properties.

The FEM is chosen because it is based on displacement and the energy of nodes in solid mechanics. The energy values are easier to obtain. The finite element analysis obtains the temperatures, stresses, flows, and/or other desired unknown parameters by minimizing an energy functional in the finite element model. An energy functional includes all the energy associated with the particular finite element model. A series of information on stress, strain, displacement, and energy is obtained from the finite element solution (Dassault Systèmes, 2016).

7.1.2.2 Extended finite element method

The extended finite element method (XFEM) (Moes, 1999) is an extension of the conventional finite element method based on the concept of partition of unity (Babuska, 1997). The presence of discontinuities in an element is allowed by enriching the degrees of freedom with special displacement functions (Figure 7.2).

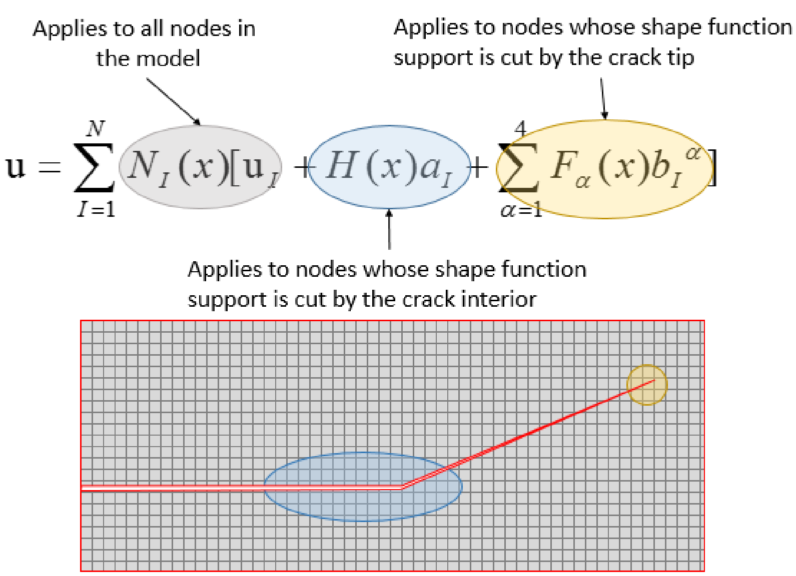

Figure 7.2 The effect of each function (Du, 2010)

NI(x): shape functions, H(x): jump function, Fα: asymptotic crack-tip functions.

The key issues are the selection of the appropriate nodes to enrich and the form of the associated enrichment functions. In terms of enrichment with a jump function, the convention adopted is that a node is enriched if the support is cut by a crack into two disjoint pieces. Figure 7.3 illustrates the application of this rule when the crack is not aligned with the element edges, and the circled nodes are enriched with the jump function (Moes, 1999).

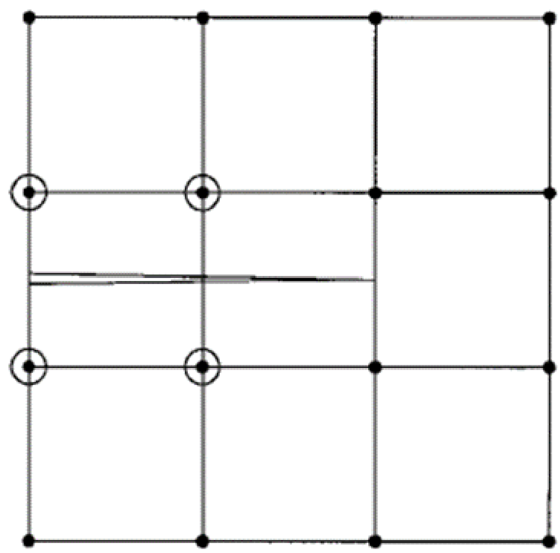

Figure 7.3 Crack not aligned with a mesh (Moes, 1999)

In a more general case such as that shown in Figure 7.4, the crack tip will not coincide with an element edge, and in this instance the discontinuity cannot be adequately described using only a function such as H(x). The jump enrichment of the circled nodes in this case only provides for the modelling of the discontinuity up until point p. To seamlessly model the entire discontinuity along the crack, the squared nodes are enriched with the asymptotic crack tip functions with the technique developed by Belytschko and Black (Belytschko, 1999).

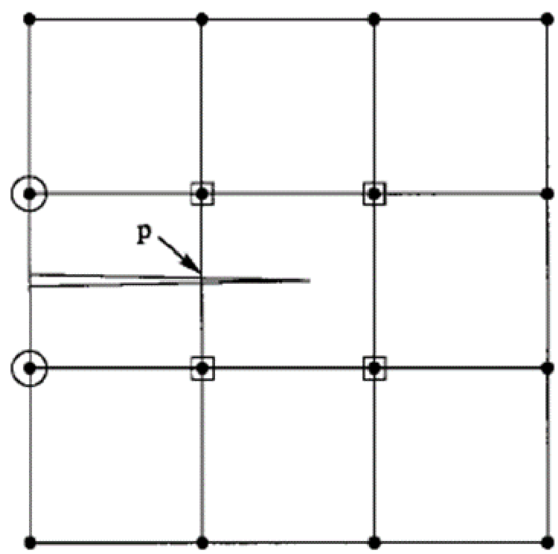

Figure 7.4 Crack tip not coincided with a mesh (Moes, 1999)

7.1.2.3 Introduction of Abaqus

The FE software Abaqus has been used in our research which is good at nonlinear solution, post processing and providing plentiful user subroutines. Abaqus is widely used in materials mechanics. The software is popular with academic and research institutions due to the wide material modelling capability and the program's ability to be customized. Abaqus was initially designed to simulate nonlinear physical behaviour and has an extensive range of material models.

Abaqus/Standard can evaluate several parameters for fracture mechanic studies based on the conventional finite element method or the extended finite element method. Abaqus has a number of multiphysics capabilities: coupled pore fluid diffusion and stress analysis, and coupled thermal-stress analysis making it powerful for simulations where multiple fields need to be coupled (Du, 2010). It provides a plenty of user-defined subroutines and allows users to define their own models when there is not an appropriate model in the data base.

7.1.2.4 User subroutines

Numerous user subroutines help users to realize their particular analysis requirements by adapting Abaqus. DLOAD supports defining nonuniform-distributed mechanical loads (pressures and body forces), UPOREP helps users define the initial pore fluid pressures in a coupled pore fluid diffusion and stress analysis as a function of node location (Du, 2010). In this section the real process of hydraulic fracturing is simulated, including formation stress, pore pressure, fluid injection, void ratios and formation leakage. User subroutines of DISP, DLOAD, SIGINI, UPOREP, VOIDRI and UFLUIDLEAKOFF have been used to make a script file to adapt Abaqus. The details of those user subroutines are described in Appendix B.

7.2 Simulation of Axial Compression Test

7.2.1 Model description and setup

7.2.1.1 Model description

Three-dimensional (3D) FE models are created using laboratory tests. The material of the model is defined by using the property of the shale sample from the experiment. C3D8R is used in the models to simulate axial compression. It is an 8-node linear brick in geometric order considering reduced integration. Abaqus/Explicit is chosen to simulate 3D stress. It is particularly used to simulate brief transient dynamic events and severely nonlinear behavior such as contact (Dassault Systèmes, 2016). The samples are made by using ISO size of rock testing with 5cm in diameter and 10cm in height.

Secondary development with Python is used to define the heterogeneity of the rock model to accurately describe the properties of the real rock sample. 4 types of material properties based on the shale sample in chapter 6 have been created and allocated to different elements (Figure 7.5b).

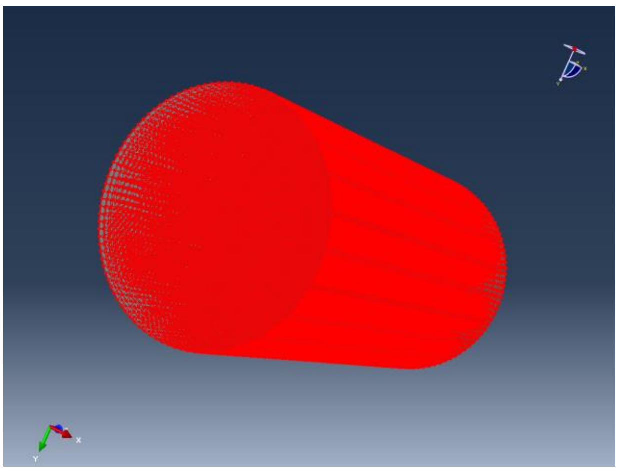

a. Mesh

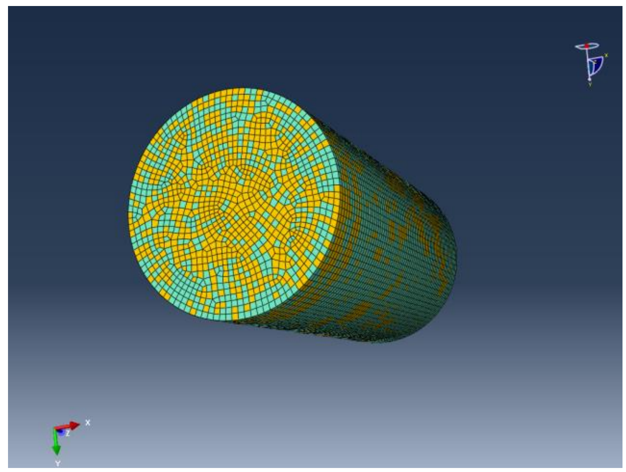

b. Property assignment

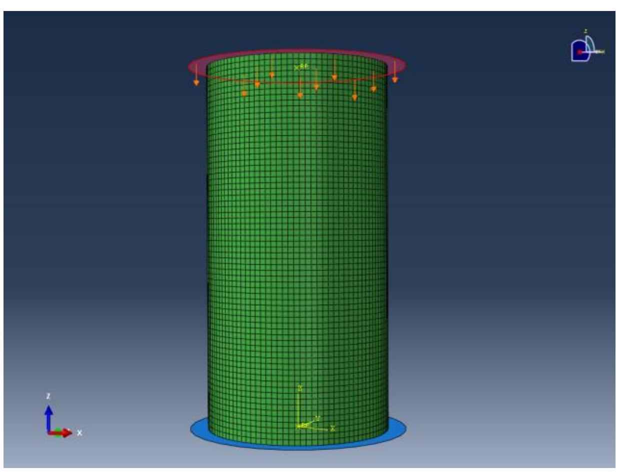

c. Stress loading

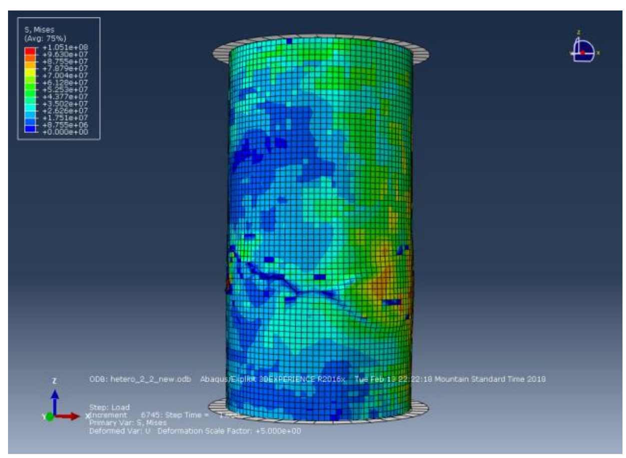

d. Model after failure (5x)

Figure 7.5 FE Models of the Uniaxial Compression Test

Elements have different physical properties and rock mechanics properties where required. The bottom of the sample is fixed and the stress is added from the top of the sample (Figure 7.5c) until it gets failure, which is the same as the axial compression test. The loading rate is 1kPa/s.

Finally, the experimental results of the uniaxial compression test are applied to refine and calibrate the models.

7.2.1.2 Definition of damage mechanism

Material failure (like rock failure) refers to the complete loss of load carrying capacity that results from progressive degradation of the material stiffness. Stiffness degradation is modeled using damage mechanics (Zhong, 2010). There is a general framework for modelling the damage and failure of conventional materials in Abaqus. One or more damage mechanisms can be combined to function simultaneously in the framework. Each damage mechanism should consist of two ingredients: a damage initiation criterion (path O to A in Figure 7.6) and a damage evolution (path A to B in Figure 7.6) creating a completely damaged state.

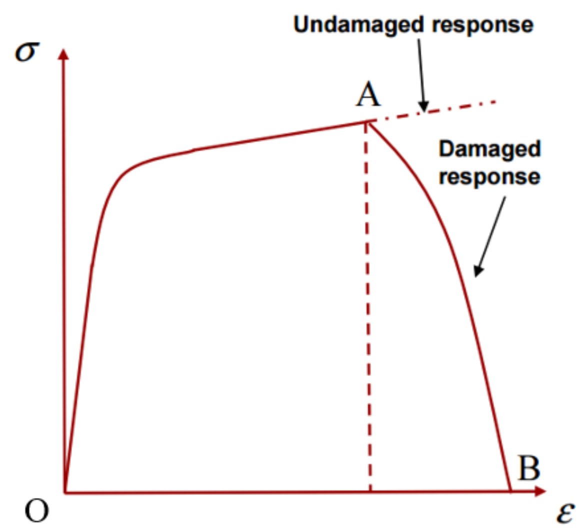

Figure 7.6 Stress-strain curve of material failure

(1) Damage initiation (path O to A)

Damage initiation determines the initiation point of stiffness degradation based on all kinds of user-specified criteria: maximum principal stress (MAXPS) criterion, maximum principal strain criterion (MAXPSC), maximum strain energy release rate criterion (MAXSERC), and maximum shear stress criterion (MSSC). MAXPS damage and shear damage are used as the primary fracture criteria in this model.

The MAXPS theory is applicable for brittle materials. Failure occurs when maximum principal stress in an object exceeds uniaxial ultimate tensile/compressive strength (or yield strength) of the material (Figure 7.7).

$$f = \max(|\sigma_1|, |\sigma_2|, |\sigma_3|) = Y \tag{7-1}$$

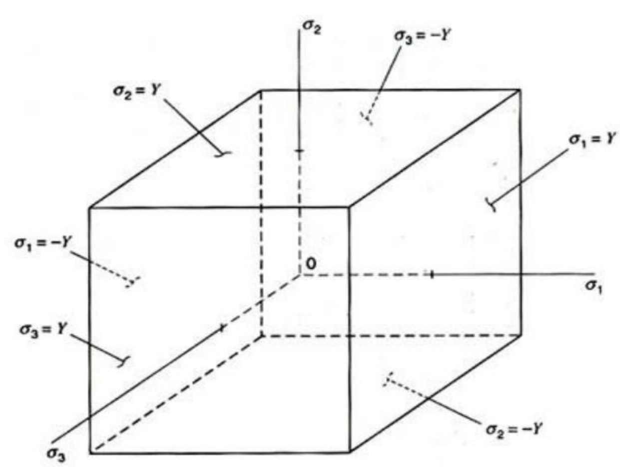

Figure 7.7 Maximum principal stress yield surface (Szwaja, 2012)

Shear criterion is appropriate for triggering damage due to shear band localization. It assumes that the equivalent plastic strain at the beginning of damage is a function of the shear stress ratio and strain rate (Dassault Systèmes, 2016). The shear stress ratio is defined as

$$\theta_s = (q + k_s p) / \tau_{\max} \tag{7-2}$$

In Abaqus, the shear criterion is used with the Mises, Johnson-Cook, Hill and Drucker-Prager plasticity models, including an equation of state (EOS). It is noteworthy that damage and failure do not occur unless damage evolution is defined (Figure 7.8c).

(2) Damage evolution (path A to B)

Damage evolution determines the material behaviour after damage initiation. It describes the degradation rate of the material stiffness when the initiation criterion is satisfied. The formulation is based on a scalar damage approach (Dassault Systèmes, 2016)

$$\sigma = (1 - D)\bar{\sigma} \tag{7-3}$$

The overall damage variable D reflects the combined influence of all the damage mechanisms. When D = 1, material at that point has completely failed.

For an elastic-plastic material, damage evolution is reflected in two ways: (1) softening the yield stress and (2) degradation of the elasticity (Figure 7.9) (Dassault Systèmes, 2016). After considering damage evolution, the response of the simulation (Figure 7.9d) provides a good approximation of the real physical response (Figure 7.9b).

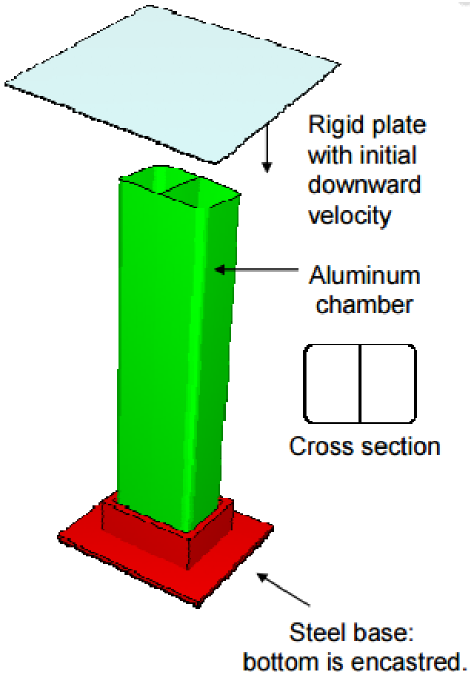

a. Schematic diagram

b. Result from the experiment

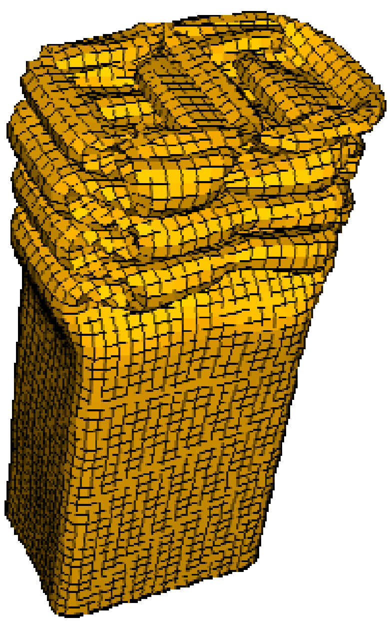

c. Simulation only with damage initiation

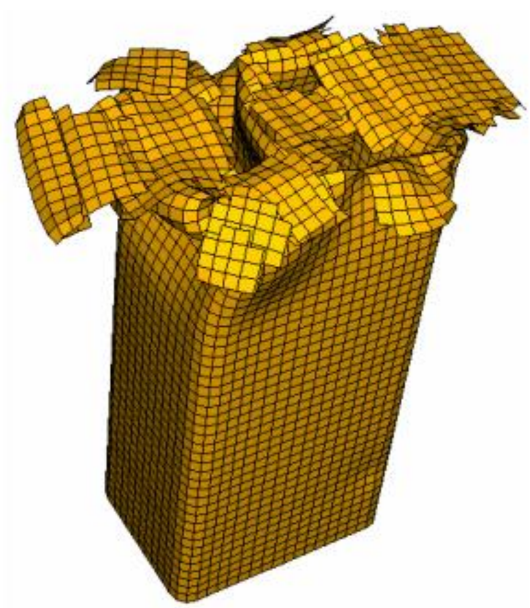

d. Simulation with damage evolution

Figure 7.8 Analysis of damage criteria for metals

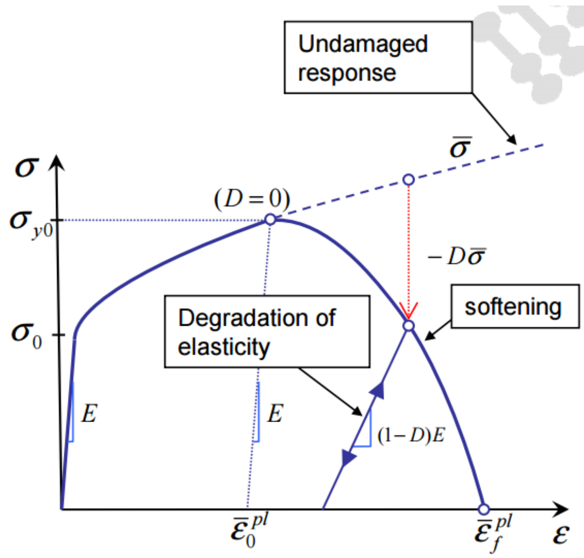

Figure 7.9 Stress-strain curve of an elastic-plastic material failure (Dassault Systèmes, 2016)

7.2.1.3 Energy setup

In Abaqus, the energy balance equations for the entire model are written as (Dassault Systèmes, 2016)

$$E_W + E_{HF} = E_{IE} + E_{KE} + E_{FD} + E_V + E_{IHE} - \text{Other} \tag{7-4}$$

$$E_{IE} = E_E + E_P + E_{CD} + E_A + E_{DMD} + E_{DC} + E_{FC} \tag{7-5}$$

Based on the real uniaxial compression test, the simulation is set up to load slowly at a constant temperature condition without considering the influence of fluid. Eq. 7-4 and Eq. 7-5 are simplified as

$$E_W \text{-} \mathrm{E}_{\mathrm{KE}} \text{-} \mathrm{E}_{\mathrm{FD}} = E_{IE} = E_E + E_P + E_{DMD} \tag{7-6}$$

7.2.2 3D homogeneous model

Based on the analysis above, a homogeneous model of the uniaxial compression test is established first. The model is 0.1m in height and 0.025m in radius with Young's modulus 10Gpa and Poisson's ratio 0.33. A smoothed particle hydrodynamics (SPH) method is used in this homogeneous model to disperse a prescribed set of continuums into small particles. Figure 7.10 is the result of the homogeneous model and it matches well with the corresponding rock failure moment during the uniaxial compression test (Figure 7.11). The debris of the rock sample during the rock failure (Figure 7.10) is evident.

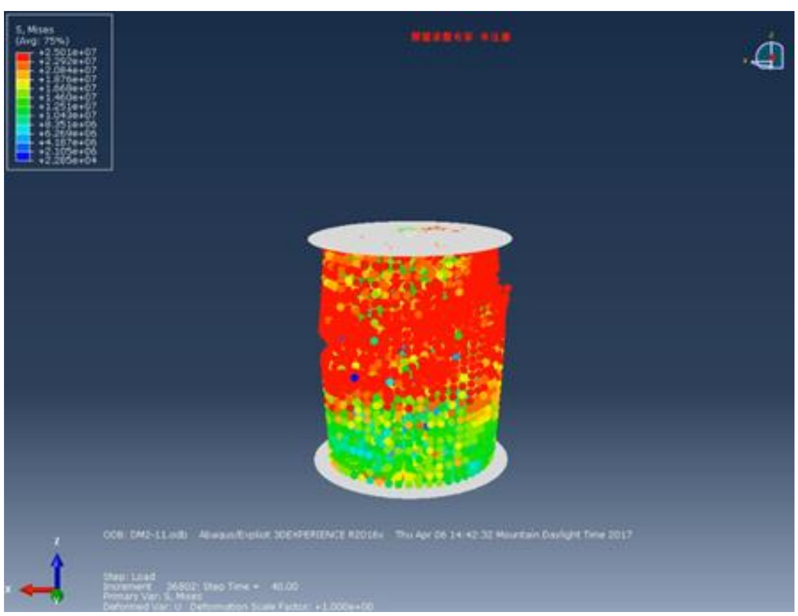

Figure 7.10 Homogeneous model of the uniaxial compression test

Figure 7.11 Rock failure moment of uniaxial compression test

Figure 7.12 shows the energy analysis of the homogeneous model. At first elastic energy, plastic energy and damage energy increase slowly with the increase of load before the rock failure. During rock failure, damage energy increases rapidly compared to a fast decrease of elastic energy. The plastic energy is much greater than the elastic energy and damage energy. It is more difficult for a homogeneous model to fail than a heterogeneous model of the same property. More energy is used to deform the homogeneous model before failure.

The mesh of the model is dispersed by using the SPH method to simulate emulational debris to some extent. The material properties of those discrete particles could not be defined separately. Heterogeneous models also could not be established. In the next section, a heterogeneous model of the uniaxial compression test is built and validated with previous experimental results.

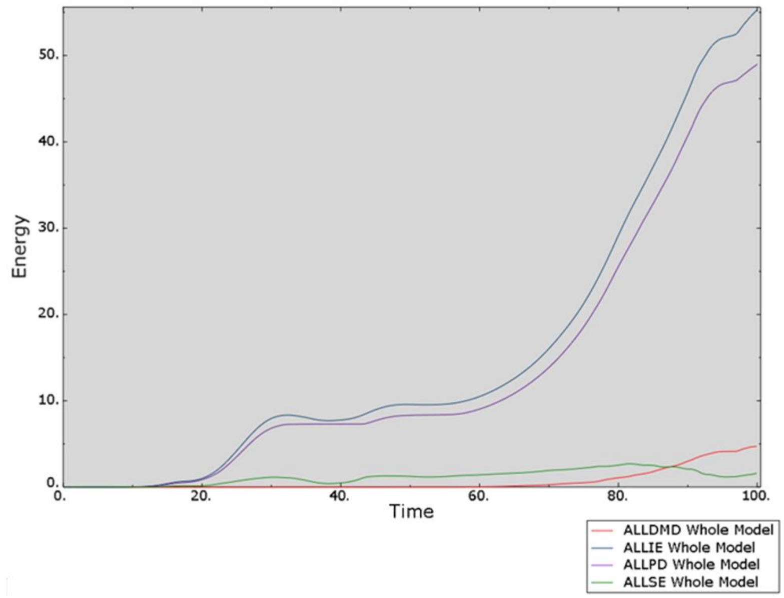

Figure 7.12 Energy analysis of the homogeneous model

(unit of energy J, unit of time sec)

7.2.3 3D heterogeneous model and validation

These methods are used to build a heterogeneous model based on the properties established for the shale from Chapter 6. The model is 0.1m in height and 0.025m in radius. Figures 7.13 and 7.14 are the heterogeneous model of the uniaxial compression test and the corresponding energy analysis.

From Figure 7.14 elastic energy, plastic energy and damage energy increase slowly at the beginning with the increase of load. During rock failure, damage energy increases rapidly compared to the fast decrease of elastic energy. This matches well with the experimental result from the loading-unloading test conducted in Chapter 6. The shape of the model is similar to the shale sample after the loading and unloading test in Chapter 6.

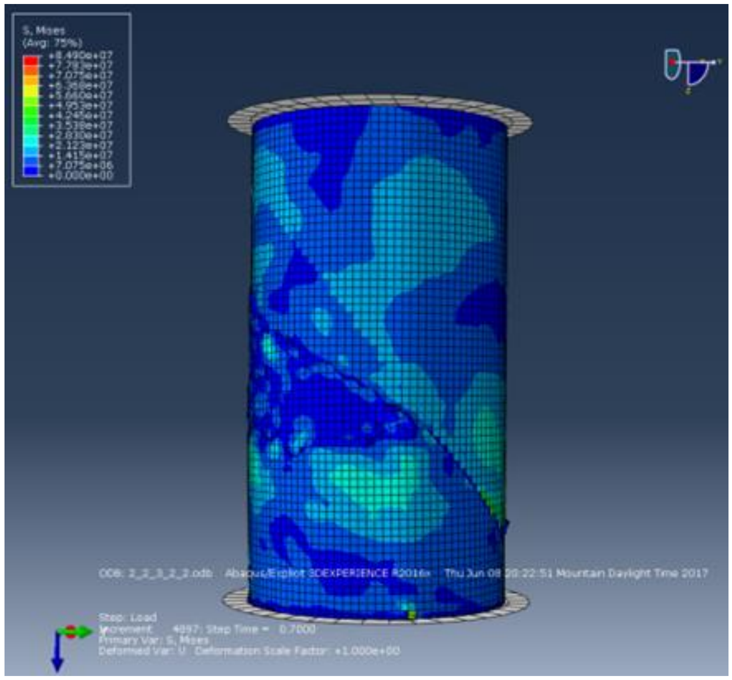

Figure 7.13 Heterogeneous model of uniaxial compression test

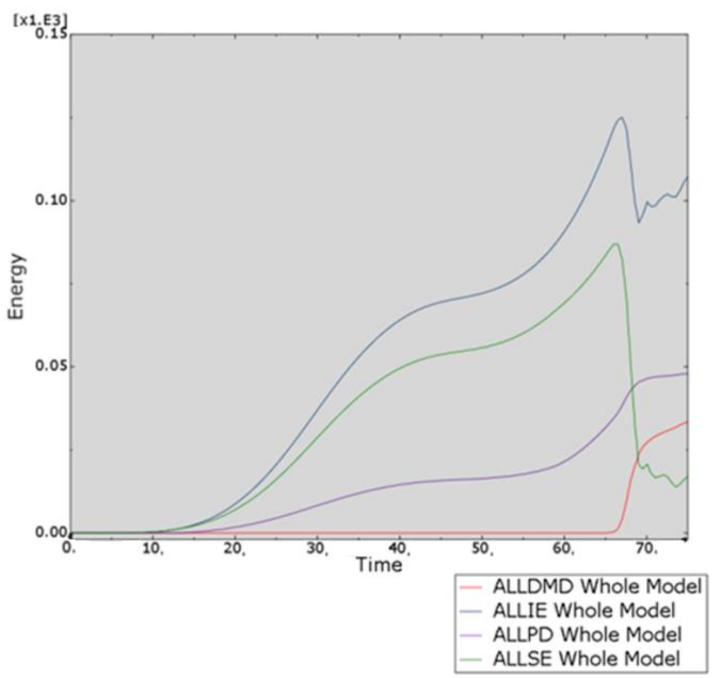

Figure 7.14 Energy analysis of the heterogeneous model

(unit of energy J, unit of time sec)

Figure 7.15 shows the stress-strain curve of the heterogeneous model from Abaqus. This curve expresses the composition of the stress-strain curves for each node in the model. It matches well with the stress-strain curve of the shale sample (Figure 6.8a) from Chapter 6, validating the simulation.

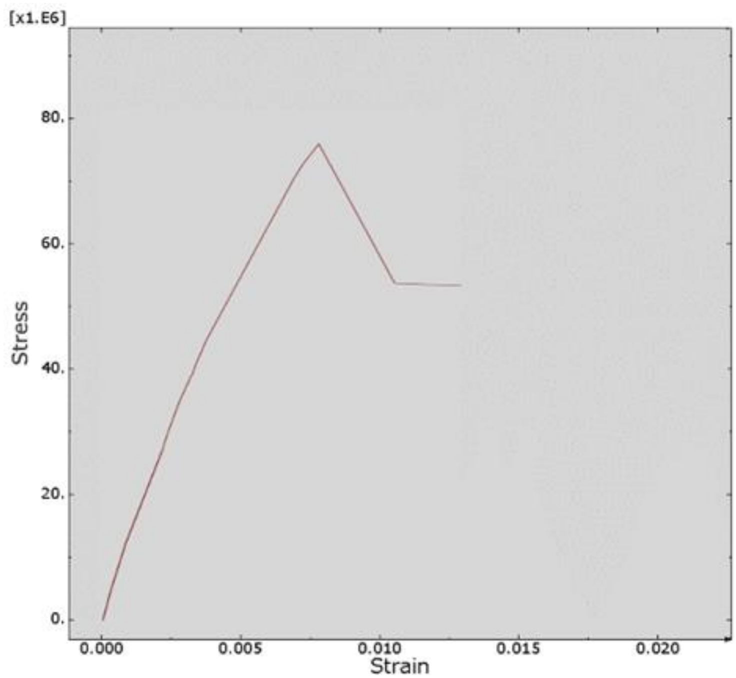

Figure 7.15 Stress-strain curve from Abaqus

(unit of stress Pa)

It is unlikely that two curves will be exactly the same. In Figures 6.8a and 7.15, the latter is a little bit larger in Young's modulus but smaller in stain and ultimate strength than the former. This is because the former is from a loading-unloading test. Hardness and toughness of the rock sample improves under repeated loading making it more challenging for the rock sample to fail. Also, it is not possible to completely master the information from the rock sample and this causes inaccuracy. A rock sample is strongly heterogeneous and the rock mechanics parameters in each part of the sample are different. The limits of the current technology mean that the heterogeneity base is approximate in the test. Each factor above contributes to the discrepancy in the curves.

7.2.4 3D models considering confining pressure

This section considers the influence of confining pressure on rock failure based on the simulation of an axial compression test. The same fracturing mechanism, contact mode and loading method are used. The confining pressure is added and changed during the simulation to determine if confining pressure has an effect on rock failure.

The rock is loaded from 0 to 85MPa without considering confining pressure in the simulation (Figure 7.16). Next, the confining pressure is added with 10MPa, 20MPa and 30MPa, respectively, and the load remains unchanged (Figures 7.17 to 7.19). Finally, the maximum load is increased from 85MPa to 90MPa and maintains a confining pressure of 30MPa (Figure 7.20).

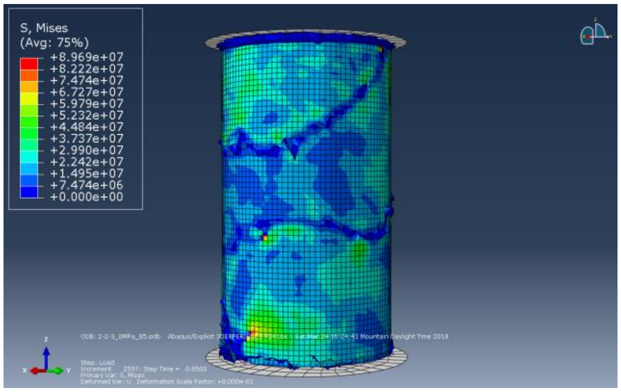

a. 3D Model

(unit of stress Pa)

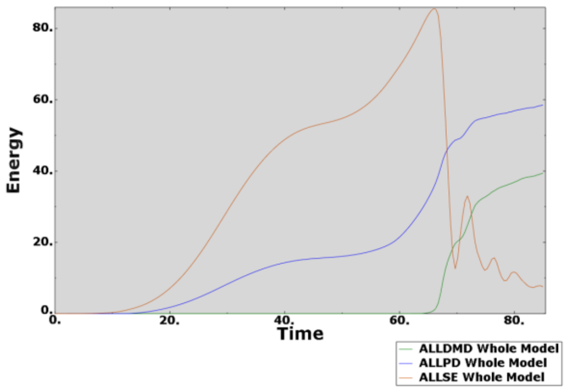

b. Energy analysis

(unit of energy J, unit of time sec)

Figure 7.16 Model with energy analysis (Pc=0 and Pmax=85MPa)

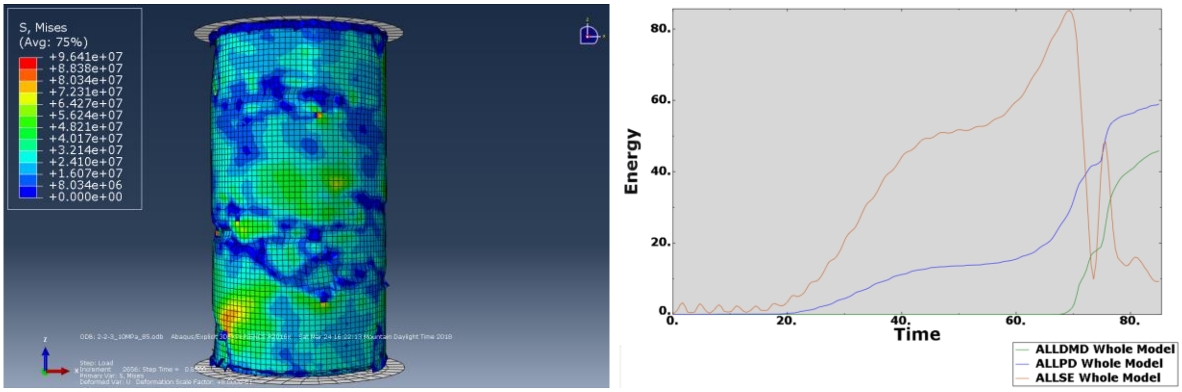

a. 3D Model
(unit of stress Pa)

b. Energy analysis
(unit of energy J, unit of time sec)

Figure 7.17 Model with energy analysis (Pc=10MPa and Pmax=85MPa)

Figures 7.16 and 7.17 demonstrate how adding confining pressure influences the degree of a rock fracture by increasing the crack number, plastic energy and elastic energy. Damage energy seems do not change much. At low confining pressure (Figure 7.16 and 7.17), there is not many cracks after the failure and much more damage happens in the ends of the rock simple.

As confining pressure increases, crack number increases (Figure 7.17 and 7.18) until the confining pressure reaches a certain value. After reaching this value, the crack number do not increase or even decrease with the increase of confining pressure (Figure 7.19). By keeping the confining pressure the same and increasing the maximum load from 85MPa to 90MPa, the crack number and the damage energy of the model increases further (Figure 7.20).

Based on the outcomes of the above work it is not possible to conclude if confining pressure promotes or restrains the rock failure. When the loading from outside is great enough, confining pressure promotes the rock failure by forcing the rock sample to be more tight and strong in hardness and toughness. At this point, energy accumulation is higher than that of low confining pressure before the rock failure. This is why both elastic energy and plastic energy increase when confining pressure increases in Figures 7.17 and 7.18. The increase of confining pressure tends to help the rock create more cracks after the failure, when input energy or loading is sufficient.

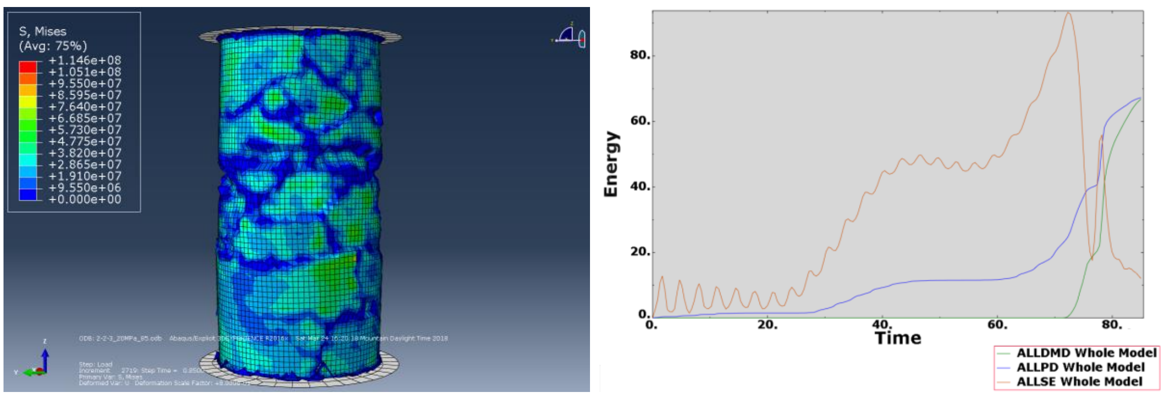

a. 3D Model (unit of stress Pa)

b. Energy analysis (unit of energy J, unit of time sec)

Figure 7.18 Model with energy analysis (Pc=20MPa and Pmax=85MPa)

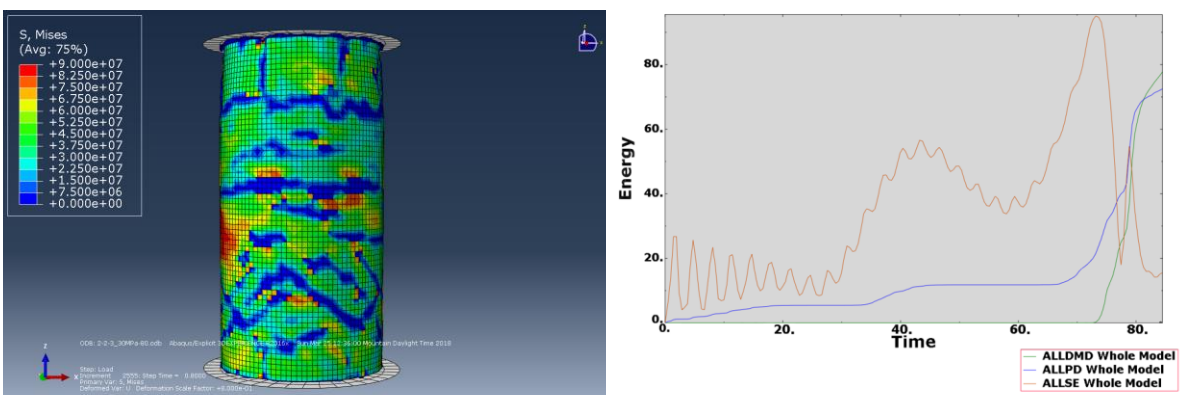

a. 3D Model (unit of stress Pa)

b. Energy analysis (unit of energy J, unit of time sec)

Figure 7.19 Model with energy analysis (Pc=30MPa and Pmax=85MPa)

If input energy or loading is not enough or just enough to fail the rock, the increase of confining pressure will resist the rock from further failure by increasing the hardness and toughness of the rock (Figure 7.20). That’s why there is a contradiction in chapter 3 where Young’s modulus and ultimate strength increase and rock plasticity increases as confining pressure increases (Figure 4.2). It is necessary to realize the relationship between input energy and confining pressure to find the optimum combination to get more cracks after rock failure.

7.3 Coupled Pore Fluid Diffusion and Stress Analysis Models

The last section shows the influence of confining pressure on different degrees of rock failure in the axial compression test. The brittleness evaluation of hydraulic fracturing is more complicated. Shale reservoirs are impacted by the different stress fields underground. The reservoirs are fractured by high fluid pressure, which is more complicated than compression tests. Coupled pore fluid diffusion and stress analysis models are established in this section based on the models in the last section to address this challenge.

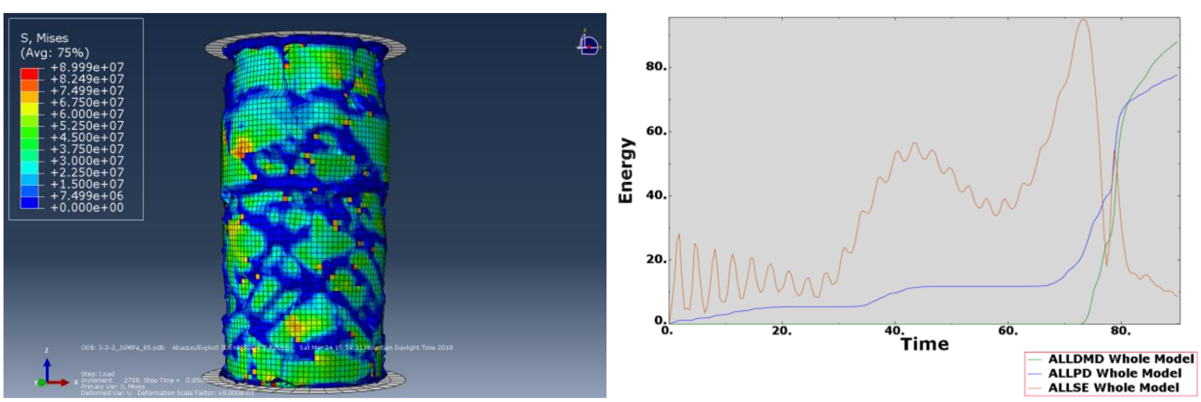

a. 3D Model (unit of stress Pa)

b. Energy analysis (unit of energy J, unit of time sec)

Figure 7.20 Model with energy analysis (Pc=30MPa and Pmax=90MPa)

7.3.1 Model description

The coupled hydro-mechanical (HM) models in this section consider the influence of rock permeability, leak off, gap flow, pore fluid pressure and in-situ stress. Two-dimensional (2D) and 3D models are established separately.

7.3.1.1 2D model description

The 2D model describes the process of hydraulically driven fracture initialization and propagation in a permeable pore medium. Homogeneous models are established to simulate both sandstone and shale reservoirs. The radius of this reservoir is 100 meters. Since the reservoir is symmetrical, only half the reservoir is simulated to reduce the mesh size. Mean values of material properties of shale and sandstone samples in the experiment in chapter 6 have been used. Table 7.1 provides the parameters used in the simulation for the shale and sandstone reservoirs. XFEM is used in 2D models to define the initialization of cracks (Figure 7.2).

Normal flow has been created by defining a fluid leak-off coefficient. This coefficient defines a pressure-flow relationship between a middle element and its adjacent surface elements (Figure 7.21) (Dassault Systèmes, 2016).

The normal flow is defined as

$$q_t = c_t(p_i - p_t) \tag{7-7}$$

and

$$q_b = c_b(p_i - p_b) \tag{7-8}$$

where q_t and q_b are the flow rates into the top and bottom surfaces, respectively, p_i is the midface pressure, and p_t and p_b are the pore pressures on the top and bottom surfaces, respectively.

Table 7.1 Reservoir parameters and fluid coefficients for shale and sandstone reservoirs

Parameter	Shale value	Sandstone value
Radius of the reservoir, m	100	100
Young's modulus, Pa	2.10E+09	1.21E+10
Poisson's ratio	0.3	0.2
Max principal stress, Pa	4.50E+07	9.80E+07
Damage evolution, N/m	3.00E+04	3.00E+04
Fluid leakoff coefficients, m/(Pa.s)	5.88E-10	5.88E-09
Gap flow, Pa.s	1.00E-03	2.00E-03
Permeability, mD	1.00E-03	1.00E-01
Porosity	0.12	0.18
Density, kg/m^3	2.50E+03	2.65E+03
vertical stress, Pa	1.50E+07	1.50E+07
minimum horizontal stress, Pa	8.50E+06	8.50E+06
maximum horizontal stress, Pa	1.85E+07	1.85E+07
injection flow rate, m^3/s	1.00E-03	1.00E-03

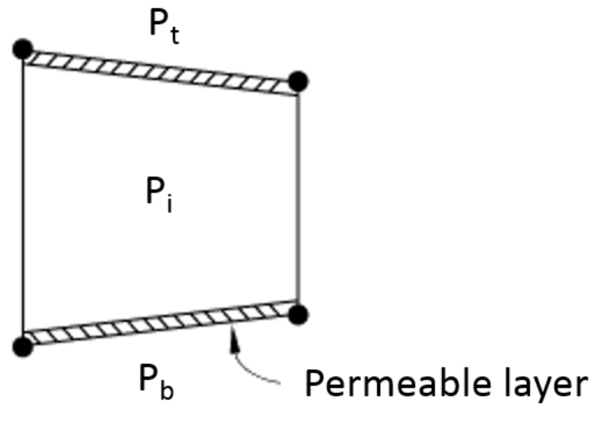

Figure 7.21 Permeable layer by leak off coefficient

A gap flow property is used to define tangential flow combined with the pore fluid material definition. In Abaqus, tangential flow is modelled as either a Newtonian fluid or a power law fluid. Defining the volume flow rate of a Newtonian fluid, it is expressed as:

$$qd = -k_t \nabla p \tag{7-9}$$

where k_t is the tangential permeability, ∇p is the pressure gradient along the element, and d is the gap opening.

In Abaqus, d (the gap opening) is defined as:

$$d = t_{curr} - t_{orig} + g_{init} \tag{7-10}$$

where t_{curr} and t_{orig} are the current and original cohesive element geometrical thicknesses, respectively; g_{init} is the initial gap opening (Dassault Systèmes, 2016). Figure 7.22 has both the tangential and normal flow within the cohesive elements.

To simulate the process described above, CFLOW is a key word used in the Abaqus model to simulate the flow to nodes of the injected high-pressure fluid.

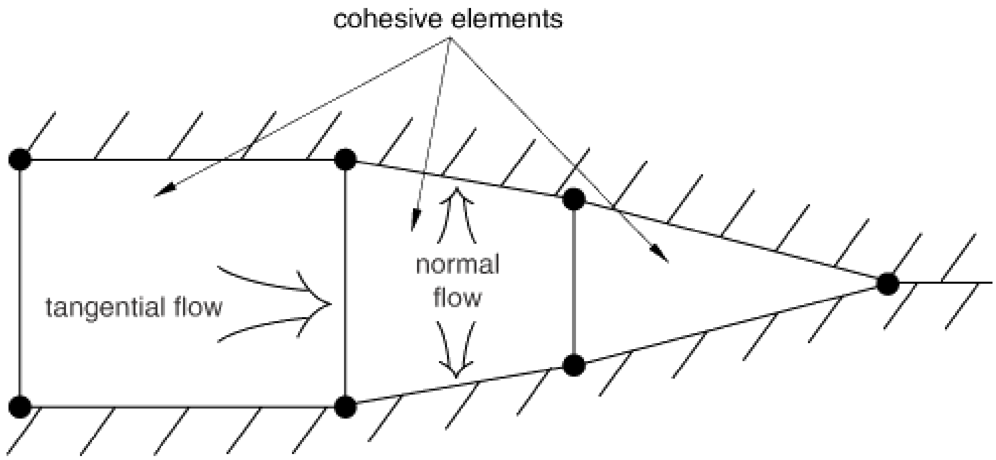

Figure 7.22 Flow within cohesive elements

7.3.1.2 3D model description

This 3D model simulates the whole process of hydraulic fracturing in an open hole including fluid injection, proppant injection and production. The shape of the reservoir is a cylinder with the wellbore in the center. The radius of this reservoir is 250 meters. Since the reservoir is symmetrical, only half the reservoir is simulated to reduce the mesh size. Mean values of material properties of shale samples in the experiment in chapter 6 have been used. The parameters used in the simulation for the reservoir are in Table 7.2. Pore pressure cohesive elements are used in 3D models to define the initialization of the cracks. The definitions of the normal flow and the tangential flow are the same as 2D models.

Drucker-Prager yield criterion has been used to determine whether a material has failed or undergone plastic yielding. Permeability and porosity are defined by user subroutines and changes with coordinates to ensure a heterogeneous model for pore structure. The initial stress field, including vertical stress, minimum horizontal stress and maximum horizontal stress, are defined by user subroutines to consider the influence of pore pressure and coordinates.

Table 7.2 Reservoir parameters and fluid coefficients for 3D reservoir simulation

Parameter	Value
Radius of the reservoir, m	250
Reservoir thickness, m	50
Young's modulus, Pa	2.10E+09
Poisson's ratio	0.25
Fluid leakoff coefficients, m/(Pa.s)	5.88E-10
Gap flow, Pa.s	1.00E-03
Permeability, mD	1.00E-03
Porosity	0.12
Density, kg/m^3	2.50E+03
Vertical stress, Pa	User defined
Minimum horizontal stress, Pa	User defined
Maximum horizontal stress, Pa	User defined
Injection flow rate, m^3/min	2.0

The process has four steps:

1. Add the initial in-situ stress and pore pressure into the system to achieve an equilibrium.
2. The fracturing fluid is pumped into the reservoir from the well to initialize a crack. A flow with a rate of 2.0m^3/min is injected into the reservoir for 20 minutes.
3. The behaviour of the proppants injected into the reservoir is simulated.
4. The production of oil or gas is simulated until the steady state conditions are achieved.

Besides the key word CFLOW used in 2D models, user subroutines of DISP, DLOAD, SIGINI, UPOREP, UFLUIDLEAKOFF, and VOIDRI are used to code the file to realize the process outlined above. See Appendix B for more details of these user subroutines.

7.3.2 Model setup

This section describes the setup of boundary conditions, predefined fields and mesh generation in the simulation.

Boundary conditions are used to specify the values of all the basic solution variables of displacement, temperature and pore pressure at boundary nodes (Dassault Systèmes, 2016). In this simulation, the displacement value of nodes at the edge of the model are set as 0 in the x-axis direction. This prevents the model from moving when flow is injected. The pore pressure value of nodes at the edge of the model is set up to simulate pore pressure in infinity.

Predefined fields are time-dependent, non-solution-dependent fields that exist over the spatial domain of the model (Dassault Systèmes, 2016). In this simulation, the predefined fields of a void ratio, pore pressure and in-situ stress are set up to define their initial values for the model.

Most meshing in Abaqus is done in a "top-down" fashion, where a mesh is created to follow exactly the geometry of the domain and moves down toward the element and node positions. There are many types of meshes applied with different purposes. In this simulation, CPE4P and C3D8RP are used in the 2D and 3D models, respectively, to simulate pore fluid diffusion and stress analysis. CPE4P is a 4-node plane strain quadrilateral with bilinear displacement and bilinear pore pressure. C3D8RP is an 8-node brick with trilinear displacement, trilinear pore pressure, reduced integration and hourglass control. The local mesh refinement is set up to accurately describe fractures.

7.3.3 Results of 2D models

The simulations of 2D shale reservoirs and sandstone reservoirs have been done. The influence of in-situ stress has been considered in the following 2D models.

7.3.3.1 The simulation of shale reservoir

Figures 7.23 to 7.25 show the fracture geometry during the simulation of a shale reservoir with changing of stress, displacement and pore pressure, respectively. To demonstrate the shape of the fracture, the deformation scale is 20 times greater than the original model.

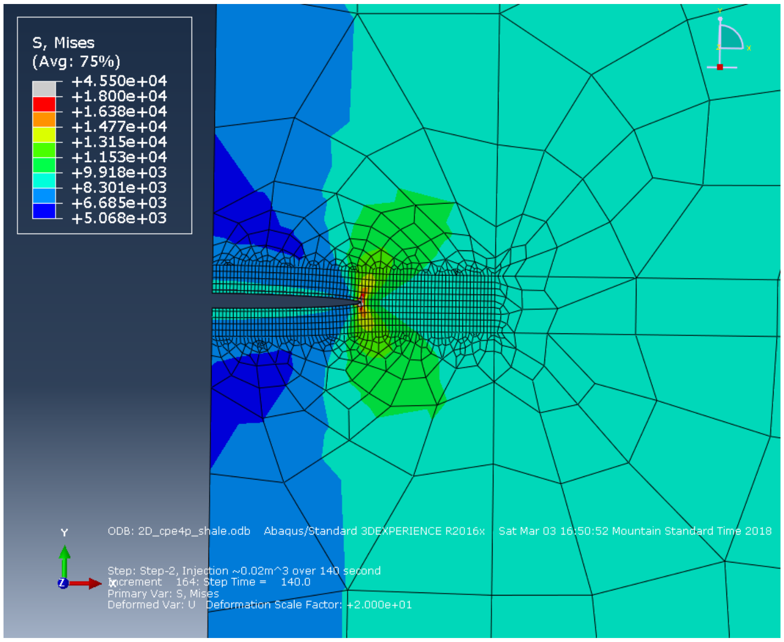

Figure 7.23 Fracture geometry with stress change of shale reservoir (20x)

(unit of stress kPa)

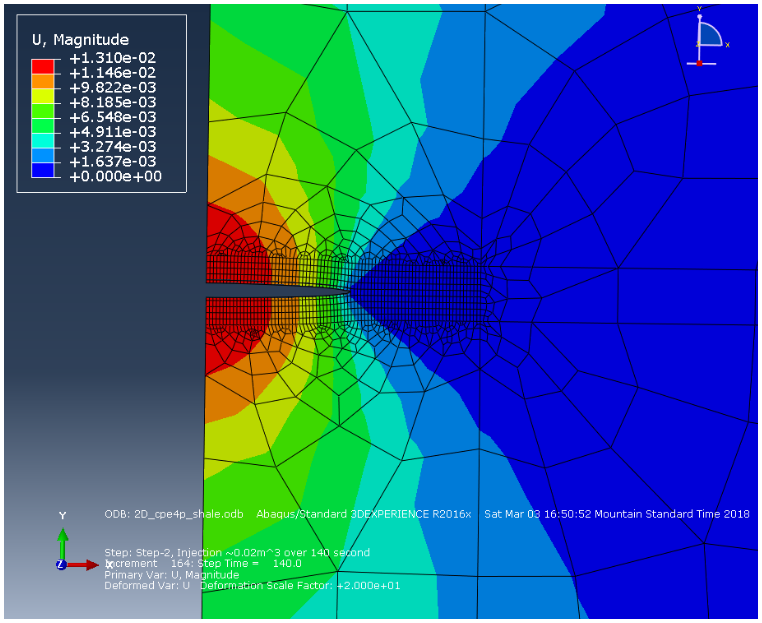

Figure 7.24 Fracture geometry with stress change of shale reservoir (20x)

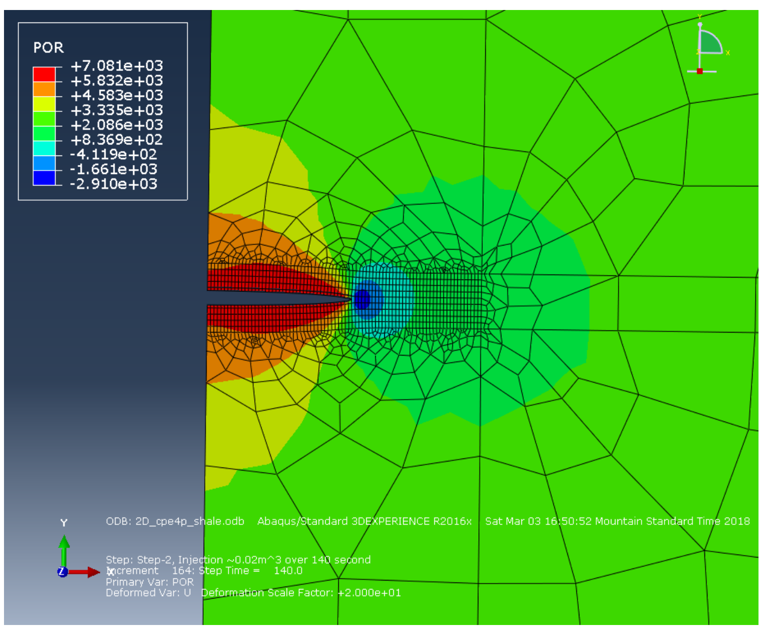

Figure 7.25 Fracture geometry with pore pressure change of shale reservoir (20x)

(unit of stress kPa)

This is a homogeneous model with one fracture created during the process. The stress field around the crack tip and rock mechanics parameters control the brittle fracture during crack growth. The analysis of stress distribution near the crack tip is important in fracture mechanics (Sun, 2012). The maximum stress is in the crack tip (Figure 7.23). The symmetrical distribution of stress near the crack tip (Figure 7.23) indicates that the primary cracking mode in this hydraulic fracture process is mode I (Figure 4.10a). This result validates the research described in Chapter 3; tensile failure occurs in hydraulic fracturing. The maximum displacement and pore pressure are in the two fracture faces (Figures 7.24 and 7.25). The high-pressure fluid impacting the two fracture faces is speculated to be the cause of the high pore pressure. During the process, the grids of the two fracture faces are compressed and pore pressure of those grids increases preventing the fracture from further propagation. The damage energy during the hydraulic fracture process are calculated in Figures 7.26.

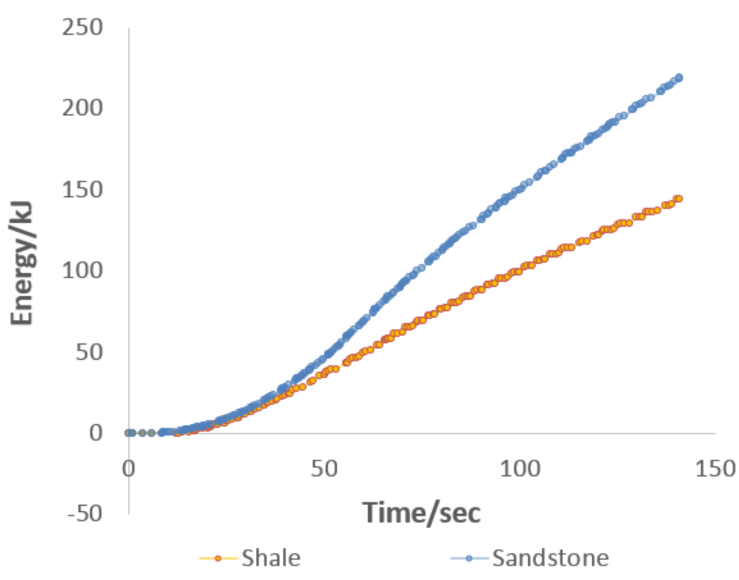

Figure 7.26 Damage energy of shale and sandstone reservoirs

7.3.3.2 Difference between shale and sandstone reservoirs

In this section, the simulation of a sandstone reservoir is established and compared to the results from the shale reservoir. The main difference between sandstone and shale reservoirs are the mechanical properties: Young’s modulus, Poisson's ratio and ultimate stress. Figure 7.27 shows the fracture geometry with stress change in the sandstone reservoir.

The sandstone fracture is much longer in length and slightly shorter in width than the fracture formed in shale under the same injection rate and time (Figures 7.23 and 7.27). The simulation of the sandstone reservoir expresses a greater damage energy (Figure 7.26) than the shale reservoir simulation.

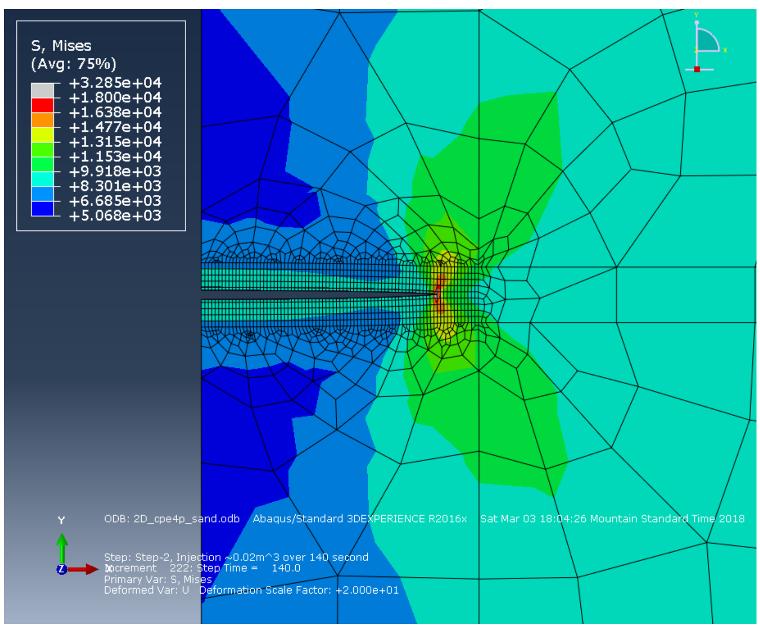

Figure 7.27 Fracture geometry with stress change of sandstone reservoir (20x)

(unit of stress kPa)

Energy efficiency in fracturing r_{ef} is defined as:

$$r_{ef} = \frac{Damage\_energy}{Total\_energy} \tag{7-11}$$

The results indicate that the energy efficiency for a sandstone reservoir is greater than that for the shale reservoir (Figure 7.28). More energy is transferred to damage energy for sandstone than shale causing a larger fracture in the sandstone than in shale reservoirs. The energy efficiency in fracturing is related to rock mechanical properties and environmental factors like in-situ stress and temperature.

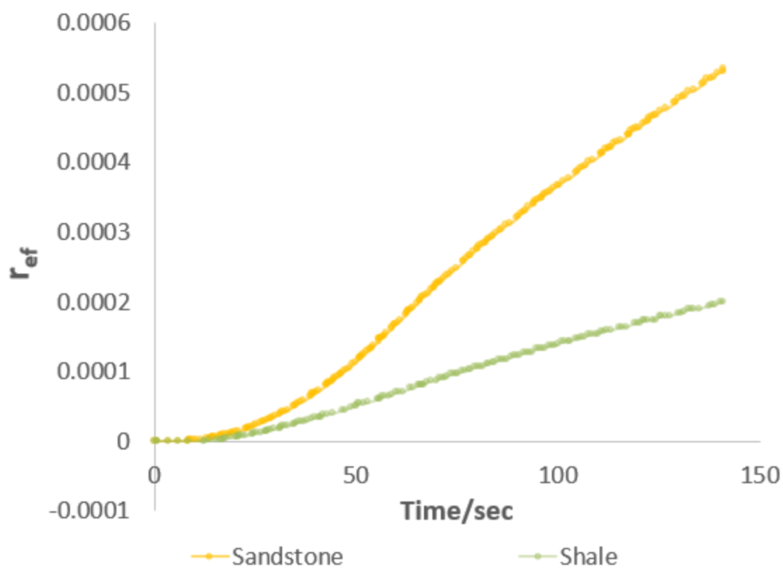

Figure 7.28 r_{ef} of sandstone and shale reservoirs

7.3.3.3 The influence of in-situ stress

To determine how in-situ stress affects fractures, variations in the in-situ stress under the existing 2D model is executed. See Figure 7.29 for the damage energy under different in-situ stresses.

The red line represents the damage energy without changing the in-situ stress. The green line is the change in damage energy with the increase of maximum principal stress from 18.5Mpa to 25.5Mpa. The blue line reveals the damage energy as there is an increase of minimum principal stress from 8.5Mpa to 12.5Mpa. When the maximum principal stress is increased parallel to the direction of fracture propagation, elastic energy and internal energy increase while pore pressure and damage energy almost remain unchanged. When we increase the minimum principal stress perpendicular to the direction of fracture propagation, elastic energy, internal energy and pore pressure increase while damage energy decreases. The increase of minimum principal stress tends to prevent the fracture propagation and pore pressure and may offset part of the effect.

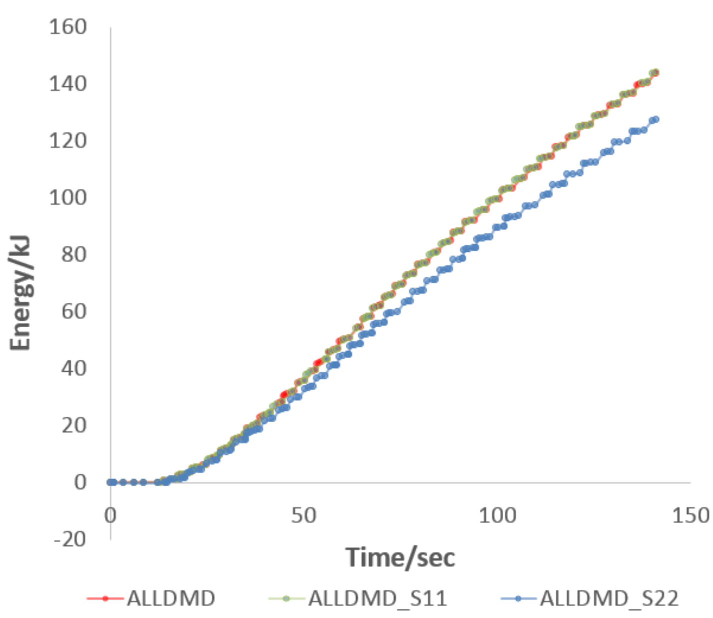

Figure 7.29 Damage energy under variable in-situ stress

7.3.4 Results of 3D models

Figure 7.30 provides the fracture geometry during different steps of the 3D simulation. The fracture is about 71m long. The pore pressure in the two fracture faces continues to increase during steps 2 and 3 as the fluid and proppants are injected into the reservoir (Figure 7.30a to d). When the maximum value is reached at the end of step 3 there is a decrease in step 4 simulating the production of oil or gas (Figure 7.30e and f) and a decrease of the bottom hole pressure.

Elastic energy, damage energy and plastic energy are calculated in Figure 7.31. The equilibrium of in-situ stress and pore fluid pressure before the stimulation has been considered in the 3D models (step 1). During the stimulation stage, the strain energy and the internal energy decrease, while the damage energy and the plastic energy increase rapidly. During the production stage, the strain and the internal energy increase slowly, while the damage and the plastic energy remain unchanged.

An unexpected outcome is both the damage energy and the plastic energy are a very small part of the whole energy system. This may be due to the tensile break of the reservoir because injecting a fluid requires less energy than compression-shear cracking in an axial compression test. The rocks adjacent to the fracture can support each other to prevent further deformation. Therefore, not much energy is used in reservoir deformation.

This 3D model is an attempt to simulate the process of hydraulic fracturing while considering energy analysis and fracture development. It demonstrates how the hydraulic fracturing process can be simulated with real stress analysis and energy analysis. It needs further improvement.

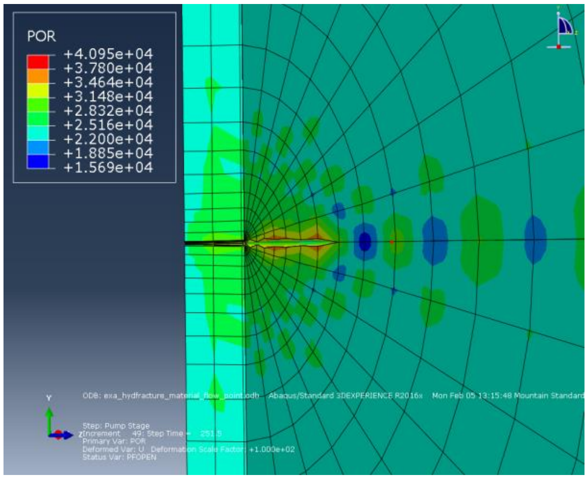

a. 200s in step 2

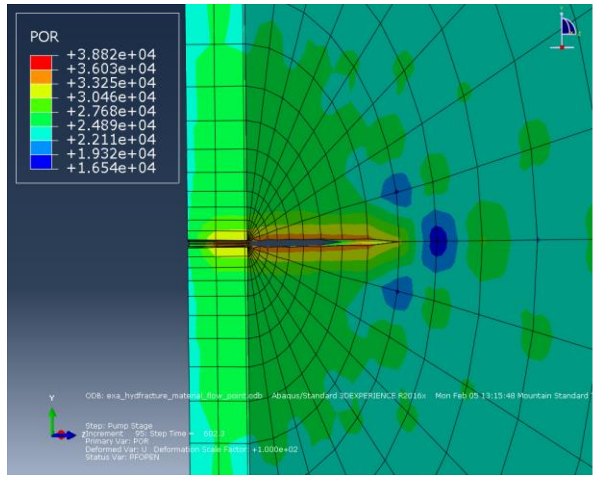

b. 600s in step 2

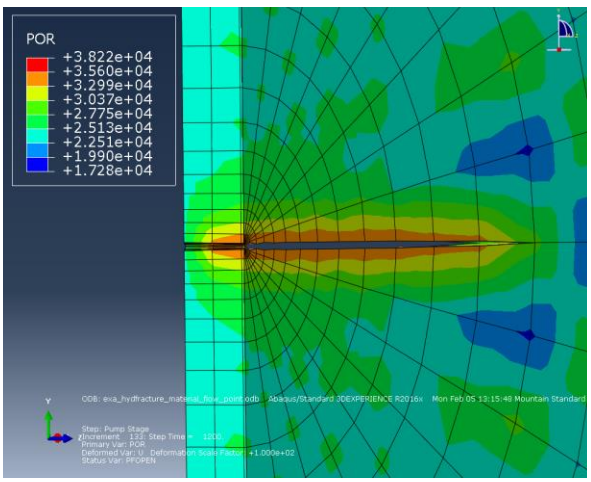

c. 1200s in step 2

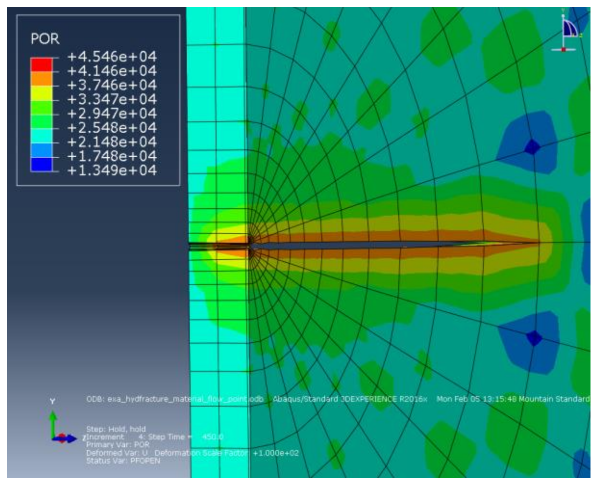

d. 450s in step3

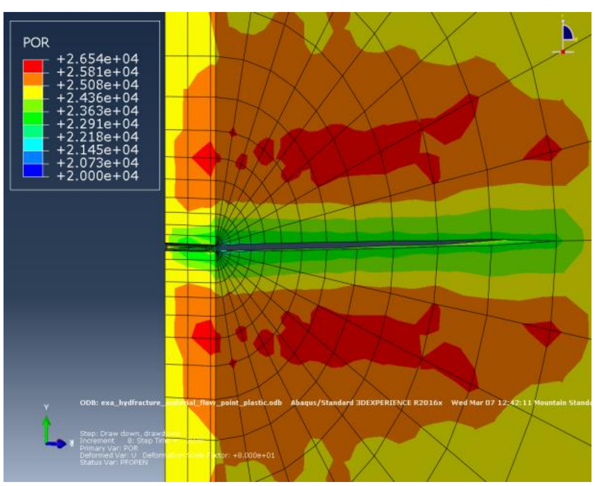

e. 2300s in step 4

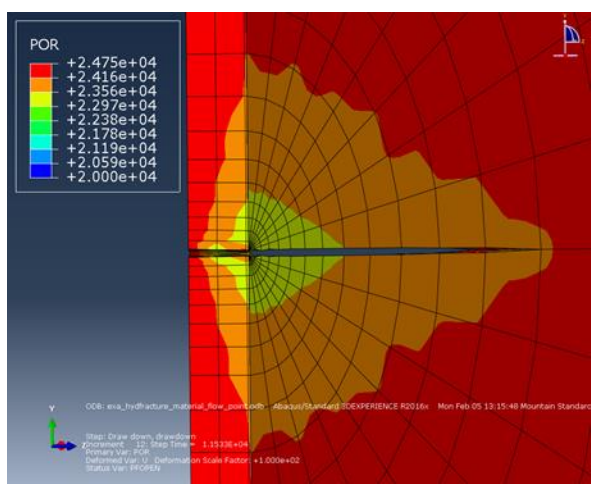

f. 26000s in step4

Figure 7.30 Fracture geometry in different steps of the 3D simulation (20x), unit kPa

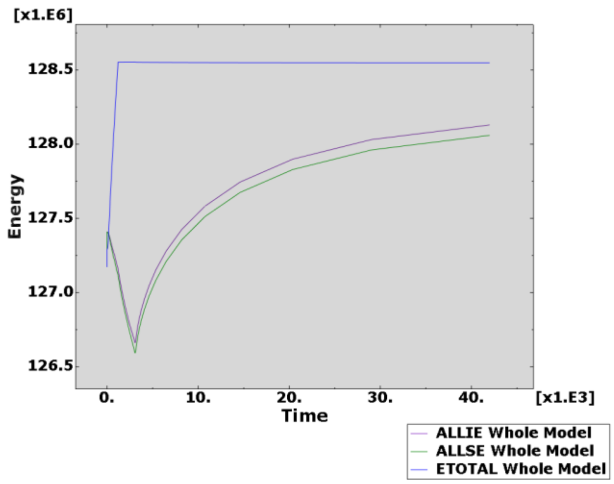

a. Strain, internal and total energy

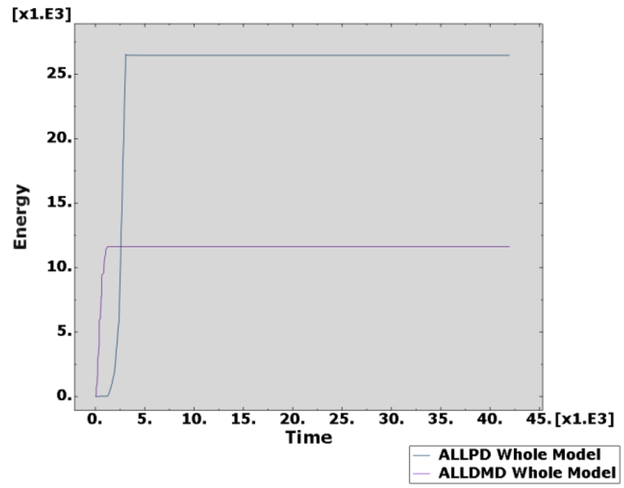

b. Damage and plastic energy

Figure 7.31 Energy analysis of the 3D simulation

(unit of energy kJ, unit of time sec)

7.4 Conclusions

(1) Elastic strain energy, plastic energy, damage energy and internal energy can be calculated using the FEM during rock failure.

(2) The simulation using the FEM to analyze an energy change and the degree of rock failure is validated by the axial compression test in Chapter 6.

(3) Confining pressure in axial compression tests helps to create more cracks after the rock failure when input energy or loading is great enough and resist the rock from further failure when input energy is not enough.

(4) Coupled pore fluid diffusion and stress analysis models are used to simulate the process of hydraulic fracturing. Compared to a shale reservoir, a sandstone reservoir is higher in damage energy and energy efficiency during the simulation.

(5) The increase of minimum principal stress in hydro-mechanical coupling models tends to prevent fracture propagation. The pore pressure may offset part of this effect.

8. Conclusions and Future Work

8.1 Conclusions

(1) A semi-analytical model that considers the influence of Young's modulus, Poisson's ratio, tensile strength, pressure and fracture toughness in brittleness evaluation has been established and matches well with experimental results.

(2) Porosity decreases with an increase in temperature while microcracks increase with an increase in temperature. Energy dissipation at high temperature is greater than the dissipation at a relatively low temperature. The thermal energy from heating provides the extra energy necessary to make cracks.

(3) A thermal cause of abnormally high pore pressure cannot be ignored in brittleness evaluation of unconventional reservoirs. The relationship between temperature and pore pressure can be expressed based on thermo-poroelastic equations.

(4) Brittle minerals play a different role in BI prediction. Usually, quartz > dolomite > calcite > clay is the order for increasing rock brittleness. Young's modulus plays a more important role than Poisson's ratio in BI prediction, which is reasonable from the point of mineralogy.

(5) By comparing the value of energy dissipation and release it is possible to evaluate rock brittleness and predict the degree of rock fragmentation after rock failure.

(6) Elastic strain energy, plastic energy, damage energy and internal energy can be calculated using the FEM during rock failure. The simulation using the FEM to analyze an energy change and the degree of rock failure is validated by the axial compression tests.

(7) Confining pressure in the axial compression tests helps to create more cracks after the rock failure when input energy or loading is great enough and resist the rock from further failure when input energy is not enough.

(8) Coupled pore fluid diffusion and stress analysis models are used to simulate the process of hydraulic fracturing. Compared to a shale reservoir, a sandstone reservoir is higher in damage energy and energy efficiency during the simulation.

(9) The increase of minimum principal stress in hydro-mechanical coupling models tends to prevent fracture propagation. The pore pressure may offset part of this effect.

8.2 Future Work

Chapter 7 is an attempt to identify an accurate and quantitative method for brittleness and fracability evaluation. The results show that this method based on the energy while effective still needs further improvement.

Only one fracture has been considered in the coupled pore fluid diffusion and stress analysis models in this thesis. Multi-fracture system will be considered in the next step. The influence of temperature and the interaction between the wellbore and reservoir are not considered during the simulation. The influence of pore pressure is more complicated than previous speculation. Temperature may affect rock brittleness by means of pore pressure but THM coupling was not part of the research in this thesis. Further research is underway. In chapter 7, the 3D model simulates the process of hydraulic fracturing in an open hole. The influence of the interaction between the wellbore and the reservoirs has been ignored. It will be considered in the following research.

References

Al-Shayea, N.A., Khan, K., Abduljauwad, S.N., 2000, Effects of confining pressure and temperature on mixed-mode (I-II) fracture toughness of a limestone rock. International Journal of Rock Mechanics and Mining Sciences, 37: 629-643.

Altindag, R., 2003, Correlation of Specific Energy With Rock Brittleness Concepts on Rock Cutting. J. South African Institute of Mining and Metallurgy, 103 (3): 163–171.

Andreev, N. Y., 1995, Brittle failure of rock materials, Technology & Engineering

Aoudia, K., Jennifer L. M., and Nicholas B. H., et al., 2010, Statistical Analysis of the Effects of Mineralogy on Rock Mechanical Properties of the Woodford Shale and the Associated Impacts for Hydraulic Fracture Treatment Design. Salt Lake City: the 44th US Rock Mechanics Symposium and 5th U.S.-Canada Rock Mechanics Symposium, UT, 27-30 June 2010.

Babuska, I., and Melenk, J., 1997, The partition of unity method, International Journal for Numerical Methods in Engineering, 40: 727-758.

Batzle, M. L., and B. J. Smith., 1992, Hand-Held Velocity Probe for Rapid Outcrop and Core Characterization. Proceedings of the 33rd US Symposium on Rock Mechanics, Sante Fe, New Mexico, Tillerson & Wawersik (eds.), Rotterdam, Balkema: 949-958.

Becker, G. F., 1893, Finite homogeneous strain, flow and rupture of rocks. Geological Society of America Bulletin, 4(1): 13–90.

Belytschko, T., and Black, T., 1999, Elastic crack growth in _nite elements with minimal remeshing. International Journal for Numerical Methods in Engineering, 45(5):601-620.

Biret, F., Valentin, G., Gordo B., et al. 1989, Effect of pressure on rock toughness. International symposium of rock mechanics, p. 165-170.

Bishop, A., 1967, Progressive failure with special reference to the mechanism causing it: Proc. Geotech. Conf., Oslo, p. 142-150.

Bodziak, R., Clemons, K., Stephens A., et al. 2014, The role of seismic attributes in understanding the hydraulically fracturable limits and reservoir performance in shale reservoirs: An example from the Eagle Ford Shale, south Texas. AAPG Bulletin, 98(11):2217-2235.

Bradley, J. S., and Powley, D. E., 1994, "Pressure Compartments in Sedimentary Basins: A Review," in AAPG Memoir, American Association of Petroleum, P. Ortoleva (Ed.), Tulsa, OK, p. 3-26.

Chen, X., 2005, Finite Element Methods and Their Applications. Springer Berlin Heidelberg New York

Chen Z., Chen M., Jin Y., 1997, Experimental study on the relationship between rock fracture toughness and acoustic velocity. Oil drilling & production technology, 19(5): 56-60.

Chmura, K., Chudek, M., 1992, Geotermomechanika górnicza (Mining Geothermomechanics). Mikołów, Księgarnia Naukowa Suplement".

Cho, D., and Perez, M., 2014, Brittleness revisited. GeoConvention, Calgary, 12-16 May 2014

Coates, D., and Parsons, R., 1966, Experimental criteria for classification of rock substances: International Journal of Rock Mechanics and Mining Sciences & Geomechanics Abstracts, p. 181-189.

Copur, H., Bilgin, N., Tuncdemir, H. et al. 2003, A Set of Indices Based on Indentation Tests for Assessment of Rock-Cutting Performance and Rock Properties. J. South-African Institute of Mining and Metallurgy, 103 (9): 589–599.

Diao H. Y., 2013, Rock mechanical properties and brittleness evaluation of shale reservoir. Acta Petrologica Sinica, 29(9): 3300-3306.

Dimitriyev, A.P., Kusyayev, L. S., Protasov, Y. I., Yamschichikov, V. S., 1969, Physical Properties of Rocks at High Temperature (translated from Russian). Moskva, Nedra.

Dassault Systèmes, 2016, Abaqus Theory Guide.

Du, Z. Z., 2010, "Extended Finite Element Method (XFEM) in ABAQUS," ABAQUS Inc., USA.

Dassault Systèmes, 2016, Abaqus Analysis User's Guide.

Eberhart-Philips, D., Han, D.H., Zoback, M. D., 1989, Empirical relationships among seismic velocity, effective pressure, porosity, and clay content in sandston. GEOPHYSICS, 54(1), 82-89.

Gandossi, L., Ulrik Von Estorff, 2015, An overview of hydraulic fracturing and other formation stimulation technologies for shale gas production. Scientific and Technical Research Reports. Joint Research Centre of the European Commission; Publications Office of the European Union, EUR 26347

Hajiabdolmajid, V., and Kaiser, P., 2003, Brittleness of Rock and Stability Assessment in Hard-Rock Tunneling. Tunnelling and Underground Space Technology, 18 (1): 35–48.

Handin, J., Hager, R. V., Friedman, M., et al. 1963, Experimental Deformation of Sedimentary Rocks under Confining Pressure Pore Pressure Tests. AAPG bulletin, 47(5): 717-755

Harris, N. B., Hemmesch, N. T., Mnich, C. A., et al. 2009, An Integrated geological and Petrophysical Swtudy of a Shale Gas Play: Woodford Shale, Permian Basin, West Texas. Gulf Coast Association of Geological Societies Transactions, 59: 337-346.

Hemmesch, N. and Harris, N. B., 2009, Sequence Stratigraphic Architecture for the Late Devonian Woodford Shale, Southern Permian Basin, West Texas. In AAPG Annual Meeting Abstracts, Denver, Colorado, 7-10 June 2009.

Hertzberg, R. W., 1995, Deformation and Fracture Mechanics of Engineering Materials (4 ed.). Wiley. ISBN 0-471-01214-9.

Holt, R., Fjær, E., Nes, O., and Alassi, H., 2011, A shaly look at brittleness: 45th US Rock Mechanics/Geomechanics Symposium.

Honda, H., and Sanada, Y., 1956, Hardness of Coal. Fuel 35: 451–461.

Hucka, V., and Das, B., 1974, Brittleness determination of rocks by different methods: International Journal of Rock Mechanics and Mining Sciences & Geomechanics Abstracts, p. 389-392.

Hucka, V., and Das, B., 1974, Brittleness determination of rocks by different methods: International Journal of Rock Mechanics and Mining Sciences & Geomechanics Abstracts, p. 389-392.

Hu, Y., Gonzalez Perdomo, M. E., Wu, K., et al. 2015, a Novel Model of Brittleness Index for Shale Gas Reservoirs: Confining Pressure Effect. SPE 176886.

Hu, Y., Gonzalez Perdomo, M. E., Wu, K., et al. 2015, New Models of Brittleness Index for Shale Gas Reservoirs: Weights of Brittle Minerals and Rock Mechanics Parameters. SPE 177010.

Hu. Y., Chen, Z., 2016, A Novel Model of Brittleness Index for Unconventional Reservoirs: Confining Pressure and Pore Pressure Effect. AAPG annual convention, Calgary, Alberta, 19-22 June 2016.

Hu, Y., Chen, Z., Chen, K., et al. 2016, Effect of Temperature on Brittleness Evaluation of Unconventional Reservoirs. AAPG annual convention, Calgary, Alberta, 19-22 June 2016.

Hu, Y., Chen, Z., Chen, K ., et al. 2016, A Novel Method of Brittleness Evaluation for Unconventional Reservoirs Based on Energy Consumption. AAPG annual convention, Calgary, Alberta, 19-22 June 2016.

Ingram, G. M., and Urai, J. L., 1999, Top-seal leakage through faults and fractures: the role of mudrock properties: Geological Society, London, Special Publications, 158: 125-135.

Jaeger, J. C., and Cook, N. G., 1976, Fundamentals of rock mechanics.

Jarvie, D. M., Hill, R. J., Ruble, T. E., and Pollastro, R. M., 2007, Unconventional shale-gas systems: The Mississippian Barnett Shale of north-central Texas as one model for thermogenic shale-gas assessment: AAPG bulletin, 91: 475-499.

Jin, X., Shah, S. N., Roegiers, J. C., et al. 2015, An Integrated Petrophysics and Geomechanics Approach for Fracability Evaluation in Shale Reservoirs. SPE Journal, 20(3): 518-526

Jin Y., Chen M., Zhang X., 2001, Determination of fracture toughness for deep well rock with geophysical logging data. Chinese Journal of Rock Mechanics and Engineering, 20(4): 454-456.

Ko, T.Y., Kemeny, J., 2007, Effect of confining stress and loading rate on fracture toughness of rocks. American Rock Mechanics Association, ARMA-07-076.

Lawn, B., and Marshall, D., 1979, Hardness, Toughness, and Brittleness: An Indentation Analysis. J. American Ceramic Society, 62 (7–8): 347–350.

Li, Q., Chen, M., Jin, Y., el al. 2012, Indoor evaluation method for shale brittleness and improvement. Chinese Journal of Rock Mechanics and Engineering, 31(8): 1680-1685

Li, Q., Chen, M., Jin, Y., el al. 2012, Experimental research on failure modes and mechanical behaviors of gas-bearing shale. Chinese Journal of Rock Mechanics and Engineering, 31(2): 3763-3771.

Liu, Q. S., and Xu, X. C., 2000, Damage analysis of brittle rock at high temperature. Chinese Journal of Rock Mechanics and Engineering, 19(4): 408-411.

Mnich, C. A., 2009, Geochemical Signatures of Stratigraphic Sequences and Sea-Level Change in the Woodford Shale, Permian Basin. MSc Thesis, Geology and Geological Engineering Department, Colorado School of Mines, Golden, Colorado.

Moes, N., Dolbow J., and Belytschko, T., 1999, A Finite Element Method for Crack Growth without Remeshing. INTERNATIONAL JOURNAL FOR NUMERICAL METHODS IN ENGINEERING, 46: 131-150.

Nagel, N., Gil, I., Sanchez-Nagel M., et al. 2011, Simulating hydraulic fracturing in real fractured rock - overcoming the limits of pseudo3D models. SPE 140480.

Nikki, T. H., Nicholas, B. H., Cheryl, A. M., et al. 2014, A sequence-stratigraphic framework for the Upper Devonian Woodford Shale, Permian Basin, west Texas. AAPG Bulletin, 98(1):23-47.

Oliver J., 1995, Continuum modelling of strong discontinuities in solid mechanics using damage models. Computational Mechanics, 17:49-61.

Paterson, M. S., and Wong, T. F., 2005, Experimental rock deformation-the brittle field, Springer.

Portas, R.M., Slatt, R., 2010, Characterization and origin of fracture patterns in a Woodford Shale quarry in southeastern Oklahoma for application to exploration and development. AAPG Annual Convention and Exhibition, New Orleans, Louisiana, 11-14 April 2010

Qu, P., Shen, R., Fu, L., et al. 2011, Time delay effect due to pore pressure changes and existence of cleats on borehole stability in coal seam. Coal Geology, 85(2): 212-218.

Quinn, J.B., and Quinn, G.D., 1997, Indentation Brittleness of Ceramics: A Fresh Approach. J. Materials Sci, 32 (16): 4331–4346.

Ranjith, P. G., Viete, D.R., Chen, B., et al., 2012, Transformation plasticity and the effect of temperature on the mechanical behaviour of Hawkesbury sandstone at atmospheric pressure. Engineering Geology, 151: 120-127

Rashid M. M., 1998, The arbitrary local mesh renement method: an alternative to remeshing for crack propagation analysis. Computer Methods in Applied Mechanics and Engineering, 154:133-150.

Rickman, R., Mullen, M., Petre, J., Grieser, W., and Kundert, D., 2008, A practical use of shale petrophysics for stimulation design optimization: all shale plays are not clones of the barnett shale: SPE 115258.

Rutter, E.H., 1972, The effects of Strain-Rate Changes on the Strength and Ductility of Solenhofen Limestone at Low Temperature and Confining Pressures. International Journal of Rock Mechanics and Mining Sciences & Geomechanics, 9: 183-189

Sehgal, J., Nakao, Y., Takahashi, H. et al. 1995, Brittleness of Glasses by Indentation. J. Materials Science Letters, 14 (3): 167–169.

Seto, M., Kuruppu, M.D., Funatsu, T., 2001, Fracture toughness testing of rock at elevated temperature and pressures. 38th U.S. rock mechanics symposium, 745-751.

Sun, C. T., and Jin, Z. H., 2012, Fracture Mechanics. Academic Press is an imprint of Elsevier, p. 295.

Sygała, A., Bukowska, M., Janoszek, T., 2013, High-temperature mechanical, physical and Thermal properties of granitic rocks - a review. Journal of Sustainable Mining, 12(4): 45-51.

Szwaja, N., 2012, Elastic and Elasto-Plastic Finite Element Analysis of a Tension Test Specimen with and without Voids. Rensselaer Polytechnic Institute Hartford, Connecticut

Tarasov, B., and Potvin, Y., 2013, Universal criteria for rock brittleness estimation under triaxial compression. International Journal of Rock Mechanics & Mining Sciences, 59:57-69

Vermylen, J. P., Zoback, M. D., 2011, Hydraulic Fracturing, Microseismic Magnitudes, and Stress Evolution in the Barnett Shale. SPE 140507

Wan, Z., Zhang, Y., Zhang, Y., and Wang, C., 2009, Research Status Quo and Prospection of Mechanical Characteristics of Rock under High Temperature and High Pressure. Procedia Earth and Planetary Science No 1, p. 565–570.

Wang, D., Ge, H., Wang, X., et al. 2015, A novel experimental approach for fracability evaluation in tight-gas. Journal of Natural Gas Science and Engineering, 23(2015): 239-249.

Wang, F. P., and J. F. Gale, 2009, Screening criteria for shale-gas systems. Gulf Coast Association of Geological Societies Transactions, 59: 779-793.

Woodruff, D.P., 2002, The chemical physics of solid surfaces. Elsevier Science B.V, The Netherlands

Wu, K., Li, X., Guo, C., & Chen, Z., 2015, Adsorbed Gas Surface Diffusion and Bulk Gas Transport in Nanopores of Shale Reservoirs with Real Gas Effect-Adsorption-Mechanical Coupling. Society of Petroleum Engineers. doi:10.2118/173201-MS

Xie, H., Peng, R., Ju, Y., et al. 2005, On energy analysis of rock failure. Chinese Journal of Rock Mechanics and Engineering, 24(15): 2603-2608.

Yagiz, S., 2009, Assessment of Brittleness Using Rock Strength and Density with Punch Penetration Test. Tunnelling and Underground Space Technology, 24 (1): 66–74.

Yang, H., 2014, Analysis on the Influencing Factors of Brittleness of Shale Reservoir. MSc Thesis, China University of Geosciences, Beijing.

Ying, T., 2012, Study on Dynamic Behavior of Rocks Considering Thermal Effect. Central South University.

Zhang, L., Mao, X., Lu, A., 2009, Experimental Study on the Mechanical Properties of Rocks at High Temperature. Science in China Series E: Technological Sciences, 52(3): 641-646.

Zhang, L., Mao, X., Liu, R., et al. 2013, the Mechanical Properties of Mudstone at High Temperatures: an Experimental Study. Rock Mechanics and Rock Engineering, 12(4): 45-51.

Zhang, Z., 2013, Energy Evolution Mechanism during Rock Deformation and Failure. China University of Mining and Technology, Beijing.

Zhong, J., Gardoni, P., and Rosowsky, D., 2010, Stiffness Degradation and Time to Cracking of Cover Concrete in Reinforced Concrete Structures Subject to Corrosion. Journal of Engineering Mechanics, 136(2): 209-219.

Zoback, M. D., 2007, Reservoir Geomechanics, Cambridge University Press.

Appendix A: Data description and Experimental Design

In order to make our analysis more applicable, two sets of data from different regions are adopted.

Data1:

Data 1 is from Sichuan basin in China (Table 2.1). Young's modulus, Poisson's ratio and compressive strength under different confining pressure are collected from triaxial tests (RTR-1000). Tensile strength is calculated by Brazil disk split tests. Also, an analysis of rock mineral composition has been done by using X-ray diffractometer from PANalytical Company.

The test results show that the primary mineral compositions of the samples are quartz, calcite and feldspar. Illite is the main mineral of clay, followed by montmorillonite. The same digit of the first sample number (like 1-1 & 1-2) means that the samples are from the same position. Results of X-ray diffraction show that mineral compositions and contents of those samples are almost the same. Therefore, mineral compositions and contents of those samples possess the same values (Table 2.1).

Data2:

Samples are collected from the Barnett, Haynesville, Eagle Ford and Longmaxi shale (Table 2.2). A shale reservoir is at a three-dimensional stress state. In order to better match the actual situation underground, we control the confining pressure by using a triaxial test. We also consider the depth, rock type, orientation and angle of the core (Table 2.2). The triaxial test has been done by using a MTS815 triaxial mechanical testing system from the China University of Petroleum (Beijing). Before the test, cores have been made into standard cylinder specimens. Finally, 15 rock samples have been obtained from the test, whose cracks are visible to naked eyes (Jarvie, 2007).

X-ray diffraction analyses show that the main mineral components of the Barnett shale samples are quartz and feldspar, followed by carbonate and clay minerals. Mineral components of the Haynesville shale are nonuniform. Samples at different depths are quite different. The content of carbonate minerals is relatively high in the Eagle Ford shale. For the Longmaxi shale, the content of brittle mineral is about 63.7%, which is almost the same as for the Haynesville shale (about 63.92%), but somewhat less than for the Barnett shale (about 71.94%) (Holt, 2011).

Appendix B Introduction of User Subroutines

User subroutines of DISP, DLOAD, SIGINI, UPOREP, UFLUIDLEAKOFF, and VOIDRI have been used to code a file in order to realize the process in Section 8.3. Following is the details of these user subroutines (Dassault Systèmes, 2016).

DISP is used to define the magnitudes of boundary conditions or connector motions.

DLOAD is used to define the variation of the distributed load magnitude as a function of position, time, element number, load integration point number.

SIGINI is used to define initial stress fields at particular material points (these are the effective stress values for the analysis). These initial stress fields can be defined as functions of coordinates, element number, integration point number.

UPOREP is used to define the initial pore pressure values of a porous medium. The initial pore pressure values can be defined as functions of nodal coordinates and/or node numbers. It is also used to define initial fluid pore pressure values in a coupled pore fluid diffusion and stress analysis.

UFLUIDLEAKOFF is used to define the fluid leak-off coefficients for pore pressure elements. It includes material behavior dependent on field variables or state variables

VOIDRI is used to define initial void ratio values at material calculation points of continuum elements in a porous medium. The initial void ratio values can be defined as functions of material point coordinates and/or element numbers.